
THE UNIVERSITY *of* EDINBURGH

# Deep radio imaging of the UKIDSS Ultra Deep Survey field: the nature of the faint radio population, and the star-formation history of the Universe


*Vinodiran Arumugam*

A thesis submitted in fulfilment of the requirements
for the degree of Doctor of Philosophy
to the
University of Edinburgh
February 2013

# Declaration

Except where otherwise stated, the research undertaken in this thesis was the unaided work of the author. Where the work was done in collaboration with others, a significant contribution was made by the author.

*Vinodiran Arumugam*
February 2013

# Abstract

The centrepiece of this thesis is a deep, new, high-resolution 1.4-GHz image covering the United Kingdom Infrared (IR) Telescope IR Deep Sky Survey (UKIDSS) Ultra Deep Survey (UDS) legacy field. Deep pseudo-continuum observations were made using the Very Large Array, prior to its recent upgrade, in its A, B and DnC configurations. The resulting mosaic has a full-width-at-half-maximum synthesised beam width of $\approx 1.7$ arcsec and a point-source sensitivity of $\approx 60\mu$Jy ($6\,\sigma$) across the central $0.6\,\mathrm{deg}^2$, while conserving flux from sources of extended emission. The full image covers $1.3\,\mathrm{deg}^2$. I also present a catalogue containing over 1,000 radio emitters, having chosen the 6-$\sigma$ threshold by maximising the number of radio sources with secure optical/near-IR counterparts.

Most of the sources in the catalogue ($\approx 90$ per cent) lie in the sub-mJy flux density regime. Deep, complementary data covering a wide range of wavelengths was used to explore this faint radio population, whose nature remains controversial. It was found that 53 per cent of the sample comprise active galactic nuclei (AGN). AGN dominate at $\gtrsim 0.2$ mJy and remain a significant population down to 0.1 mJy; at lower fluxes – the so-called $\mu$Jy radio population – star-forming galaxies become dominant.

The radio sample presented here was also matched to *Hubble Space Telescope* imaging of the UDS field (which is part of the Cosmic Assembly Near-IR Deep Extragalactic Legacy Survey – CANDELS) to classify the faint radio population morphologically. These classifications were done using the Gini–$M_{20}$ method. It was found that a low fraction of AGN and SFGs are undergoing interactions and mergers, $33 \pm 9$ and $13 \pm 7$ per cent, respectively. The merger fraction does not appear to have evolved significantly since $z \sim 3$. This suggests that mergers have played a relatively minor role in the assembly of galaxies and super-massive black holes – certainly less significant than previously thought.

Finally, I present a study of cosmic star-formation activity as a function of stellar

mass and redshift, exploiting panchromatic stacking. Mid-IR–through–radio images, including new data from *Herschel*, are stacked at the positions of a *K*-selected (i.e. an approximately mass-selected) sample in the UDS field. Specific star-formation rates (SSFR, i.e. star-formation rate per stellar mass, or the rate at which a galaxy is converting its gas into stars) were derived from UDS radio luminosities measured here and stellar masses from the literature. The SSFR was found to be poorly correlated with stellar mass; it decreases with decreasing redshift; at a given mass, SSFR rises with redshift. These results indicate that at early epochs, galaxies were forming stars more efficiently and at a higher rate.

# Acknowledgements

I would like to thank my parents, to whom I dedicate this thesis, for their unwavering encouragement and support over the years and for financially supporting me through the PhD. Without your love and support, this ambition would never have been possible. I am also grateful to my two sisters for always being supportive.

A big thank you to Rob Ivison for the guidance and support through the PhD and with this thesis - it took a while, but we got there in the end! You have been a great mentor to me - in astronomy and beyond. I would also like to thank Eduardo Ibar for being a patient teacher and Philip Best for his advice and guidance on various aspects of my PhD. In addition, I would also like to acknowledge John Stott, Nathan Bourne and Marco Viero for the different collaborations in which I was involved.

The PhD experience would not have been as enjoyable if not for the good times and great laughs I shared with my colleagues at the Observatory. In particular, I would like to thank William Taylor for the fun, geeky chats we shared and for the great observing nights out; Trevor Back for being good company during late nights in the Vista Huts; Jack Mayo, Victoria Bruce and Alasdair Thomson for being great office mates and for the great office banter; and Paula Wilkie (and her magical stationery cupboard), Tania Johnston (especially for allowing me to rant at you in the mornings about thesis progress), Martin Black, Sandy Rogers, David Harvey, Julia Kennedy and Henry Pearce for being great company over the years.

Another part of what made this PhD an enjoyable experience was the opportunity to participate in public engagement, which served as a persistent reminder of my passion for astronomy. For this, I would like to thank Tania Johnston, Dave Chalton, Will Sharp and the rest of the Visitor Centre crew for the fun times we had working together.

The work presented in this thesis was funded in part by the School of Physics and Astronomy and European Research Council Advanced Grant, 321302, COSMICISM.

"If we knew what we were doing, it wouldn't be called research."

– Albert Einstein

# Contents


**1 Introduction** **1**
- 1.1 The radio Universe . . . 1
  - 1.1.1 The extragalactic radio population . . . 2
  - 1.1.2 The faint radio population . . . 5
- 1.2 Star-forming galaxies . . . 6
  - 1.2.1 Submm-selected galaxies . . . 9
  - 1.2.2 The far-IR/radio correlation . . . 10
- 1.3 Active Galactic Nuclei . . . 11
  - 1.3.1 Radio galaxies . . . 13
- 1.4 The origin of radio emission and interferometry . . . 14
  - 1.4.1 Synchrotron radiation . . . 14
  - 1.4.2 Radio interferometry . . . 18
  - 1.4.3 Instrumental effects . . . 22
  - 1.4.4 The (Jansky) Very Large Array . . . 26
- 1.5 Outline of thesis . . . 27

**2 Deep, high-resolution radio imaging of the UKIDSS Ultra Deep Survey** **29**
- 2.1 Introduction . . . 29
- 2.2 Observations . . . 31
- 2.3 Data reduction and imaging . . . 32
  - 2.3.1 Bandwidth smearing effects . . . 37
- 2.4 Source extraction and cataloguing . . . 39
  - 2.4.1 Source extraction . . . 39
  - 2.4.2 A robust final catalogue . . . 40
- 2.5 Source counts . . . 41
- 2.6 Confusion . . . 47
- 2.7 Identifying radio counterparts to submm galaxies . . . 48
- 2.8 Conclusions . . . 51

**3 Multi-wavelength properties of the faint radio population** **53**
- 3.1 Introduction . . . 53
- 3.2 Multi-wavelength observations of the UDS . . . 54
  - 3.2.1 Optical and near-IR observations . . . 54

3.2.2 *Spitzer* observations . . . 55
3.2.3 X-ray imaging . . . 55
3.3 Photometric and spectroscopic redshifts . . . 56
3.4 Radio sub-sample . . . 57
3.5 Spectroscopic Classification . . . 59
3.6 Near-IR properties of the radio sample . . . 61
3.7 Mid-IR (24-$\mu$m) properties of the radio sample . . . 64
3.8 X-ray properties of the radio sample . . . 66
3.9 Nature of the faint radio population . . . 68
3.9.1 Luminosity and redshift distributions . . . 68
3.9.2 Partitioning the radio population between AGN and SFGs . . . 71
3.10 Conclusions . . . 71

**4 Morphologies of the faint radio population 75**
4.1 Introduction . . . 75
4.2 Quantifying galaxy morphology . . . 76
4.2.1 Sersic index . . . 77
4.2.2 *CAS* parameters . . . 78
4.2.3 Gini and $M_{20}$ . . . 79
4.3 Data and sample selection . . . 80
4.3.1 Deep *HST* observations of the UDS . . . 80
4.3.2 Sample selection from the faint radio population . . . 80
4.4 Morphological analysis . . . 83
4.5 Conclusions . . . 86

**5 Panchromatic stacking 89**
5.1 Introduction . . . 89
5.2 Observations . . . 92
5.2.1 Parent sample, photometric redshifts and stellar masses . . . 92
5.2.2 *Herschel* observations . . . 93
5.2.3 Radio observations . . . 93
5.2.4 Archival observations in the mid-IR and submm wavebands . . . 93
5.3 Stacking $K$-selected galaxies . . . 94
5.4 Stacking of far-IR observations . . . 94
5.4.1 Simultaneous stacking . . . 95
5.4.2 Traditional stacking . . . 95
5.4.3 Comparison of the two stacking methods . . . 96
5.5 Stacking in the radio waveband . . . 99
5.5.1 Radio-derived star-formation rates . . . 101
5.6 Specific star-formation rates . . . 103
5.7 Future work . . . 104

**6 Conclusions 107**

**Bibliography** **109**

**Publications** **115**

# Chapter 1

# Introduction

## 1.1 The radio Universe

Radio astronomy began with the discovery of radio emission along the Galactic plane by Karl Jansky in 1931. Non-thermal synchrotron emission is detected mainly at radio wavelengths, although it can also contribute all the way across the electromagnetic spectrum and can dominate in the X-ray band. It arises due to the acceleration of relativistic particles through a magnetic field and provides a means of studying high-energy regions. Radio observations are also widely used to study atomic and molecular gas, e.g. probing $H_2$ using the $J = 1 - 0$ rotational transition of CO at $\lambda_{\rm rest} = 2.6\,$mm, or probing H I via its 21-cm line.

Atmospheric absorption of electromagnetic radiation limits the wavelengths at which ground-based astronomy can be done. The radio window spans across 0.3 mm to approximately 20 m in wavelength (15 MHz to 1 THz); the cut-off is limited by the ionosphere and water vapour at longer wavelengths and by $O_2$ and $CO_2$ at shorter wavelengths. Observing across this wide window requires a range of telescopes with different observing capabilities, using different observing techniques.

Radio observations have become an important part of astronomy, providing an insight into processes that cannot be provided at other wavelengths. The radio spectrum can be observed with sub-arcsecond spatial resolution, through a technique known as interferometry. This not only allows for detailed imaging of distant objects but also the determination of source positions to high accuracy. The latter point is particularly important in the study of submillimetre-selected galaxies, as will be discussed later. Another advantage of radio astronomy is that radio wavelengths are not

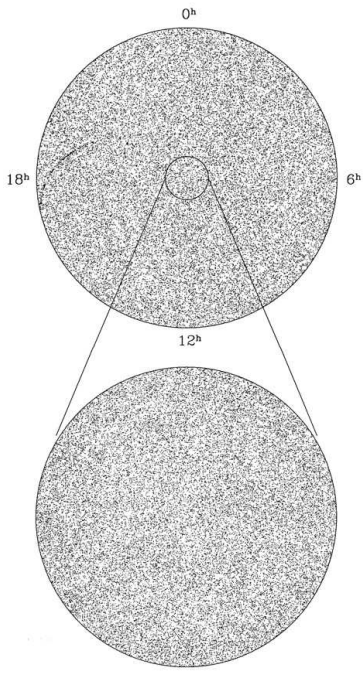


Figure 1.1: The isotropic radio sky. Galactic sources are seen as a faint curved band towards the left of the upper image. Adapted from Condon (2007).

obstructed by dust and so radio emission provides an ideal probe of dust-enshrouded regions. In particular, this makes radio observations a good tracer of young star-forming regions.

In the following section, the extragalactic radio sky is first discussed in the context of the observed radio source counts. In subsequent sections, the different observed sources are introduced. My main area of interest is the faint radio population, consisting mainly of star-forming galaxies. Finally, the fundamental principals of synchrotron emission – the primary emission mechanism at radio wavelengths – and radio interferometry will be introduced here.

### 1.1.1 The extragalactic radio population

The radio sky displays an isotropic distribution of sources compared to the clumpier distributions seen in the optical and infrared sky (Figure 1.1), indicating that nearly all discrete sources are at cosmological distances. The isotropy is due to the large clustering scales of radio galaxies, and the fact that radio emission is unobscured by dust.

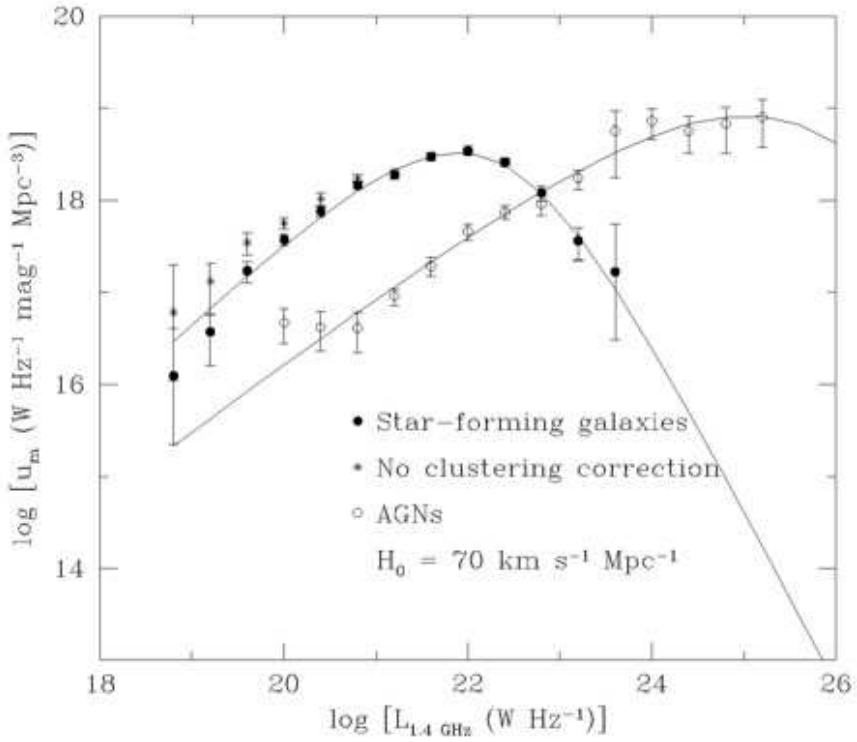


Figure 1.2: The local 1.4-GHz luminosity function for AGNs and SFGs (Condon, 2007).

Determining the distances to nearby galaxies allows us to infer the space densities of sources in a given luminosity range: the radio luminosity function (Condon, 1991). Defining different luminosity functions for different classifications of sources (e.g. active galactic nuclei – AGN, star-forming galaxies – SFGs, etc.) is a more useful method of displaying the distribution of the different kinds of radio sources. One way of distinguishing SFGs from AGN is to employ the far-infrared/radio correlation (discussed later – see Yun et al., 2001) which is obeyed – very tightly – by SFGs. Figure 1.2 shows the 1.4-GHz luminosity functions of SFGs and AGN.

Deep sky surveys have shown that radio-loud AGN dominate the source counts above a flux density of $\approx$ 1 mJy, with SFGs and radio-quiet AGNs dominating the population in the sub-mJy regime. The exact proportion of SFGs to AGN in the sub-mJy population is still hotly debated, but SFGs are expected to become more prominent at 1.4-GHz flux densities below 0.1 mJy – the so-called $\mu$Jy radio population.

The flux density distribution of radio sources is more generally expressed as a differential source count: the number of sources per steradian with flux densities $S$

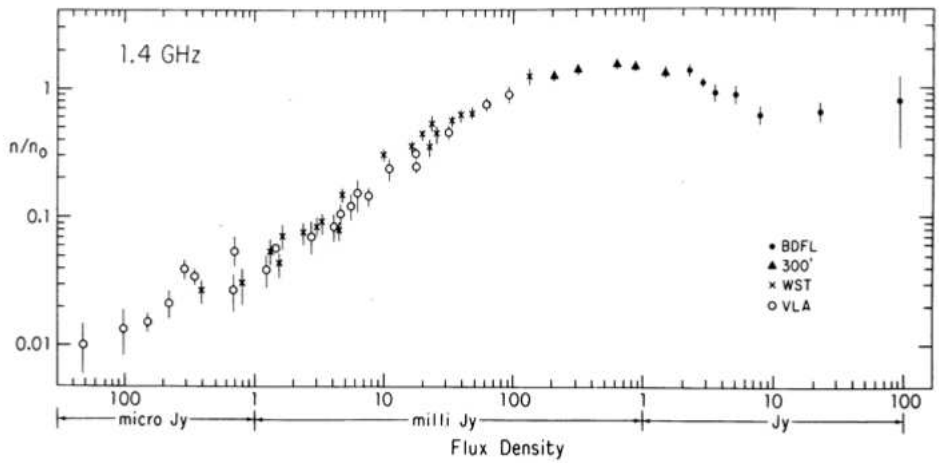


Figure 1.3: Source counts at 1.4 GHz normalised to the expected number density for a Euclidean Universe, $n_0$ (Kellermann & Wall, 1987).

to $S + dS$, $n(S)dS$. For the case of a static, Euclidean Universe, the flux density varies as $D^{-2}$ where $D$ is the distance. The total number of sources brighter than some flux density is then, $N(\ S) \propto S^{-3/2}$ and so the differential source count will go as $n(S) \propto S^{-5/2}$. The expected number density for a Euclidean Universe can then be obtained by plotting $n(S) \times S^{5/2}$, as shown in Figure 1.3.

Obedience to a Euclidean Universe should result in a horizontal distribution on this kind of plot. Above 100 mJy, sources do follow a near-Euclidean form. These are quasars and radio-loud galaxies.

Below 100 mJy, there is a steep drop in source counts. This sharp deviation betrays rapid evolution of the radio population, most probably a space density evolution. These sources are unlikely to display luminosity evolution as Condon (1984) showed that their luminosity is an arbitrary function of time, a model which matches the observations. The sources prominent at these fluxes are radio-quiet AGN and (ultra)luminous infrared galaxies – (U)LIRGs. These latter objects are high-luminosity starburst galaxies, emitting as much as 95% of their energy in the IR (Condon et al., 1998). Ultraluminous starbursts are most easily discovered in observations made at far-infrared (far-IR) and radio wavelengths as they are compact and shrouded in dust.

Figure 1.4 shows an extension of source counts to the sub-mJy region (Richards, 2000), where the weak sources may be beginning to tend back towards a Euclidean distribution. Understanding the nature of this sub-mJy population is the main objective of this thesis and will be achieved by investigating the properties of a large, new sample

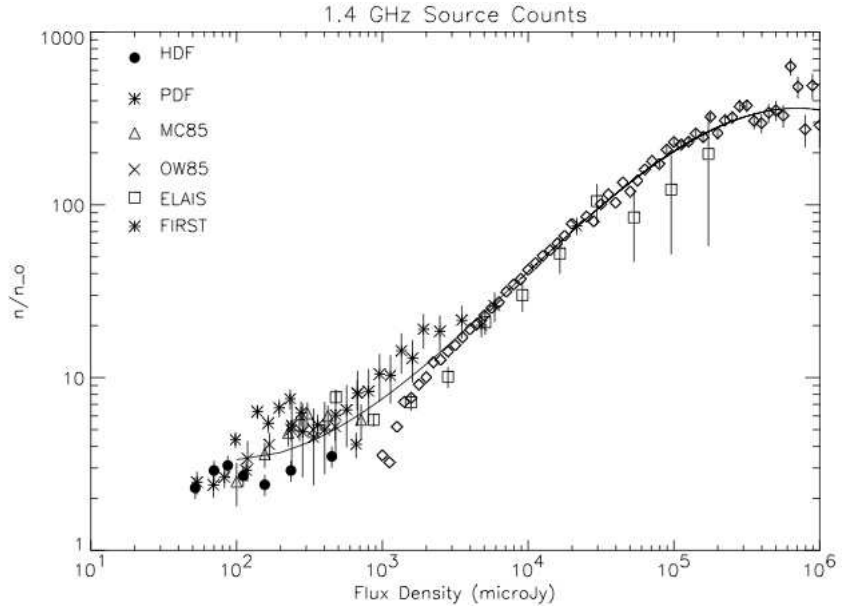


Figure 1.4: Source counts from a deep survey at 1.4 GHz, concentrating on the sub-mJy population (Richards, 2000).

of sub-mJy radio sources.

### 1.1.2 The faint radio population

Determining the fractional composition of SFGs and AGN in various flux density regimes is important in understanding the co-evolution of these two populations in the wider context of galaxy formation and evolution. However, it has been difficult to make progress, due to small and sometimes unreliable samples, and the significant challenge involved in determining optical counterparts, and obtaining spectroscopic redshifts and diagnostics – particularly for the most distant sources.

While radio galaxies with radio-loud super-massive black holes (SMBHs) as central engines dominate the source counts above 1 mJy, the nature of the sources dominating the fainter radio regime is not as clear. Early studies of the sub-mJy radio regime suggested that such sources are usually SFGs, but in the context of today's observational capabilities the quality of the classifications seem (very) unreliable (e.g. Windhorst et al., 1985). As the sensitivity of optical and near-IR surveys have improved, an increasing number of these sources have been associated with early-type galaxies.

Recently, deep radio surveys have employed similarly deep multi-wavelength

observations to investigate the sub-mJy population (Simpson et al., 2006; Barger et al., 2007; Bardelli et al., 2009; Ibar et al., 2009; Strazzullo et al., 2010; Padovani et al., 2011). The sub-mJy regime is now believed to consist of a complex mix of radio-quiet AGN and SFGs.

Chapter 3 discusses a number of diagnostics used to probe the nature of the faint radio population, identifying and classifying SFGs and AGN.

## 1.2 Star-forming galaxies

At the lower end of the radio luminosity function, with radio luminosities of around $10^{28}$ to $10^{32}$ ergs s$^{-1}$, radio emitters are associated with SFGs and radio-quiet AGN (Simpson et al., 2006; Ibar et al., 2009).

Emission from these galaxies – often referred to as 'normal' galaxies – is not dominated by a central SMBH. The radio emission is predominantly non-thermal and is in the form of synchrotron radiation. The astrophysical process responsible for the emission of synchrotron radiation is the acceleration of relativistic electrons, from Type-II and Type-Ib supernovae (SNe), along the magnetic field lines of a galaxy. These SNe are the end products of short-lived ($\tau \lesssim 10^7$ yr) massive stars ($M > 8\,M_\odot$). As relativistic electrons have lifetimes, $\lesssim 10^8$ yr, the radio emission is not influenced by older stellar populations, which makes radio observations a good probe of recent star formation.

The other radiation detected at radio wavelengths is thermal free-free emission. This emerges from H II regions, ionised by massive stars, although this mechanism only becomes significant at frequencies of ($\sim$30–200 GHz). At still higher frequencies, the emission from SFGs is dominated by thermal radiation from dust at rest-frame far-IR wavelengths (see Figure 1.5).

Radio observations are thus an ideal way of detecting and identifying SFGs. Sub-arcsecond spatial resolution, possible due to interferometric observations, mean that highly accurate positions can be determined. For this reason, radio observations are often used to pinpoint dust-enshrouded galaxies, where traditional optical observations are compromised by dust obscuration.

However, radio observations alone are not sufficient to study the general properties of galaxies and to constrain theories of galaxy formation and evolution. To form a more complete picture, data are needed at all observable wavelengths, including those

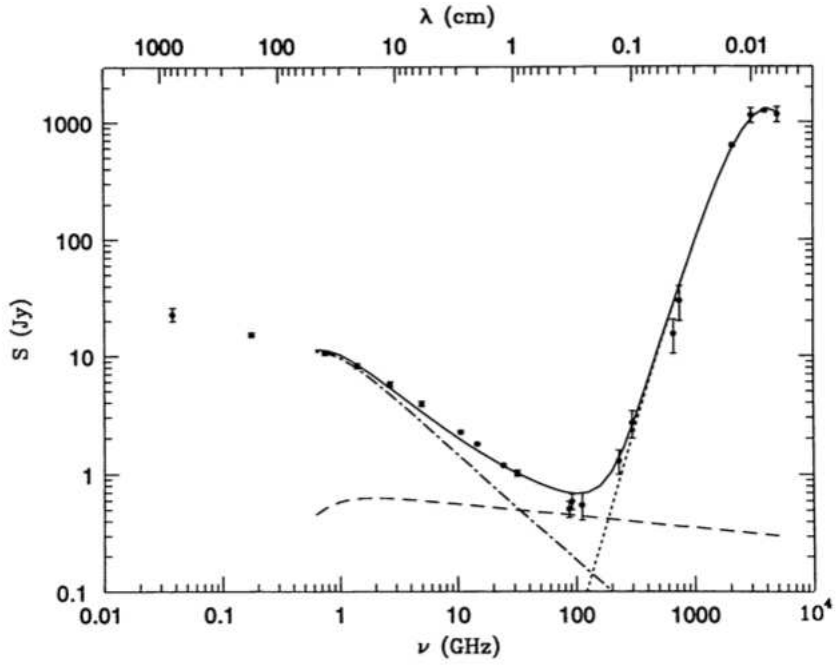


Figure 1.5: Radio–through–far-IR spectrum of the local SFG, M82. The total spectrum is given by the solid line, constituting contributions due to synchrotron emission (dot-dashed line), free-free (dashed line) and dust emission (dotted line) (taken from Condon, 1992).

accessible only from space (X-rays, far-IR), to yield the high-quality spectral energy distributions (SEDs) that are needed to understand the global properties of the observed sources.

Only then can we obtain the level of understanding of these distant sources sufficient to understand the interplay between the quantity and physical state of available gas (the raw material from which stars are made), the rate of cosmic star formation and hence stellar mass assembly, and that of AGN activity. All these are required in order to obtain an in-depth understanding of galaxy formation and evolution.

### Infrared-luminous galaxies

The cosmic IR background (CIRB), first detected by the *COBE* satellite (Puget et al., 1996; Fixsen et al., 1998), showed that the rate of dust-obscured star formation is at least as high as that visible using optical and ultraviolet (UV) data (see Figure 1.6). Dust-enshrouded star-forming regions in galaxies – very luminous at IR wavelengths

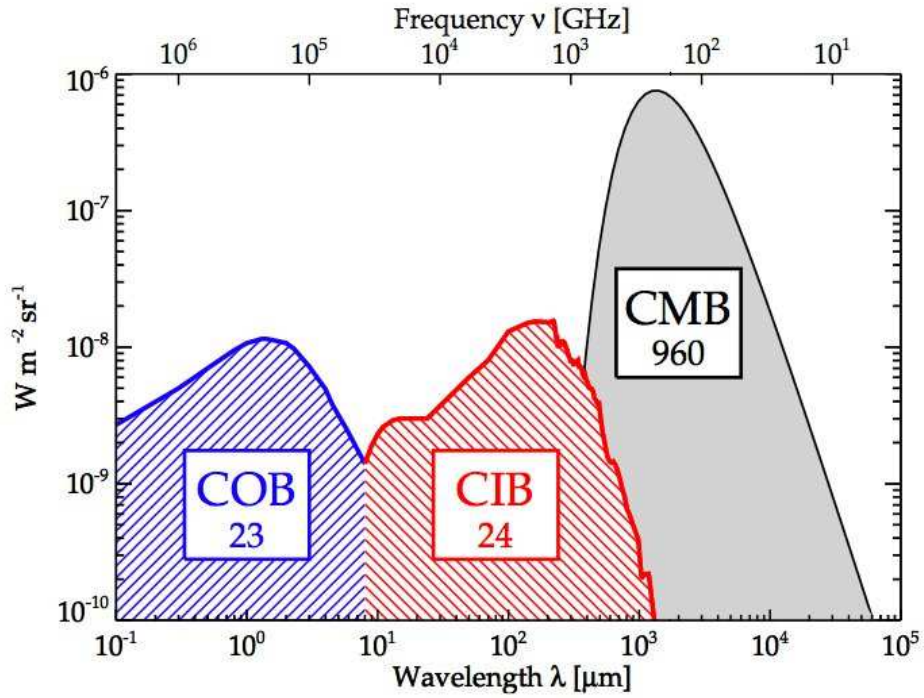


Figure 1.6: Spectral energy distribution (SED) of the cosmic optical, IR and microwave backgrounds with approximate brightness (nW m$^{-2}$ sr$^{-1}$) given in the boxes (Dole et al., 2006).

– are missed by optical and UV surveys. Although dwarfed by the cosmic microwave background, the CIRB intensity is still at least as high as the integrated optical light from galaxies. The largest contribution to the CIRB comes from IR-luminous galaxies, emitting most of their energy between rest-frame 8 and 1000 $\mu$m. These are usually classified as either luminous IR galaxies (LIRGs, with $10^{11-12}\,L_{\odot}$), ultraluminous IR galaxies (ULIRGs, $10^{12-13}\,L_{\odot}$) or hyperluminous IR galaxies (HLIRGs or HyLIRGs, with $>10^{13}\,L_{\odot}$).

Multi-wavelength studies of IR-luminous galaxies have revealed that they are often the result of mergers between gas-rich galaxies (Engel et al., 2010). Their emission is powered by either starbursts, i.e. radiation from young stars, or by AGN, i.e. radiation due to accretion onto a SMBH, or by both (e.g. Ivison et al., 1998; Ivison et al., 2010). In both cases the resulting radiation is absorbed by dust and re-radiated at longer wavelengths. The temperature of the dust, as inferred from fits to its IR/submm SED, is often taken as a diagnostic of the original source of the radiation – the dust surrounding an accreting SMBH is expected to be warmer than the dust typically found

in star-forming regions, though this is not a clean diagnostic.

Observations of LIRGs in the local Universe suggest they are usually dominated by starbursts – high-resolution radio images reveal tens of radio supernovae, the end products of short-lived, massive stars; AGN may dominate the HyLIRG population. The connection between AGN and starbursts is a topic of intense debate, since AGN provide a means of terminating star formation in galaxies that would otherwise exhaust their gas too quickly – so-called 'feedback'.

### 1.2.1 Submm-selected galaxies

Submm observations have an important advantage if one wishes to find and study distant, dusty galaxies. On the Rayleigh-Jeans portion of the far-IR SEDs of such galaxies, the flux density increases rapidly with frequency (see Figure 1.5). This results is a so-called 'negative $K$-correction', which means that ever more distant galaxies ($z \sim 0.5$ and beyond) are observed at wavelengths ever closer to the rest-frame peak of their SEDs. Their brightness does not dim as one would normally expect. The inverse-square law is balanced by the $K$ correction and we can select galaxies in a manner that is virtually independent of their distance from us (Blain & Longair, 1993).

Early submm surveys (e.g. Smail et al., 1997; Hughes et al., 1998; Eales et al., 1999) found a population of very luminous, dusty galaxies at high redshift – SMGs or 'SCUBA galaxies', named after the instrument with which they were first seen (Holland et al., 1999). SMGs are usually very faint in the optical waveband (Smail et al., 2002; Dunlop et al., 2004) and it is often near-impossible to determine which of the many near-coincident optical or IR galaxies are responsible for the submm (rest-frame far-IR) emission. In the local Universe, SFGs are known to follow the far-IR/radio correlation as the origins of both radio and far-IR emission relate to young, massive stars (Yun et al., 2001). Recent studies have hinted that the far-IR/radio correlation holds at high redshift (Appleton et al., 2004; Ibar et al., 2008, cf. Ivison et al. 2010a,b) so we expect to see faint radio emission from SMGs and this is how they have typically been pinpointed (Ivison et al., 1998; Smail et al., 2000; Eales et al., 2000; Ivison et al., 2002, 2007; Biggs et al., 2011). The low surface density of radio sources means that counterparts are often unique and statistically robust.

With their positions thus determined, deep optical spectroscopy revealed that a significant fraction of SMGs lie at $z \sim 1 - 3$ (Chapman et al., 2005). With redshifts in hand, observations of molecular lines such as CO were possible and these revealed

evidence of massive quantities of molecular gas – the fuel for star formation (Frayer et al., 1998, 1999; Greve et al., 2005; Tacconi et al., 2006, 2008). The typical star-formation rates (SFRs) of these massive galaxies are $\sim 10^3\,M_\odot$ and they are sufficiently abundant to make a significant (perhaps dominant) contribution to the global SFR in the early Universe. They are also a key part of the phenomenon known as 'downsizing' – the idea that massive galaxies form early, followed by less massive galaxies in the $z < 1$ timeframe. The study of SMGs thus contributes towards our understanding of galaxy formation and evolution.

As well as providing accurate positions, and estimates of distance (Carilli & Yun, 1999), radio observations can be used to distinguish between AGN and starbursts – by looking at the spatial extent of the emission (AGN might display jets, or highly concentrated emission with very high brightness temperatures), by looking for large deviations from the far-IR/radio correlation (so-called 'radio-excess AGN' – Donley et al. 2005b) and also via unusually steep or flat radio spectral indices (e.g. Ibar et al., 2009; Ibar et al., 2010a).

### 1.2.2 The far-IR/radio correlation

First discovered by van der Kruit (1971), the far-IR/radio correlation is a very tight correlation observed between the far-IR and radio luminosities of SFGs, over a large range of both luminosities (see Figure 1.7). The *Infrared Astronomy Satellite (IRAS)* survey highlighted the universality and low scatter of this correlation (Helou et al., 1985), bringing to light its significance as a tool to probe of the nature of sources detected in these bands. The far-IR/radio correlation can be described by the $q$ parameter (Helou et al., 1985):

$$q = \log\left(\frac{\mathrm{FIR}}{3.75\times10^{12}\,\mathrm{W m^{-2}}}\right) - \log\left(\frac{S_\nu}{\mathrm{W\ m^{-2}\ Hz^{-1}}}\right) \tag{1.1}$$

The correlation holds for SFGs as emission in both wavebands have the same source – massive stars, $M > 8\,M_\odot$. The far-IR emission is dust-reprocessed thermal radiation, the result of optical and UV light from massive stars being absorbed by surrounding dust, much of which may have formed following SNe explosions (e.g. Dunne et al., 2003; Barlow et al., 2010). Dust temperatures are typically between 20 and 200 K and the thermal radiation has a modified blackbody spectrum, peaking at rest-frame $\sim 100\,\mu$m. As discussed above, the radio synchrotron emission comes from

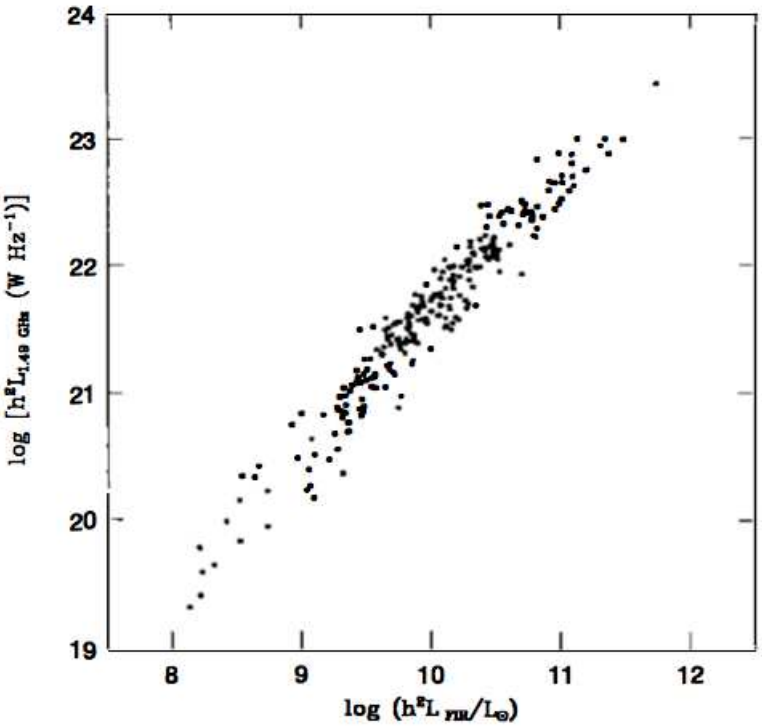


Figure 1.7: The far-IR/radio correlation as seen for a sample of SFGs (Condon, 1992).

SNRs, the product of massive stars. The correlation between the two luminosities can be exploited as a useful tool (Ivison et al., 2010a, and references therein) to:

(a) obtain an estimate of the SFR from the far-IR or radio luminosities (Condon, 1992; Bell, 2003);

(b) obtain distance estimates to dusty starbursts galaxies, using the submm-to-radio spectral index (Carilli & Yun, 1999);

(c) distinguish SFGs from AGN as the latter may be observed to have a radio excess, deviating significantly from the correlation (e.g. Donley et al., 2005b).

## 1.3 Active Galactic Nuclei

AGN emit very high luminosities from a very concentrated core and/or from extended radio jets/lobes. The compact core has a scale of $\approx 0.01$ parsec, yet has a mass of up to $10^9\ M_\odot$. This large amount of energy is the gravitational potential released as material

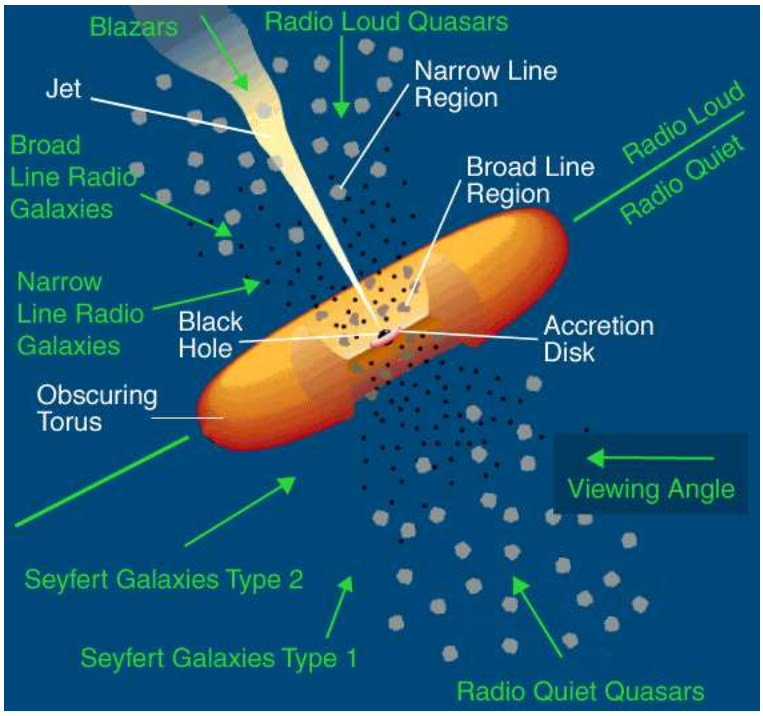


Figure 1.8: Unified model of an AGN, showing the properties seen by a variety of plausible observers from lines of sight. Image credit: NASA.

from the surrounding disk is accreted down onto the central SMBH. The AGN structure is believed to comprise a SMBH surrounded by a toroidal dust structure (the torus). The accretion also gives rise to high energy jets, streaming from the nucleus. The exact process through which this occurs is not yet clear. Typical sizes of the accretion disk are of the order of a few astronomical units (AU), making direct observation of the accretion process impossible with current observing facilities. Global Very Long Baseline Interferometry of the SMBH at the centre of our own galaxy, using the submm facilities including the Atacama Large Millimetre/Submm Array, will probe close to this scale in the coming years.

The apparent diversity of AGN has been explained as essentially an orientation effect (Antonucci, 1993): this unification scheme is illustrated in Figure 1.8, showing how different viewing angles lead to different observed properties.

AGN can broadly be divided into the radio-loud and radio-quiet categories. Radio-quiet AGN are further divided into two classifications: Seyfert 1 (S1) and Seyfert 2 (S2). S1 objects display broad-line regions (with typical line widths, $\sim 10{,}000\,\mathrm{km\,s^{-1}}$) and narrow-line regions (typical line widths, $\lesssim 1{,}000\,\mathrm{km\,s^{-1}}$) in their spectra; S2

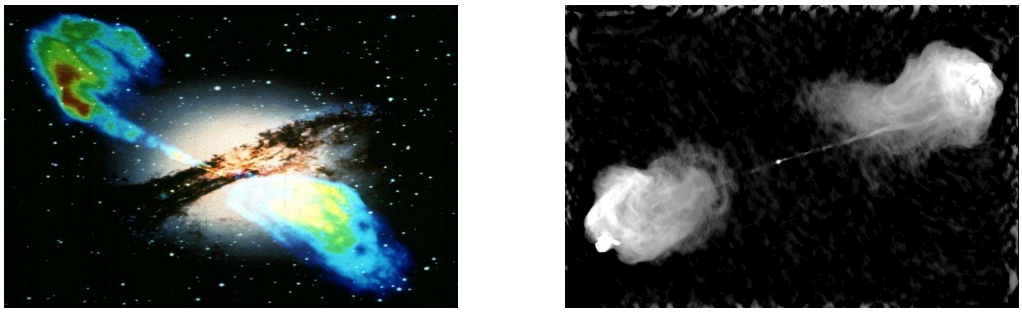

(a) (b)

Figure 1.9: *Left:* Radio and optical composite image of Centaurus A (labelled a). Image credit: HubbleSite. *Right:* Bright radio source, Cygnus A, displaying jets streaming from a core to radio lobes (labelled b). Image credit: https://eee.uci.edu/clients/bjbecker/ExploringtheCosmos.

objects display only narrow lines. At X-ray wavelengths, S1s have stronger emission than S2s. Radio-loud AGN are believed to have a core-dominated source with jets close to the line of sight.

As part of this thesis I aim to determine the fraction of AGN and SFGs amongst the faint radio population. Distinguishing SFGs from AGN-dominated sources using multi-wavelength diagnostics will be discussed in Chapter 3.

### 1.3.1 Radio galaxies

Radio galaxies were the first extragalactic radio sources to be found due their high luminosities ($\sim 10^{34}$–$10^{39}\,\mathrm{W\,Hz^{-1}}$). These are commonly hosted by giant ellipticals and are some of the largest structures in the Universe, spanning up to 3 Mpc – much larger than their optically visible counterparts (e.g. Figure 1.9(a)). Emission from radio galaxies is usually seen as long, thin jets extending away from a bright, central core. These jets feed into two large, radio-emitting regions known as radio lobes. The lobes form as a result of diffuse gas exerting a ram pressure and stopping the jets, giving rise to hotspots of radiation. Figure 1.9(b) shows one of the brightest radio galaxies, Cygnus A – a typical example of a system with these features.

The jets streaming out from the nucleus are composed of hot matter propelling outwards as a result of the large energy being released from accretion of in-falling material onto the central SMBH. Away from the nucleus, radio galaxies are classified by the interaction of the jets with the surrounding gas. This follows the classification of Fanaroff-Riley (Fanaroff & Riley, 1974; Kawakatu et al., 2009). FR I sources have

an edge-darkened morphology, with subsonic jets near the nucleus. They do not have very bright lobes. The jets of FR I sources sometimes appear to curve due to distortion of the jet stream by the surrounding gas. In some cases only one jet can be seen – an effect of relativistic beaming, i.e. the relativistic motion of particles in the beam appear to boost its intensity in the direction of a beam that is close to the line of sight, reducing the intensity of the opposing beam. FR II sources have supersonic jets with the bulk of emission coming from the lobes. FR I sources are weaker emitters than the FR II sources.

## 1.4 The origin of radio emission and interferometry

### 1.4.1 Synchrotron radiation

Synchrotron emission arises as a result of a charged particle being accelerated in a magnetic field. Although it makes a contribution at shorter wavelengths, it is primarily detected through radio emission. A brief introduction to synchrotron emission will be presented here; a more detailed treatment of the concepts outlined here can be found in Longair (2010) and Burke & Graham-Smith (2002).

#### Motion of an electron around a magnetic field

The gyration of a non-relativistic electron, of charge, *e*, and mass, *m*, in a magnetic field, *B*, will have an angular frequency

$$\omega_{\rm e} = \frac{e\,B}{m\,c} = 2\pi\,\nu_{\rm e}. \tag{1.2}$$

A relativistic electron with energy, $\gamma m_0 c^2$, also follows a spiral path along a magnetic field line, but will have an angular frequency which is lower by a factor $\gamma$, as the inertial masses are higher by this factor:

$$\omega_{\rm r} = \frac{\omega_{\rm e}}{\gamma}, \tag{1.3}$$

where $\gamma \gg 1$ for a relativistic electron.

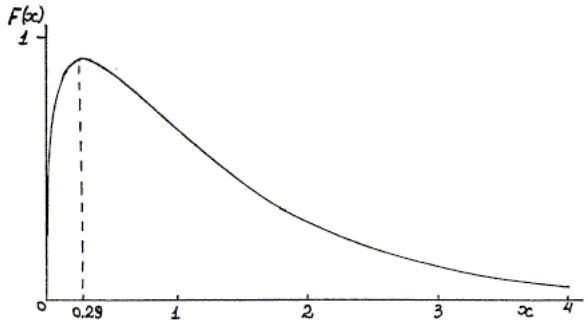


Figure 1.10: The function $F(x)$ describes the synchrotron spectrum. Taken from Ginzburg & Syrovatskii (1965).

### Synchrotron spectrum

The radiation from a relativistic electron as it gyrates in the magnetic field is seen as a narrow beam of width, $\approx 1/\gamma$. As the electron gyrates around the magnetic field, it follows a helical path and radiates a narrow beam of width, $1/\gamma$, in its direction of motion. Each time the beam crosses the line of sight of an observer, a short pulse is detected. The duration over which the pulse can be observed is given by $\Delta t = 1/(\gamma^3 \nu_{\rm r})$. The Fourier spectrum of this pulse is concentrated about a critical frequency given by

$$\nu_{\rm c} = \frac{3}{2}\,\gamma^3\,\nu_{\rm r}\,\sin\alpha. \tag{1.4}$$

The pitch angle, $\alpha$, is defined as the angle between the magnetic field line and the velocity component of the electron. The peak emission, however, has a value $\nu_{\rm max} = 0.29\,\nu_{\rm c}$.

The synchrotron spectrum is often expressed in terms of the parameter, $x = \nu/\nu_{\rm c}$. The power spectrum of the radiation is

$$P(\nu)\,{\rm d}\nu = \sqrt{3}\,\frac{e^3\,B\,\sin\alpha}{m\,c^2}F(x)\,{\rm d}\nu \tag{1.5}$$

where $F(x)$ describes the integral of a modified Bessel function of order 5/3:

$$F(x) = x\int_x^\infty K_{5/3}(z)\,{\rm d}z. \tag{1.6}$$

Figure 1.10 shows the function $F(x)$ and the synchrotron spectrum for a single

electron. As the total radiation is a sum of its parallel (||) and perpendicular ($\perp$) components, it can be decomposed to give

$$P_{\perp,||}(\nu) = \frac{\sqrt{3}}{2}\frac{e^3\,B\,\sin\alpha}{m\,c^2}\begin{cases} F(x)+G(x) & (\perp) \\ F(x)-G(x) & (||) \end{cases} \tag{1.7}$$

where $G(x) = \int_x^\infty K_{2/3}(z)\,\mathrm{d}z$.

Defining the magnetic energy density, $U_\mathrm{B}$, and the Thomson scattering cross-section $\sigma_\mathrm{T}$ as

$$U_\mathrm{B} = \frac{B^2}{8\pi} \quad \text{and} \quad \sigma_\mathrm{T} = \frac{8\pi\,e^4}{3\,m^2\,c^4}, \tag{1.8}$$

then integrating over all frequencies, averaging over all pitch angles and assuming an isotropic distribution of electrons will give the synchrotron power radiated by a relativistic electron as

$$P = \frac{4}{3}\,\gamma^2\,c\,\sigma_\mathrm{T}\,U_\mathrm{B}. \tag{1.9}$$

Based on this, the half-life of the radiation is then

$$t_{1/2} = m\,c^2\left(\frac{4}{3}\,\gamma\,c\,\sigma_\mathrm{T}\,U_\mathrm{B}\right)^{-1}. \tag{1.10}$$

For a cosmic-ray electron with an energy of 10 GeV in a 3-$\mu$G field, the lifetime of the radiation will be of the order $10^8$ yr. This is an important result as radio observations of synchrotron emission are probes of very recent star formation (Condon, 1992).

### Synchrotron emission from a distribution of electron energies

The synchrotron spectrum discussed above is for a single electron and these results will now be extrapolated for the case of a distribution of electron energies. The energy distribution of electrons from a non-thermal source, as well as cosmic-ray electrons, can be approximated by a power-law

$$N(E)\,\mathrm{d}E = C\,E^{-p}\,\mathrm{d}E \tag{1.11}$$

where $p$ is the slope of the electron energy spectrum and $N(E)\,\mathrm{d}E$ is the number of electrons per unit volume in the energy interval, $E + dE$. The power spectrum for a distribution of electron energies is then

$$P(\nu)\,\mathrm{d}\nu = N(E)\,\mathrm{d}E \times P_{\mathrm{single\,electron}}. \tag{1.12}$$

From $\nu = 3\,\omega_g\,E^2/(4\pi\,m_0^2\,c^4)$, $\mathrm{d}\nu = 3\,\omega_g/(2\pi\,m_0^2\,c^4)E\,\mathrm{d}E$. Substituting $\mathrm{d}\nu$ and $P_{\mathrm{single\,electron}}$ into Equation 1.12 then gives

$$P(\nu)\,\mathrm{d}\nu = C\,E^{-p}\,\frac{4}{3}\,c\,\sigma_{\mathrm{T}}\,U_{\mathrm{B}}\left(\frac{E}{m_o\,c^2}\right)^2\frac{2\pi\,m_0^2\,c^4}{3\,\omega_g\,E}\,d\nu \tag{1.13}$$

and so

$$P(\nu) \propto E^{1-p}\,B \propto \left(\frac{\nu}{B}\right)^{\frac{1-p}{2}}\,B \propto \nu^{\frac{1-p}{2}}B^{\frac{1+p}{2}}. \tag{1.14}$$

If the radio spectral index is then defined as $\alpha = (1-p)/2$, the observed flux density can be parameterised as $S_\nu \propto \nu^{-\alpha}$ where, typically, $0.5 \leq \alpha \leq 1$.

### Synchrotron self-absorption

Assuming a source of synchrotron radiation follows a power-law spectrum, its intensity will continue to rise at lower frequencies since $S \propto \nu^{-\alpha}$. However, as dictated by thermodynamic equilibrium, this is not possible as the brightness temperature $T_{\mathrm{b}}$ (obtained from the intensity, $I_\nu = 2\,k\,T_{\mathrm{b}}/\lambda^2$) cannot exceed the temperature of the electrons that are radiating. Hence, at some point the spectrum will need to turn over; once it has turned over, the source is self-absorbed.

Although the electron distribution is non-thermal it is defined by a relativistic Maxwellian distribution, where the concept of temperature can still be used. The effective temperature of the electrons is then given by

$$T_{\mathrm{eff}} = \frac{\gamma m_0\,c^2}{3\,k} \simeq \frac{m_0\,c^2}{3\,k}\left(\frac{\nu}{\nu_{\mathrm{e}}}\right) \tag{1.15}$$

As mentioned above, a synchrotron source following a power-law will become self-absorbed and so the radiation temperature must equal the electron temperature. Therefore,

$$S_\nu = \frac{2\,k\,T_{\mathrm{b}}\,\Omega}{\lambda^2} = \frac{2\,m_0\,\Omega}{3\,\nu_e^{1/2}}\,\nu^{5/2} \propto \nu^{5/2}\,\Omega\,B^{-1/2} \tag{1.16}$$

where $\Omega$ is the the solid angle subtended by the source. The turn-off at $\nu^{5/2}$ is a point at which the source goes from being optically thick to optically thin. If $B$ is known,

self-absorption allows for $\Omega$, the size of the source to be determined.

### 1.4.2 Radio interferometry

Having examined the emission mechanism responsible for radio waves, let us now look at the detection of these radio waves. Due to the large wavelength of radio waves, even the largest steerable dishes ($\sim$100 m, e.g. Green Bank Telescope and Effelsberg) would not be able to achieve sub-arcsecond angular resolutions. Building steerable dishes much larger than this presents severe technical challenges, such as correcting for gravitational sagging and maintaining tracking accuracy.

Interferometry is a technique used in radio astronomy to combine signals from two or more observing elements (e.g. antennas) to achieve the effective resolution of a single large dish, with a diameter defined by the furthest distance between two observing elements. In this section, the basic concepts of interferometry will be introduced, including any assumptions made in the treatment of radio observations (*note that bold-type fonts represent vector quantities*).

#### The observed electromagnetic field

The gyration of electrons in a magnetic field causing synchrotron emission at a location $\mathbf{r}$ and time $t$ is observed as a time-variable electromagnetic (EM) field, $\mathbf{E}(\mathbf{r},\ t)$. The response of a radio antenna to this EM-field is a signal $v(\mathbf{r},\ t)$, which will be proportional to $\mathbf{E}(\mathbf{r},\ t)$. The intensity of the radiation is then given by

$$I(\mathbf{r}) = \langle v(\mathbf{r}, t)\, v^*(\mathbf{r}, t) \rangle, \tag{1.17}$$

where, $v^*$ is the complex conjugate of $v$. Some assumptions can be made about the observed radiation:

(a) while the field varies with time, it fluctuates in an ergodic manner, such that measuring a time-averaged signal over a relatively long period allows for short-period variability to be ignored;

(b) the source is distant enough to be "flat" against a celestial sphere and only the surface brightness of the object can be measured; no information about the depth of the information can be inferred;

(c) the field is a scalar field and any polarisation effects are ignored, as the signal can be made to be quasi-monochromatic by the use of filters.

The signal can be measured from two points, $\mathbf{r}_1$ and $\mathbf{r}_2$. Coherence theory explains the correlation of two measurements at these two points, some time $\tau$ apart:

$$\Gamma(\mathbf{r_1}, \mathbf{r_2}, \tau) = \langle v(\mathbf{r_1}, t)\, v^*(\mathbf{r_2}, t+\tau)\rangle \tag{1.18}$$

and the degree of coherence is given by

$$\gamma(\mathbf{r_1}, \mathbf{r_2}, \tau) = \frac{\Gamma(\mathbf{r_1}, \mathbf{r_2}, \tau)}{[I(\mathbf{r_1})\, I(\mathbf{r_2})]}. \tag{1.19}$$

When $|\gamma|$=1, the radiation is considered to be coherent; it is incoherent if $|\gamma|$=0; values in between indicate partial coherence. The case where $\tau = 0$, $\Gamma(\mathbf{r_1}, \mathbf{r_2}, 0)$ is known as the spatial coherence function. For a source with spatially incoherent radiation, the van Cittert-Zernike theorem relates the spatial coherence function to the sky brightness:

$$\Gamma(\mathbf{r_1}, \mathbf{r_2}) = \int I(\mathbf{s}) e^{-2\pi i s(\mathbf{r_1}-\mathbf{r_2})/c}\, d\Omega, \tag{1.20}$$

where $I(\mathbf{s})$ is the intensity of a source at the distance of a unit vector, $\mathbf{s}$. The spatial coherence function depends on the relative distance, $\mathbf{r}_1$-$\mathbf{r}_2$; the correlation properties of the field can be inferred by keeping one position fixed and moving the second. A schematic of this measurement is illustrated in Figure 1.11.

### Interferometry

An interferometer is a device used to measure the spatial coherence function. In this section, the response of an interferometer to an incoming signal is discussed. The case of a simple two-element interferometer will be considered as interferometric arrays are simply an ensemble of two-element interferometers.

For the case of two antennas, separated by a baseline distance, $\mathbf{b}$, pointing at a source in the direction of a unit vector, $\mathbf{s}$, one antenna will receive the signal at a time $\tau_{\rm g}$ after the other. This time delay is known as the geometric delay and is given by $\tau_{\rm g} = \mathbf{b}.\mathbf{s}/c$, where $c$ is the speed of light. The response produced by each antenna is passed through an amplifier, where the signals are filtered to select a frequency bandwidth, $\Delta\nu$, and desired polarisation. The signals are then combined in a correlator, where

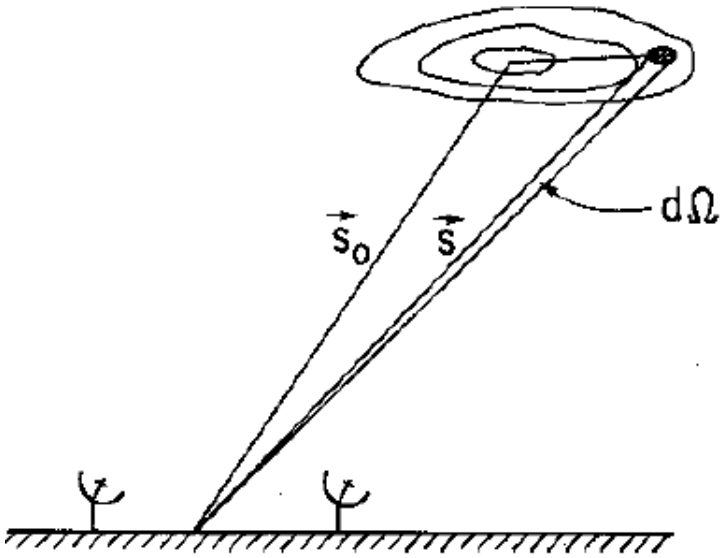


Figure 1.11: Schematic diagram illustrating the vectors used to define the measurement of source coherence (Taylor, Carilli & Perley 1999).

they are passed through a voltage-multiplier followed by a time-averaging integrator. For antennae responses of $V_1(t) = v_1 \cos 2\pi\,\nu(t - \tau_{\rm g})$ and $V_2(t) = v_2 \cos 2\pi\,\nu(t)$, the output from the correlator will then be proportional to $\langle V_1(t)\, V_2(t)\rangle$, i.e. the output is given by

$$r(\tau_{\rm g}) = v_1\, v_2 \cos 2\pi\,\nu\,\tau_{\rm g}. \tag{1.21}$$

The rotation of the Earth causes a slow variation of $\tau_{\rm g}$, resulting in the cosine factor producing a fringe pattern.

The response of an interferometer can also be expressed by the radio brightness of the source integrated across the whole sky. Let $I(\mathbf{s})$ be the brightness of the source in the direction of the unit vector $\mathbf{s}$ at frequency, $\nu$, observed with an antenna of effective collecting area, $A(\mathbf{s})$. The power incident on each antenna over a frequency bandwidth, $\Delta\nu$, in a solid angle element, $\mathrm{d}\omega$, is $A(\mathbf{s})I(\mathbf{s})\Delta\nu\mathrm{d}\Omega$. The correlator output (Equation 1.21) is proportional to the incident power and to the cosine term. Then, omitting constant gain factors, the correlator output for a signal integrated over the entire surface of the celestial sphere, $S$, is given by

$$r = \Delta\nu \int_S A(\mathbf{s})\, I(\mathbf{s}) \cos \frac{2\pi\, \nu \mathbf{b} \cdot \mathbf{s}}{c}\, \mathrm{d}\,\Omega. \tag{1.22}$$

Integrating over the entire surface of the sphere rather than over the angular area for which the source is defined has little effect as the integrand drops to low values outside of the angular area of the source. Three assumptions are made in the derivation of Equation 1.22: (1) $\Delta\nu$ is small enough such that any variation in *A* or *I* with $\nu$ is negligible; (2) the source is far enough so that any incoming radiation can be taken as planar field and (3) the radiation from the source is spatially incoherent.

As discussed above, the measurement of the spatial coherence can be accomplished by keeping one position fixed (a phase tracking centre, $\mathbf{s}_0$ hereafter) and moving the second. This is the conventional way in which an interferometric image is constructed. Defining the position vector, $\mathbf{s} = \mathbf{s_0} + \sigma$, Equation 1.22 can be re-written as

$$\begin{aligned} r = \Delta\nu\, \cos\left(2\pi\nu \frac{\mathbf{b}\cdot\mathbf{s_0}}{c}\right) \int_S A(\sigma) I(\sigma) \cos \frac{2\pi\nu \mathbf{b}\cdot\sigma}{c}\, \mathrm{d}\Omega \\ -\Delta\nu \sin\, \left(2\pi\nu \frac{\mathbf{b}\cdot\mathbf{s_0}}{c}\right) \int_S A(\sigma) I(\sigma) \sin \frac{2\pi\nu \mathbf{b}\cdot\sigma}{c}\, \mathrm{d}\Omega. \end{aligned} \tag{1.23}$$

A visibility – a complex quantity – is a measure of the coherence of the electromagnetic field and is defined as

$$V = |V| e^{i\phi_v} = \int_S A'(\sigma) I(\sigma) e^{-2\pi i \nu \mathbf{b}\cdot\sigma/c}\, \mathrm{d}\Omega, \tag{1.24}$$

where $A'(\sigma) = A(\sigma)/A_0$ is the normalized antenna response pattern and $A_0$ is the response at the beam centre. Separating Equation 1.24 into its real and imaginary parts gives

$$|V| \cos\phi_V = \int_S A'(\sigma) I(\sigma) \cos \frac{2\pi\nu \mathbf{b}\cdot\sigma}{c}\, \mathrm{d}\Omega \tag{1.25}$$

and

$$|V| \sin\phi_V = -\int_S A'(\sigma) I(\sigma) \frac{2\pi\nu \mathbf{b}\cdot\sigma}{c}\, \mathrm{d}\Omega. \tag{1.26}$$

Substituting these into Equation 1.23 will then give

$$r = A_0 \, \Delta\nu \, |V| \cos \left( \frac{2\pi\nu \mathbf{b} \cdot \mathbf{s_0}}{c} - \phi_V \right). \tag{1.27}$$

The cosine term represents the phase and amplitude of the fringe pattern; making this measurement and then calibrating for the amplitude and phase of the visibilities is the conventional way in which radio interferometric images are interpreted. The brightness distribution of the radio source is determined by performing an inverse Fourier transform on Equation 1.24.

A coordinate system can now be introduced to make measurements of Equation 1.27. The coordinate system commonly used is one where the antennae baselines are taken as a vector with components (*u, v, w*), where *u* is towards the east, *v* is towards the north and *w* is the direction pointing to the source. This coordinate system is measured in wavelengths. The position of sources on the sky are given in terms of (*l, m*), which represent the direction cosines measured with respect to the *u* and *v* axes. Hereafter, the measurement will be taken to be confined to a plane, i.e. *w* is in the direction phase tracking centre, $\mathbf{s_0}$ and $w = 0$. The parameters discussed above in the derivation of the response from an interferometer can be re-defined using this coordinate system:

$$\frac{\nu \, \mathbf{b} \cdot \mathbf{s}}{c} = u \, l + v \, m \quad \text{and} \quad \mathrm{d}\Omega = \frac{\mathrm{d}l \, \mathrm{d}m}{\sqrt{1 - l^2 - m^2}}. \tag{1.28}$$

Substituting these into Equation 1.27 and taking the case where $|l|$ and $|m|$ are small then gives

$$V(u, v) = \int \int A'(l, m) \, I(l, m) \, e^{-2\pi i [ul + vm]} \, \mathrm{d}l \, \mathrm{d}m. \tag{1.29}$$

This gives a two-dimensional Fourier transform and the sky brightness can be obtained from the visibilities by inverting this relation:

$$A'(l, m) \, I(l, m) = \int \int V(u, v) e^{-2\pi i [ul + vm]} \, \mathrm{d}l \, \mathrm{d}m. \tag{1.30}$$

### 1.4.3 Instrumental effects

When dealing with interferometric datasets, the instrumental effects discussed below need to be considered (see Taylor, Carilli & Perley 1999).

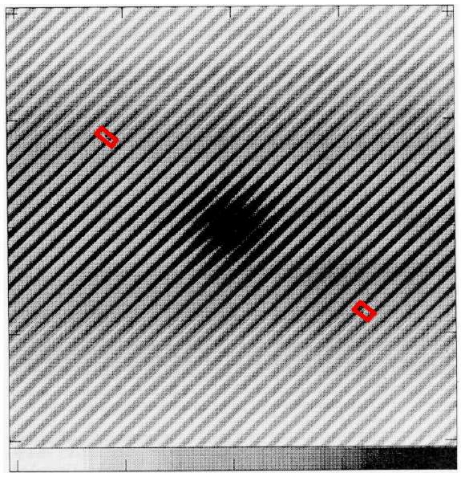

Figure 1.12: The figure shows a visibility function and the red boxes – the size of which is determined by the bandwidth – indicate a region over which source visibilities would be averaged. As a source visibility is not constant over this region, there will be a distortion in the image (Taylor, Carilli & Perley 1999).

### Bandwidth Smearing

Bandwidth smearing is an effect that results from observing with a finite bandwidth. It arises due to the averaging of visibilities by the correlator. The data in the correlator is recorded in consecutive time intervals and the only value retained is an average of the time interval. Smearing is a result of averaging the data over a period when there is significant change in the visibilities, as illustrated in Figure 1.12.

There are three approaches to estimating bandwidth smearing (Taylor, Carilli & Perley 1999) and each approach can be parameterised by the factor

$$\beta = \frac{\Delta\nu}{\nu_0}\frac{\theta}{\theta_{\rm beam}}, \tag{1.31}$$

where $\Delta\nu$ is the bandwidth of each observing channel, $\nu_0$ is the central observing frequency, $\theta$ is the distance of the source form the phase tracking centre and $\theta_{\rm beam}$ is the synthesised beam size (full width at half maximum for a point source). The following equations describe the three different approaches to bandwidth smearing ($I$ and $I_0$ are the observed and intrinsic peak flux densities, respectively):

- Assuming the case of a Gaussian bandpass and circular Gaussian tapering,

$$\frac{I}{I_0} = \frac{1}{\sqrt{1+\beta^2}} \quad \text{where} \quad \beta = \frac{\Delta\nu}{\nu}\frac{\theta}{\theta_{\rm beam}}. \tag{1.32}$$

Assuming the case of a square bandpass and circular Gaussian tapering,

$$\frac{I}{I_0} = \frac{\sqrt{\pi}}{\gamma\,\beta}\,\mathrm{erf}\,\frac{\gamma\,\beta}{2} \quad \text{where} \quad \gamma = 2\sqrt{\ln 2} \tag{1.33}$$

- Assuming the case of a square bandpass, no tapering and square (*u*,*v*) coverage

$$\frac{I}{I_0} = \frac{2}{\eta\,\beta}\,\mathrm{Si}\,\frac{\eta\,\beta}{2} \quad \text{where} \quad \mathrm{Si}(x) = \int_0^x (\frac{\sin t}{t})\,\mathrm{d}t \tag{1.34}$$

and $\eta$ =3.79.

The effect of bandwidth smearing is a reduction in the peak intensity and radial stretching of the source towards the pointing centre; note, however, that while peak intensity is reduced, the integrated flux density of the source is conserved.

The solution to this problem is to observe with a bandwidth that is narrow enough for bandwidth smearing to be negligible. This will however, result in loss of sensitivity. An alternative is to use an observing band – over which the source can be considered to have the same flux density – which can be divided up into narrow channels and then re-combined. The number of channels can be chosen so that each band is narrow enough for smearing to be negligible.

### Primary beam attenuation

Primary beam attenuation is the loss of antenna gain with radially increasing distance from the pointing centre. The response of a Jansky Very Large Array antenna at 1.4 GHz can be described by the following polynomial:

$$P = 1 - 1.343 \times 10^{-3}\chi + 6.579 \times 10^{-7}\chi^2 - 1.186 \times 10^{3}\chi^3 \tag{1.35}$$

and $\sqrt{\chi} = rf$, where *r* is the radial distance from the pointing centre (in arcmin) and *f* is the frequency (in GHz). Primary beam attenuation can be corrected for using this polynomial.

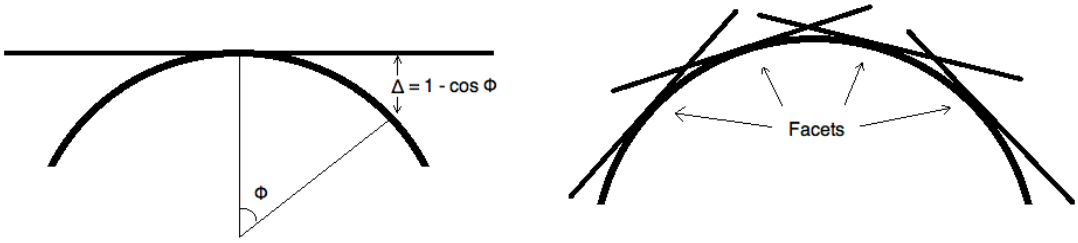


Figure 1.13: *Left:* A separation between the tangential plane and the celestial sphere of more than $\Delta = 1 - \cos\phi$ will cause a smearing effect. *Right:* Polyhedron imaging is a solution to the problem of smearing caused by non-co-planar imaging. The celestial sphere is approximated into smaller fields of view known as facets.

### Smearing due to non-coplanar imaging

The response of an interferometer (Equation 1.29) is a 2-dimensional Fourier transform that is only valid for co-planar baselines and for small fields of view. This presents a problem, especially at lower frequencies where the primary beam is large, when there is a need to image a relatively large area of the sky. Due to the curvature of the celestial sphere, sources will suffer a smearing effect when there is a large separation between the plane tangential to the observing direction and the celestial sphere. Taylor, Carilli & Perley (1999) show that the separation at which this becomes a problem is $\Delta = 1 - \cos\phi$, where $\phi$ is the angle from the phase-tracking centre (see Figure 1.13).

Polyhedron imaging is an approach to overcome the problem of smearing as a result of non-co-planar imaging. This technique requires the application of the small field approximation, such that the celestial sphere is approximated into a number of smaller tangent planes known as facets. Each facet will have visibility data that has been phase-shifted so that the centre of each facet coincides with a certain position on the celestial sphere; the centre of each facet is then also a phase centre. Figure 1.13 illustrates the polyhedron imaging technique.

### Time-average smearing

As a result of averaging the source visibility over a period when it is not constant, the rotation of the Earth can also produce smearing effects – time-average smearing. This is an important consideration for Earth-rotation synthesis arrays – interferometers that use the rotation of the Earth to fill the $(u, v)$ plane. Time-average smearing is more

Figure 1.14: The (Jansky) Very Large Array. Photo by Dave Finley, courtesy NRAO/AUI.

pronounced for longer baselines as they trace out a greater area in the (*u, v*) plane. Time-average smearing can be avoided by scheduling short integration times.

### 1.4.4 The (Jansky) Very Large Array

The primary dataset presented in this thesis was obtained with the Very Large Array (VLA) – now referred to as the Jansky Very Large Array, following a major programme of upgrades completed following the acquisition of the data discussed here. The VLA is a radio interferometer near Socorro in New Mexico, USA, run by the National Radio Astronomy Observatory. Since it was commissioned in 1980, the VLA has been used for a wide variety of astronomy programmes, as well as weather studies and satellite tracking.

The VLA comprises 27 antennas, each 25 m in diameter, in a Y-shaped configuration. The antennas are placed on tracks, so the VLA has the capability to be regularly re-configured. A-configuration provides the highest resolution, with antenna separations of up to 36 km; D-configuration is the most compact configuration, with maximum antenna separations of 1 km. The telescope switches between configurations every 4 months. The operating frequency range of the VLA is 0.3–50 GHz.

Details of data obtained for this thesis with the VLA will be discussed in Chapter 2.

## 1.5 Outline of thesis

In this thesis I present deep, new radio observations designed to study the nature of the faint radio population and to delineate the cosmic star-formation history of the Universe.

Radio observations of the UKIDSS UDS field are presented in Chapter 2, with a thorough description of the data reduction and imaging methodology and processes. The extraction of a robust catalogue is also presented in Chapter 2, using an interesting new technique to define the detection threshold and maximise catalogue reliability.

In Chapter 3, the radio data are cross-matched with complementary multi-wavelength data to distinguish between AGN and SFGs amongst the sub-mJy population, and as a function of flux density.

Chapter 4 presents a morphological analysis of the sub-mJy radio population, using recently obtained *Hubble Space Telescope* images of the CANDELS field within the UDS. This morphological analysis concentrates on delineating the merger activity amongst AGN and SFGs (and a matched control sample) as a function of redshift.

In Chapter 5 I study specific star-formation rates of $K$-selected galaxies as a function of stellar mass and redshift, through the use of panchromatic stacking. I also present the apparatus (two independent stacking methods) that I am currently using to delineate the history of cosmic star formation.

Finally, I present a succinct set of conclusions from my thesis in Chapter 6. The cosmology used throughout this thesis is $\Omega_{\Lambda} = 0.73$, $\Omega_m = 0.27$ and $H_0 = 71\,\mathrm{km\,s^{-1}\,Mpc^{-1}}$. All magnitudes, unless otherwise stated, are quoted on the AB system.

# Chapter 2

# Deep, high-resolution radio imaging of the UKIDSS Ultra Deep Survey

## 2.1 Introduction

Here, in Chapter 2, I present the centerpiece of this thesis, a wide-field, high-resolution, high-dynamic-range radio image of the Ultra Deep Survey (UDS) field, the deepest element of the United Kingdom Infrared (IR) Telescope IR Deep Sky Survey (UKIDSS – see Lawrence et al., 2007).

As we have seen in Chapter 1, radio surveys are an effective method of probing galaxy evolution and play an important role in the study of star-forming galaxies (SFGs) and active galactic nuclei (AGN). Dust-enshrouded SFGs and torus-obscured AGN are typically faint in the optical and near-IR wavebands, making selection of distant examples of these objects difficult. However, synchrotron radiation from highly relativistic particles interacting with magnetic fields in SFGs, and from collimated jets in AGNs, are detected at radio wavelengths, unperturbed by any intervening dust (Condon, 1992). This makes radio observations an excellent tracer of star-formation and AGN activity, though disentangling these two processes has always proved rather difficult. It is clear, however, that radio source counts above a flux density of 1 mJy at 1.4 GHz are dominated by nuclear-driven emission from quasars and luminous radio galaxies. Below 1 mJy, the radio source counts – normalised to a Euclidean Universe – flatten. These galaxies are believed to comprise a different population consisting mainly of SFGs and faint AGNs (e.g. Ibar et al., 2009; Strazzullo et al., 2010; Padovani et al., 2011), but it is fair to say that the nature of the sub-mJy radio population is not

yet well understood. Amongst other things, the relative fractions of SFGs and AGNs contributing to this population is still debated hotly. It has been suggested that radio-quiet AGNs are more common than their radio-loud counterparts and could play an important role in galaxy evolution (e.g. Strazzullo et al. 2010, cf. Simpson et al. 2006).

If acquired with suitable angular resolution, radio observations are an excellent method of obtaining accurate positional information for galaxies detected in surveys with lower spatial resolution, such as those conducted with far-IR or submm cameras. Wide-field radio observations are often used as a high-resolution proxy for submm observations (e.g. Ivison et al., 2007; Biggs et al., 2011), exploiting the well-known correlation between far-IR and radio luminosities (Helou et al., 1985) and being more economical than the object-by-object approach using submm interferometers (e.g. Younger et al., 2007) due to the large primary beam, $\sim 30$ arcmin FWHM, of a typical radio interferometer like the VLA at 1.4 GHz. Indeed, the radio data I shall present in what follows have been used already to study submm-selected galaxies (SMGs – e.g. Ikarashi et al., 2011; Michalowski et al., 2012), and I present some new identification work for the SCUBA-2 Cosmology Legacy Survey towards the end of this chapter.

Deep, high-resolution radio imaging of extragalactic 'deep fields' – where suitably deep, multi-wavelength data are available – should improve our understanding of this faint radio population, thereby testing and constraining current theories of galaxy formation and evolution. The complementary data are essential to determine the true nature of faint radio galaxies – their dominant emission mechanism, their redshifts, masses, star-formation rates, etc.

Probing fainter still, the so-called 'stacking' technique (e.g. Dole et al., 2006) allows us to explore the properties of the radio population that lies below the conventional detection limits that can be achieved by radio telescopes in reasonable integration times (e.g. Boyle et al., 2007; Karim et al., 2011), thereby probing low-luminosity or high-redshift populations. Dunne et al. (2009), for example, studied the properties of $K$-selected[1] galaxy populations using a stacking approach to investigate the star-formation history of sources at flux densities an order of magnitude fainter than previously possible. One of the issues highlighted by Dunne et al. was the relatively small overlap between the narrow radio map presented by Ivison et al. (2007) of the particular deep field used for that study, the UDS[2] and the much wider ($\approx 0.6\,\mathrm{deg}^2$)

[1] In this context, $K$ is a broadband near-IR filter, covering 2.03–2.37 $\mu$m (50-per-cent cut-on and cut-off).

[2] The UDS is centred at $\alpha_{\mathrm{J2000}} = 2^{\mathrm{h}}18^{\mathrm{m}}00^{\mathrm{s}}$ and of $\delta_{\mathrm{J2000}} = -05^{\mathrm{d}}04'20''$.

optical and near-IR data available in the UDS. The UDS is the deepest element of UKIDSS (Lawrence et al., 2007) and is currently the deepest publicly available wide-area near-IR survey, with photometric redshifts for >100,000 galaxies and a wealth of other multi-wavelength data (e.g. Warren et al., 2007; Cirasuolo et al., 2010).

As we shall see in what follows, wide-field, high-resolution radio imaging is a challenging technique, hence the relative rarity of such images in the literature. To reach sensitivities necessary to explore the faint radio population, we must achieve a dynamic range of $\gtrsim$10,000, where this is defined as the ratio of the brightest flux density per synthesised beam in the image (typically around 100 mJy beam$^{-1}$ in a well-chosen deep field at 1.4 GHz for a map with $\sim$1.5-arcsec spatial resolution) to the noise level (typically $\approx$10 $\mu$Jy beam$^{-1}$). We must accomplish this in the presence of radio-frequency interference (RFI) from the Sun and from our fellow inhabitants of planet Earth. We must also minimise the effects of bandwidth smearing, which reduces the peak flux density of sources located a long way from the phase centre in maps with high spatial resolution, potentially eliminating them from catalogues. The primary goal of the radio imaging described here was to achieve excellent sensitivity and resolution across the entire UDS region, without missing faint sources due to pernicious effects of bandwidth smearing.

The UDS field is well suited to deep radio observations as it does not contain any particularly bright radio sources that might compromise sensitivity via the dynamic range limitations mentioned earlier, allowing observations to reach the very faint flux density levels ($S_{1.4\mathrm{GHz}} \leq 100\,\mu$Jy) where current controversies about the nature of the radio population are focussed.

## 2.2 Observations

The goal of our new observations was to produce a deep map of the entire UDS region at roughly $3\times$ the resolution and $2\times$ the depth of previous 1.4-GHz wide-field UDS radio imaging, as published by Simpson et al. (2006).

Simpson et al. (2006) divided the UDS field into 14 pointings, each separated by 15 arcmin, as listed in Table 2.1. B-configuration data were obtained for all 14 pointings during 2001 May and 2002 August and September. The total observing time per pointing was 3.6 hr. All the pointings were then observed again during a move from C to DnC (hereafter DnC) configurations in 2003 January, for a total of

0.1 hr per pointing to acquire coverage of the shortest possible VLA baselines. Some A-configuration data were also acquired, over the course of 13 nights during 2003 July, August and September, mainly for the central three pointings (pointings 1–3 in Table 2.1), with only short observations of the other 11 pointings ($\sim 1$ hr each). These $\sim 60$ hr of observations were presented by Ivison et al. (2007).

Using the same pointing grid as Simpson et al. (2006) and Ivison et al. (2007) for subsequent work means that it is relatively easy to combine data already acquired in the different configurations. One might opt for closer spacings if one were designing a new, optimal high-resolution survey, to minimise the effects of bandwidth smearing, but it would be necessary to re-acquire the short spacings to ensure sensitivity to large-scale emission.

New A-configuration data, presented here for the first time, were gathered during 13 nights in 2008 December, 90 hr in total. Each track was 7 hr long, to maximise elevation and thus minimise ground pick-up, which would cause an increase in system temperatures and, in turn, an increase in the noise of the image. The old VLA correlator was used, in its spectral-line mode ('4') with two intermediate frequencies (IFs) at frequencies of 1.365 and 1.435 GHz, each with seven 3.125-MHz channels recording both right and left circular polarisations every 3 s; short integration times are used to avoid time-average smearing effects. Multiple, narrow channels are used to reduce the effect of bandwidth smearing, which would otherwise dramatically limit the useful field of view of each pointing and make it impossible to deal with (i.e. clean) bright sources in the outer regions of the primary beam.

Over the years, 0241−082, 0217+017 using 0157−107 were chosen to calibrate the complex gain and the bandpass. None of these is an ideal calibrator, but all are adequate when employing suitable $uv$ restrictions. Absolute flux density calibration was achieved via 0137+331 (3C 48) and 0542+498 (3C 147), which were usually observed at the beginning and the end of each run, respectively.

## 2.3 Data reduction and imaging

Reduction of the data was accomplished using the $\mathcal{AIPS}$ (Astronomical Image Processing System) package. Prior to calibration, the data were carefully flagged to remove any data corrupted by RFI or antenna tracking faults, using the standard flagging tasks, TVFLG and UVFLG. Data were flagged very carefully, looking

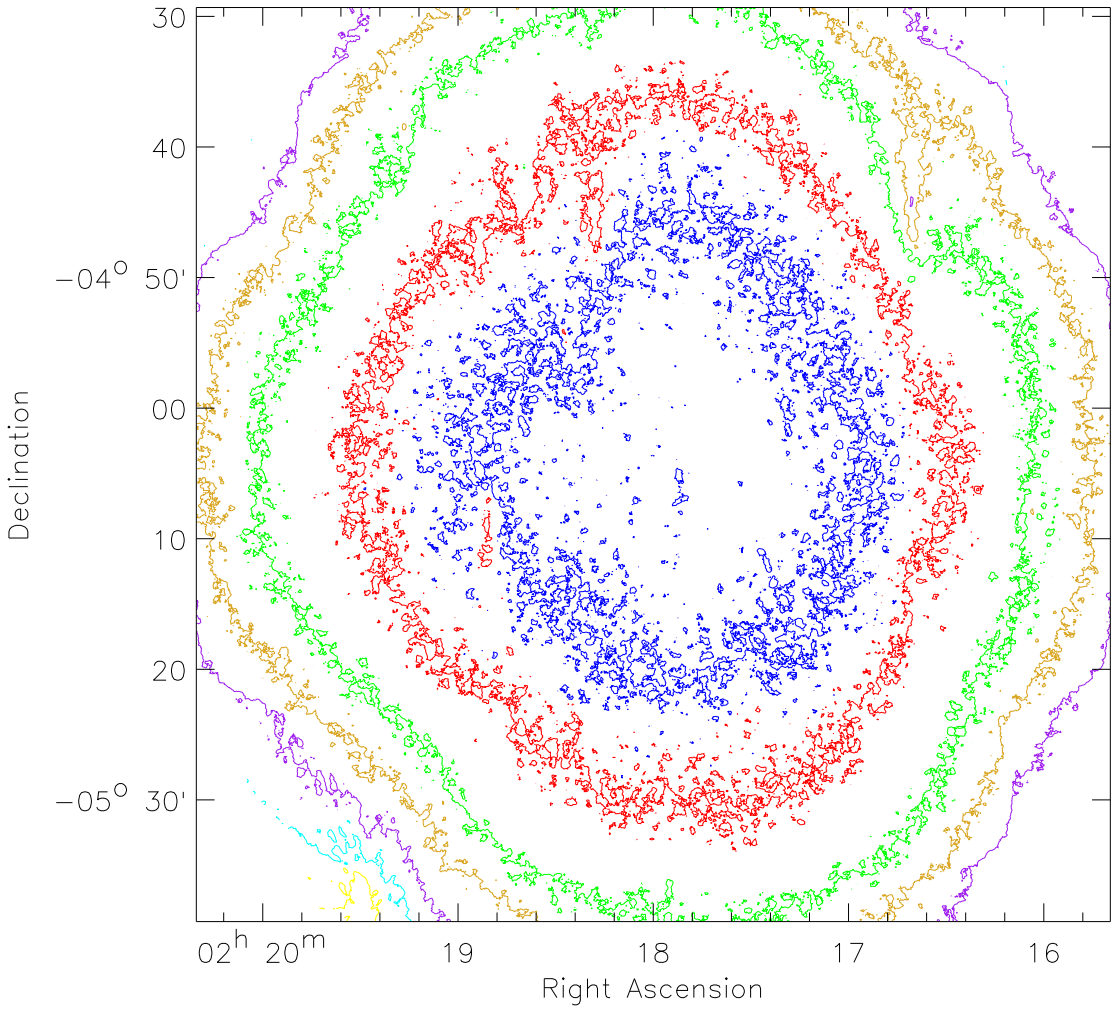


Figure 2.1: Noise contour map of the multi-configuration mosaic, centred at R.A. $2^{\rm h}18^{\rm m}00^{\rm s}.0$ and Dec. $-05^{\rm d}04'20''$ J2000. Contours are plotted at 8 (blue), 10 (red), 15 (green), 20 (gold), 30 (purple), 50 (cyan) and 100 (yellow)$\times\mu$Jy beam$^{-1}$. The central 0.6 deg$^2$, which coincides with deep optical and near-IR observations of the UDS field, has an r.m.s. noise level less than 10 $\mu$Jy beam$^{-1}$.

Table 2.1: UDS pointing positions and noise levels reached at its centres

| Pointing number | Name | R.A. (h m s) | Dec. (d m s) | r.m.s. ($\mu$Jy beam$^{-1}$) |
|---|---|---|---|---|
| 1 | SXDSM3P5 | 02 18 00 | −04 51 20 | 10.9 |
| 2 | SXDSO3P5 | 02 18 30 | −05 04 20 | 11.0 |
| 3 | SXDSO2P5 | 02 17 30 | −05 04 20 | 10.0 |
| 4 | SXDSM4P5 | 02 19 00 | −04 51 20 | 14.1 |
| 5 | SXDSM2P5 | 02 17 00 | −04 51 20 | 13.2 |
| 6 | SXDSM3P4 | 02 18 00 | −05 17 20 | 12.3 |
| 7 | SXDSO1P5 | 02 16 30 | −05 04 20 | 14.9 |
| 8 | SXDSO2P4 | 02 17 30 | −05 30 20 | 13.3 |
| 9 | SXDSO2P6 | 02 17 30 | −04 38 20 | 14.4 |
| 10 | SDXSO3P6 | 02 18 30 | −04 38 20 | 13.9 |
| 11 | SXDSO4P5 | 02 19 30 | −05 04 20 | 14.9 |
| 12 | SXDSO3P4 | 02 18 30 | −05 30 20 | 17.4 |
| 13 | SXDSM4P4 | 02 19 00 | −05 17 20 | 13.8 |
| 14 | SXDSM2P4 | 02 17 00 | −05 17 20 | 13.1 |

at each individual channel, IF and polarisation. Amplitude and phase calibration were then carried out with the CALIB task using the nearby calibrators. Time-dependent bandpass calibration was accomplished via the same calibrators, to account for variability of the complex gain response with both frequency and time. Higher RFI levels were identified in the 2001, 2002 and 2003 data. This can be attributed mainly to ionospheric disruption of the radio signals, since many of these observations were undertaken during daytime, close to the 2001 solar maximum. However, Ivison et al. (2007) reported a correlator failure which contributed to the severe interference found in some of the 2003 A-configuration data.

The data for each individual pointing and configuration were concatenated across the different observing runs.

The next stage was to self-calibrate the data, which is an iterative process involving further tweaks to the amplitude and/or phase solutions based on ever-improving maps. To accomplish this, we first used heavily tapered $(u, v)$ data to create wide-field (2.5-deg$^2$) images of each pointing, in order to identify any distant, bright sources whose sidelobes might spill into the primary beam ($\sim$30 arcmin FWHM at 1.4 GHz for the VLA). This is an important consideration at 1.4 GHz as the primary beam has a high first-sidelobe response (Owen et al., 2005). Having identified these bright sources, an area of diameter 40 arcmin was divided into 55 facets – each facet consisting of $1024^2$

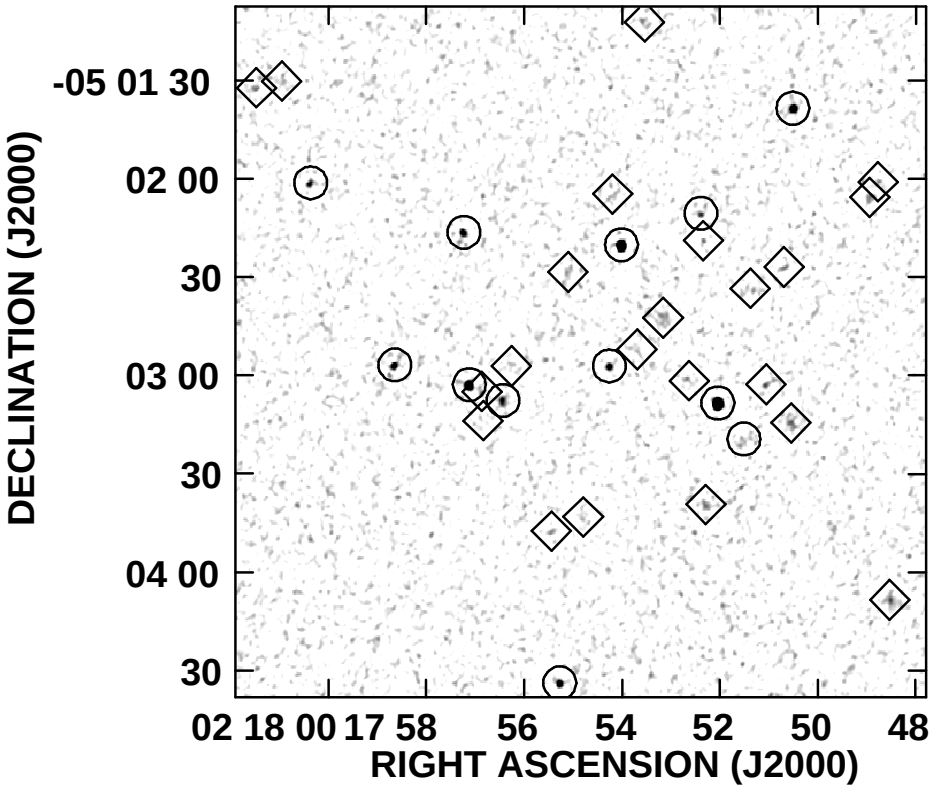


Figure 2.2: A $\approx$10-arcmin$^2$ region of the UDS radio mosaic. Sources marked with a diamond are those found in the 4$\sigma$ catalogue; those marked with a circle are also present in the 6-$\sigma$ catalogue (see §3.4).

pixels, each pixel $0.35'' \times 0.35''$ – to cover the primary beam (centred on each of the 14 pointings, so 770 facets in total, and $\approx 8 \times 10^8$ pixels), with dozens of additional facets placed on bright sources outside each of the primary beam areas. This multi-faceting technique is employed to reduce distortion effects of the wide, non-planar field. A clean box or circle was then placed around the sources in each facet to ensure only real sources are used during self-calibration, allowing for better cleaning of the image and avoiding the worst effects of the so-called 'CLEAN bias'.

Self-calibration was accomplished with CALIB on a pointing-by-pointing and configuration-by-configuration basis, first in phase only, then in both phase and amplitude. After each pass, IMAGR was run on a concatenated file of the calibrated data in the A, B and DnC configurations to provide an optimal image for subsequent self-calibration. The CLEAN boxes were re-defined after each iteration, resulting in significant improvements to the final images. CLEAN components (delta functions representing most of the real flux density in the maps, centred on the appropriate pixels) were subtracted from the $uv$ data using UVSUB (FACTOR = 1) and the data were flagged once more by eye to remove any residual corrupt data, which are now more easily spotted; the CLEAN components were then added back (UVSUB, FACTOR=$-1$).

Since the same positions on the sky were observed many times in the different configurations, the CPU-intensive job of imaging was made easier by averaging the data (optimally, based on baseline length) using STUFFR. The concatenated multi-configuration data were then re-imaged with IMAGR. PEELR was then used to deal with residual sidelobe structures around the brightest sources in five pointings, SXDSM3P5, SXDSO3P5, SXDS02P5, SXDSM4P5 and SXDSM4P4, by self-calibrating the data using only those sources (Owen et al., 2009).

Before a final image of the UDS could be created, all the facets in each of the pointings were convolved to a common beam size. Unfortunately, the choice of this common beam size is driven by the lowest common denominator – the lowest spatial resolution achieved in any facet across the 14 pointings – but this cannot be helped, and still provides a $\approx 3\times$ improvement in spatial resolution over the previously available imaging. The final synthesised beam size was $1.82'' \times 1.63''$, with a position angle of $177°$.

The facets were then knitted or mosaic-ed together with the task FLATN, weighted by the noise within each pointing, determined using RMSD with OPCODE = 'MEAN'

and a circular window of diameter 101 pixels. This mosaicing technique was repeated a number of times with the goal of finding the sweet spot where losses due to bandwidth smearing are compensated by the inclusion of additional areal coverage in the mosaicing process. This was assessed by maximising the number of reliable detections in the map, as assessed by crude 5-$\sigma$ source extraction with the SAD algorithm (source extraction will be discussed in detail in Section 2.4). This was done by cropping each pointing at 10, 30 and 50 per cent using the PBPARM parameter in FLATN[3]. It was found that cropping each individual pointing to exclude the area beyond the 30-per-cent beam sensitivity level, i.e. beyond a radius of 19.86 arcmin, gave the best compromise, yielding $\sim$1000 more sources than the 50-per-cent beam cut-off and suffering considerably less from bandwidth smearing effects than the 10-per-cent beam cut-off.

The final image covers an area of $\sim$1.3 deg$^2$. The noise level is $< 8\,\mu$Jy beam$^{-1}$ at the centre of the map and $\sim 10\,\mu$Jy beam$^{-1}$ within the central 0.6 deg$^2$, i.e. the area covered by deep optical and near-IR observations of the UDS field (Cirasuolo et al., 2010). Fig. 2.1 shows a noise map, created using RMSD, with contour levels at 8 (blue), 10 (red), 15 (green), 20 (gold), 30 (purple), 50 (cyan) and 100 (yellow) $\mu$Jy beam$^{-1}$. Fig. 2.2 displays a small, representative portion of the intensity map.

### 2.3.1 Bandwidth smearing effects

Bandwidth smearing (BWS) causes a reduction in the peak flux density of a source, as well as an elongation towards the pointing centre. It is important to consider BWS when planning and analysing A-configuration VLA observations.

As we saw in Chapter 1, the reduction in peak flux density, assuming a Gaussian bandpass and circular Gaussian tapering, can be estimated using

$$\frac{I}{I_0} = \frac{1}{\sqrt{1+\beta^2}} \quad \text{where} \quad \beta = \frac{\Delta\nu}{\nu}\frac{\theta}{\theta_{\rm beam}}. \tag{2.1}$$

where $I$ and $I_0$ are the observed and intrinsic peak flux densities, $\Delta\nu$ is the bandwidth of each channel (3.125 MHz in this case), $\nu$ is the central observing frequency, $\theta$ is the distance of the source from the phase centre and $\theta_{\rm beam}$ is the synthesised beam size (Taylor, Carilli & Perley 1999). This is often used to correct for the reduction

[3]Note that the beam sensitivity decreases with increasing distance from the centre of the map and so an image cropped at 50-per-cent beam sensitivity is considerably smaller than an image cropped at 10-per-cent sensitivity.

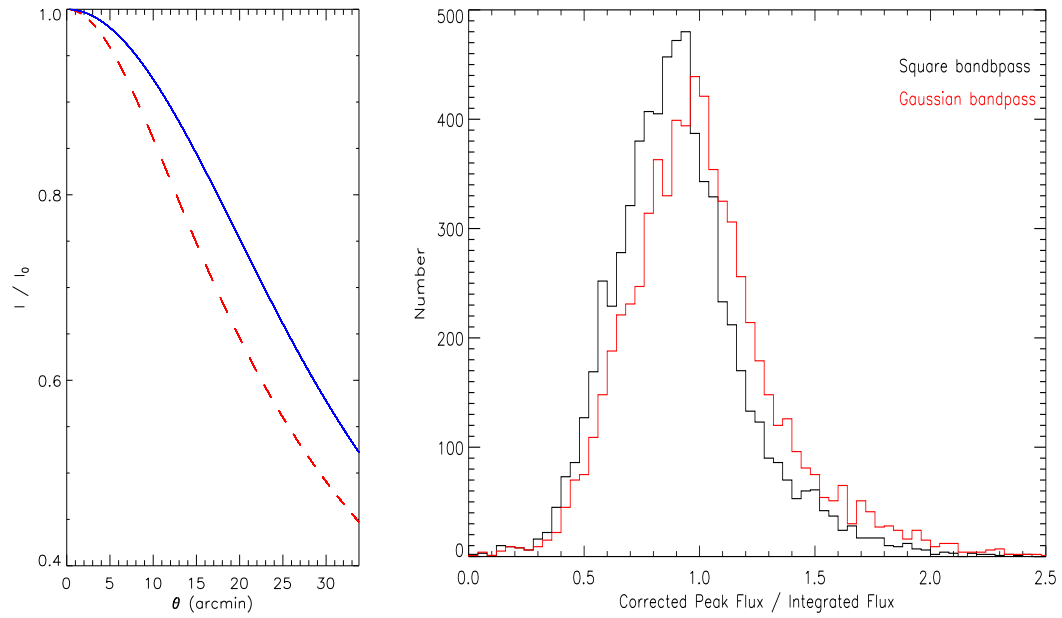


(a) (b)

Figure 2.3: *Left:* The reduction in peak intensity as a function of distance from the phase centre, $\theta$, for a Gaussian (red dashed line) and square (blue solid line) bandpass. This was calculated using Equation 2.1 with $\Delta\nu = 3.125\,\mathrm{MHz}$, $\nu = 1.4\,\mathrm{GHz}$ and $\theta_{\mathrm{beam}} = 1.82''$. *Right:* Comparison of the corrected peak flux to integrated flux density ratio using the two different smearing corrections. The correction appropriate for a square bandpass results in fewer peak fluxes being boosted to values higher than the integrated fluxes.

in peak flux densities, but we found that peak flux densities were then often boosted to values higher than the integrated flux density (which is conserved in the presence of BWS). After much exploratory work, an alternative correction – appropriate for a square bandpass with circular Gaussian tapering – was used:

$$\frac{I}{I_0} = \frac{\sqrt{\pi}}{\gamma\beta}\,\mathrm{erf}\,\frac{\gamma\beta}{2} \quad \text{where} \quad \gamma = 2\sqrt{\ln 2} \tag{2.2}$$

and erf is the error function. The difference between the two different approaches is illustrated in Fig. 2.3(a). As can be seen in Fig. 2.3, the correction for a square bandpass results in fewer peak fluxes being boosted to values higher than the integrated flux densities. The reduction in peak flux density, $I/I_0$, for the final map is roughly a weighted average of the value at the corresponding pixel in each of the contributing pointings. Following a similar procedure to that used to create the final intensity map, the BWS was estimated as a function of position. Using Equation 2.2, a smearing map was generated, weighted by the noise values in the individual facets. This BWS map was then used to obtain the value of $I/I_0$ at the position of each source and is provided in the catalogue.

In practise, it is virtually impossible to correct the angular sizes of each source for the effect of BWS because each point in the final mosaic has contributions from as many as seven different pointings, each influencing a hypothetical source at that position in its own way (magnitude of effect; relative weighting; position angle). For this reason, the convolved (from the synthesised beam) source sizes are included in the catalogue and no correction is made to the sizes for BWS.

## 2.4 Source extraction and cataloguing

### 2.4.1 Source extraction

Source extraction was accomplished using the $\mathcal{AIPS}$ task, SAD, searching for sources down to a signal-to-noise (SNR) threshold of $4\,\sigma$, where the signal in this case is the peak flux density and $\sigma$ is determined locally using RMSD (OPCODE = 'RMS'; circular window of 101 pixels) on residual maps from a similarly deep source extraction. Catalogued sources were also constrained to have an integrated flux density $\geq 2.5\sigma$.

The use of a reliable noise map avoids the detection of spurious sources at the

edges of the map where the noise is highest (Fig. 2.1). Error estimation in SAD follows the formulae given by Condon (1997). There is a tendency for this source extraction method to miss extended sources with low surface brightness. Compact sources affected by BWS may also be missed in this way. The signal map was therefore convolved by factors of $\sqrt{2}$ and 2 to produce maps with beam sizes of $2.57'' \times 2.31''$ and $3.64'' \times 3.26''$, respectively. Source extraction was then repeated for these lower resolution maps and the catalogues were merged.

The map was examined visually to identify the most extended sources – 57 of them – and new positions and flux density values were then obtained individually using TVSTAT. In the final catalogue, these sources are marked with a '1' in the 'FLAG_TVSTAT' column. Where possible, the positions of extended sources identified as jets or lobes were chosen by identifying the host in 3.6- and/or 24-$\mu$m *Spitzer* images, following Simpson et al. (2006). For those sources whose flux densities were measured using TVSTAT, an additional flag (the 'FLAG_TVSTAT_TYPE' column of the catalogue) indicates the type of extended source it was determined to be:

(a) ES – extended source;

(b) ME – multi-element source, e.g. core and jets;

(c) AF – source with imaging artifacts.

The 'FLAG_CATNO' column identifies which of the three maps a source was extracted from, where catalogue 1 is the highest resolution map and 3 is the lowest. So, "123" means the source was identified in all three catalogues; "120" means the source was found only in catalogues 1 and 2; "003" indicates a detection in catalogue 3 only. After refining the catalogue for multiple detections of single sources, the full 4-$\sigma$ catalogue contains 6,861 sources. Many of these will be spurious, but this catalogue will be useful in the next steps.

### 2.4.2 A robust final catalogue

In-depth studies of the $\mu$Jy radio population require robust catalogues of faint radio emitters. To choose an appropriate threshold for our catalogue, we employ a novel technique using the deep near-IR photometric catalogue published by Warren et al. (2007), which covers 0.89 deg$^2$ of our radio image.

First, a very deep (4-$\sigma$) catalogue was searched for near-IR counterparts (hereafter IDs) with a matching radius of up to 3 arcsec. Only the closest matches were accepted. Fig. 2.4(a) shows the distribution of counterpart separations. The solid line shows the contamination level (i.e. by random line-of-sight near-IR emitters) expected for each bin of separations, as estimated from the average source density down to the detection threshold of the photometric catalogue. Within a separation of 1 arcsec, 66 per cent of the 4-$\sigma$ radio sources have a near-IR id. This rises to 86 per cent at a separation of 2 arcsec, but spurious associations are now expected to dominate. Even when losing a third of the catalogue, there are sufficient sources to explore completeness, so a separation of 1 arcsec was adopted for this purpose.

Fig. 2.4(b) shows the fraction of radio sources with near-IR IDs within 1 arcsec as a function of peak-to-noise (PNR). Even at 5$\sigma$, it can be seen that a significant number of sources must be spurious. By the time a threshold of 6$\sigma$ was reached, the curve has reached a plateau at around 97 per cent (the remaining 3 per cent are a combination of compact, near-IR-faint radio galaxies and radio lobes), and contains 1,082 sources with near-IR IDs. Dropping our threshold to 5.5$\sigma$ would add 181 sources, but $\sim$50 of them were regarded as dubious, so this is not a price worth paying for a larger sample. A 6-$\sigma$ threshold was hence chosen for the robust catalogue. A small selection from the catalogue is shown in Table 2.4.

## 2.5 Source counts

The catalogue described in Section 3.4 was now used to determine the differential source counts (per unit area), normalised to a Euclidean Universe. It is important to note, that the observed counts will be affected by completeness. Several effects can cause incompleteness, such as

(a) the increase in noise towards the edges of the map that results from primary beam attenuation;

(b) the reduction in peak flux density due to BWS effects;

(c) the loss of low-surface-brightness objects with flux densities close to the detection threshold.

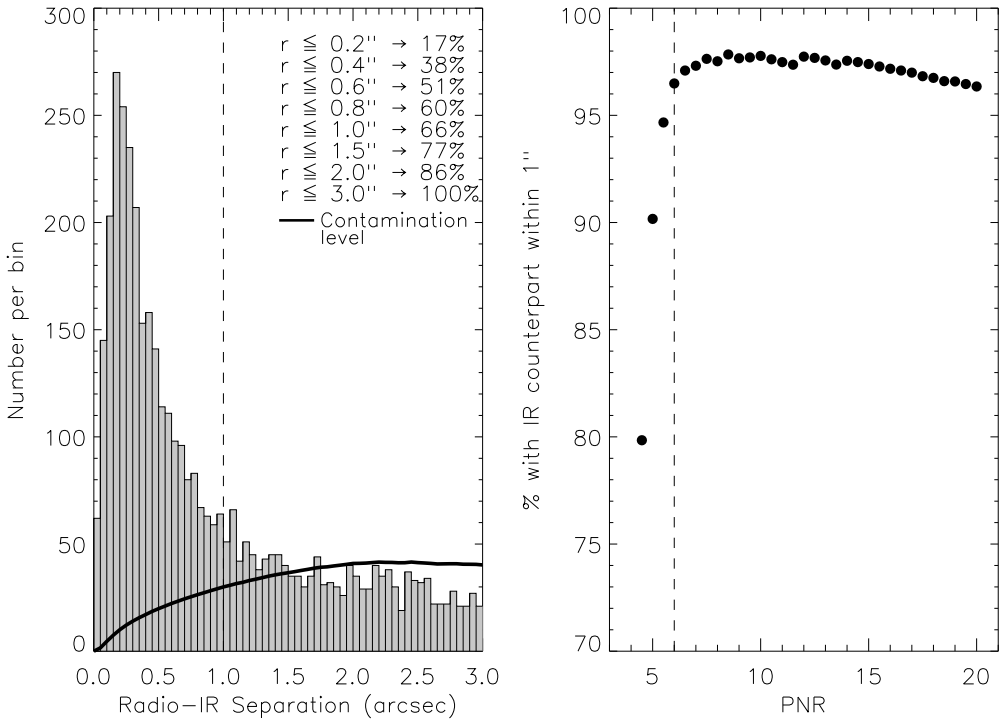


(a) (b)

Figure 2.4: *Left:* Number of matches within a given radial separation. The solid line represents the level of contamination expected for each bin, as estimated from the average source density down to the detection threshold of the photometric catalogue. The inset values represent the fraction of sources with IDs within a given separation. Our adopted search radius of 1 arcsec is marked with a dashed line. *Right:* Fraction of radio sources with near-IR IDs within 1 arcsec. The dashed line represents the chosen threshold, at $6\sigma$, for the final catalogue.

Table 2.2: Parameters used to simulate completeness (for the counts presented in Table 2.3).

| Parameter | Description |
|---|---|
| R.A., Dec. | Sky position of source |
| n | Number of pointings contributing to source |
| $S_\nu$ | Integrated flux density |
| BMAJ | Intrinsic major axis |
| BMIN | Intrinsic minor axis |
| $\mathrm{BMAJ_{syn}}$ | Major axis of the synthesised beam |
| $\mathrm{BMIN_{syn}}$ | Minor axis of the synthesised beam |
| $\mathrm{BMAJ_{conv}}$ | Convolved major axis of source |
| $\mathrm{BMIN_{conv}}$ | Convolved minor axis of source |
| Peak | Peak flux density |
| $\mathrm{BMAJ_{sm}}$ | Smeared major axis of source |
| $\mathrm{BMIN_{sm}}$ | Smeared minor axis of source |

Correction factors can be determined via the use of simulated skies, containing radio sources with characteristics similar to those expected in the image. Table 2.2 summarises the parameters used to describe the sources used in the simulations.

The simulated sources were generated with flux densities distributed randomly between 0.01 and 10 mJy, and with a flux-density-dependent angular size distribution. The two angular size distributions used were those of Windhorst et al. (1990) and Bondi et al. (2003). The former is given by

$$h(\theta) = \exp\left(-\ln(2) \times \frac{\theta}{\theta_{\mathrm{med}}^{0.62}}\right) \tag{2.3}$$

where $\theta$ is the FWHM of the source and $\theta_{\mathrm{med}} = 2.0\, S^{0.3}$ arcsec. The Bondi et al. (2003) distribution is given by

$$h(\theta) = \begin{cases} (1.6^{\theta})^{-1} & \text{for } \theta \leq 4\,\text{arcsec} \\ \theta^{-1.3} - 0.01 & \text{for } \theta > 4\,\text{arcsec.} \end{cases} \tag{2.4}$$

At $S_\nu > 3$ mJy, the Windhorst et al. (1990) distribution is assumed; between 0.8 and 3 mJy the average of the Windhorst et al. (1990) and Bondi et al. (2003) distributions is taken. For the faintest sources, $S_\nu < 0.8$ mJy, only the Bondi et al. (2003) distribution is considered. These angular sizes were adopted as the intrinsic

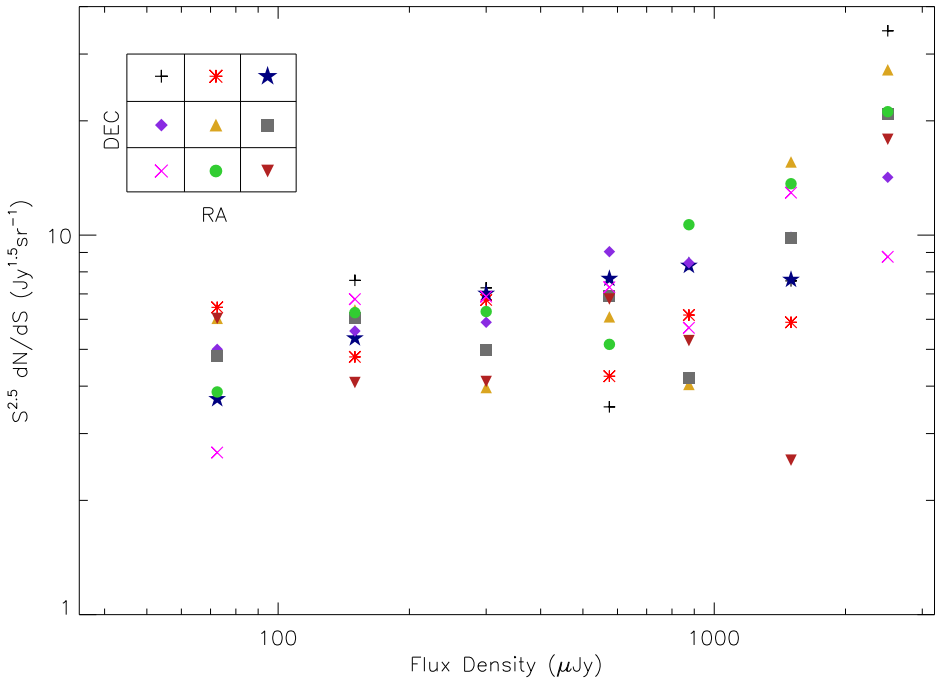


Figure 2.5: Euclidean normalised differential source counts at 1.4 GHz, up to 3 mJy, for nine sub-divisions of the radio map. The inset grid displays the way in which the map (as in Fig. 2.1) was divided and the corresponding plot symbols for each division.

major axis of the source, BMAJ. These fake sources were then convolved with the synthesised beam to simulate the interferometric response, yielding $\mathrm{BMAJ_{conv}}$. Given that the area and the integrated flux density are known, the intrinsic peak flux density can be obtained using

$$\mathrm{Peak} = S_\nu \, (1.1331 \ \mathrm{BMAJ_{conv}} \ \mathrm{BMIN_{conv}})^{-1}. \tag{2.5}$$

These sources were then assigned coordinates corresponding to those on our final image, avoiding noisy regions around bright sources. Each source could then be referenced to positions on the 14 individual pointings that were used to mosaic the final map. The individual pointings contributing to the measurement of each source were identified and the distance between the source and the individual phase centres (PCs) determined, and the position angle. This information is important: the position of each source in the individual pointings determines the appropriate degree of BWS and primary beam attenuation.

Table 2.3: Radio source counts at 1.4 GHz.

| Flux bin ($\mu$Jy) | $S_{\rm m}$ ($\mu$Jy) | $N$ | $N_{\rm C}$ | $S^{2.5}\,dN/dS$ (sr$^{-1}$ Jy$^{1.5}$) | $C$ |
|---|---|---|---|---|---|
| 45–100 | 72.5 | 422 | 2399.8 | $4.88 \pm 1.25$ | 5.69 |
| 100–200 | 150 | 439 | 790.0 | $6.07 \pm 1.06$ | 1.80 |
| 200–400 | 300 | 220 | 281.1 | $6.29 \pm 1.26$ | 1.28 |
| 400–750 | 575 | 96 | 105.7 | $6.79 \pm 1.74$ | 1.10 |
| 750–1,000 | 875 | 26 | 28.3 | $6.16 \pm 2.25$ | 1.09 |
| 1,000–2,000 | 1,500 | 40 | 42.5 | $9.83 \pm 4.11$ | 1.06 |
| 2,000–3,000 | 2,500 | 19 | 19.7 | $17.9 \pm 11.7$ | 1.04 |
| 3,000–6,000 | 4,500 | 18 | 18.5 | $19.8 \pm 12.7$ | 1.03 |
| 6,000–10,000 | 8,000 | 8 | 8.1 | $31.2 \pm 24.7$ | 1.01 |

The next step was to introduce the effects of BWS and primary beam attenuation into the simulated sky. For the former, the flux density of each smeared source was conserved, so $\mathrm{BMAJ_{conv}}$ and $\mathrm{BMIN_{conv}}$ were altered appropriately.

For each fake source, the average contribution from the different pointings was injected into a residual image, chosen to be the best approximation for the noise structure in the observations. Finally, source detection was done in exactly the same way as described in Section 2.4. The simulations were repeated ten times, using $\sim 2{,}500$ sources each time, to get a robust estimate of the completeness as a function of flux density.

Due to non-uniform noise structure across the map (Fig. 2.1), different areas of the map require different completeness corrections for a given flux bin. This was taken into consideration by dividing the map into nine sub-regions, then calculating the differential counts for these sub-divisions, as shown in Fig. 2.5. The final differential source counts per flux bin was taken to be the median of the nine values and the uncertainties are determined from the scatter of the counts amongst these nine sub-divisions. The uncertainties, which are considerable, then reflect the Poisson errors and the scatter of the counts across the map.

The differential source counts so determined, $S^{2.5}dN/dS$, are given in Table 2.3 along with the observed number of sources ($N$), corrected number counts ($N_{\rm C}$) and the respective corrective factor, $C$. The $S_{\rm m}$ column in Table 2.3 is the middle of the bin – the flux density used to calculate the differential source counts. The source counts up to 3 mJy are shown in Fig. 2.6 along with those from a number of other radio surveys,

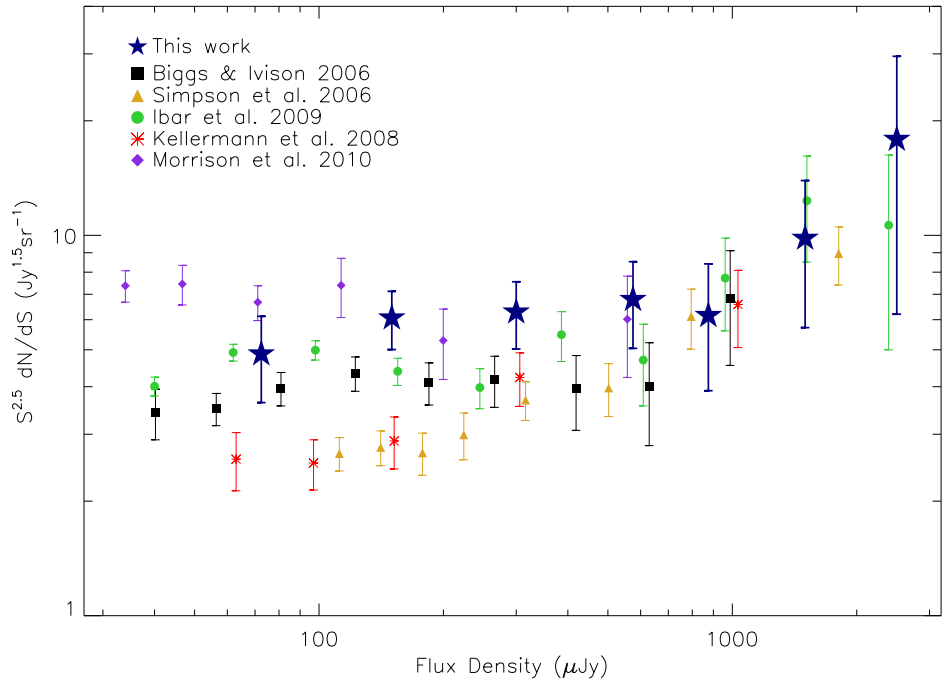


Figure 2.6: Euclidean normalised differential source counts at 1.4 GHz from this work and some previous surveys: HDF-N (Biggs & Ivison, 2006; Morrison et al., 2010) UDS (Simpson et al., 2006); Lockman Hole (Ibar et al., 2009); CDF-S (Kellermann et al., 2008).

for comparison. The differential source counts per unit area in the range 45–1,000 $\mu$Jy can be represented by a power-law fit,

$$\frac{dN}{dS} = (12.7 \pm 9.4)\, S_{\nu}^{-2.41\pm0.09}\ \mathrm{Jy}^{-1}\mathrm{sr}^{-1}, \tag{2.6}$$

close to the Euclidean value of $-2.5$. The counts must eventually drop steeply at some lower flux density, otherwise the sky brightness will exceed the observed cosmic radio background (e.g. Singal et al., 2010). The steepening in the counts seen above 1 mJy suggests that they represent a different population of objects to those dominating the sub-mJy counts, as discussed by many authors.

Above $\sim$300 $\mu$Jy, there is a reasonable degree of consistency between the counts determined in the different deep fields. The field-to-field scatter increases at the faintest flux densities and a number of factors could be contributing to this, e.g. inconsistencies between datasets and the use of different data reduction methods. Within the map, the scatter seen across the nine sub-divisions (Fig. 2.5) suggests that the effect of cosmic variance across the UDS field may be stronger than that found by Condon (2007) in the *Spitzer* First Look Survey (FLS) region. At $z \sim 1$, the angular extent subtended by this map corresponds to a comoving transverse size of $\sim$ 70 Mpc and so would expect to see differences in source density due to large-scale structure. However, uncertainties could also arise due to imperfect modelling of the fake sources used to account for incompleteness, particularly from the choice of angular size distributions, and particularly at the faint end of the accessible flux density distribution.

## 2.6 Confusion

At the resolution of this map, extrapolating the counts to fainter fluxes suggest that the confusion limit will be reached at a detection threshold of $\sim$ 3 $\mu$Jy, though this is of course influenced by the intrinsic size of the radio emitters. For a source size of 0.65 arcsec – the median size of radio-emitting regions in distant starbursts as determined by Biggs & Ivison (2008), the natural confusion limit is estimated to be at $\sim$ 1 $\mu$Jy, although Condon (2007) suggest that the natural confusion limit could be as low as $\sim$15 nJy. Based on the counts, the 10-arcsec angular resolution of the ASKAP-EMU survey (Norris et al., 2011) will yield an confusion limit of $\sim$ 54 $\mu$Jy. A similar calculation for the MIGHTEE-MeerKAT survey (Jarvis, 2012) at an angular resolution of 3.5 arcsec will reach its confusion limit at $\sim$ 12 $\mu$Jy. This uncertainty

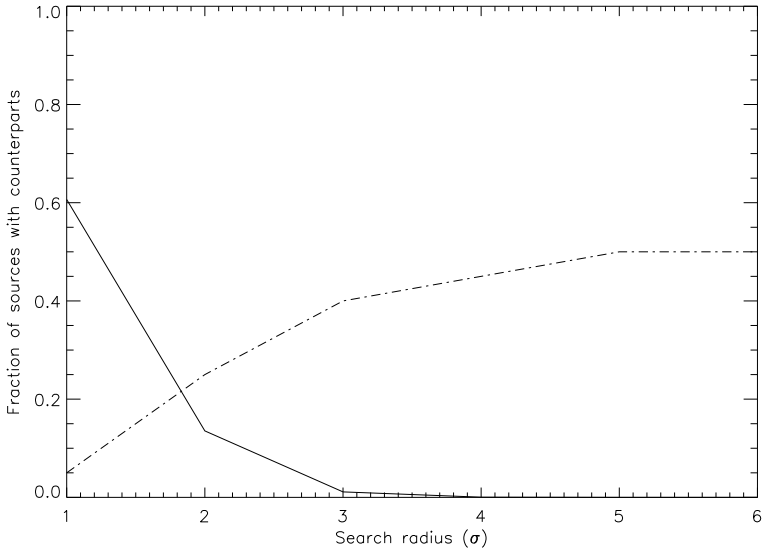


Figure 2.7: The dot-dashed line represents the fraction of sources with robust counterparts ($p \leq 0.05$) at varying search radii, in multiples of the positional uncertainty of the submm source, $\sigma$. The solid line represents the number of sources for which a radio counterpart will not be found, calculated using the cumulative distribution function of the Rayleigh distribution.

in the natural confusion limit needs to better constrained, since there may be design consequences for facilities such as the Square Kilometer Array (SKA), and this should be within the capabilities of upcoming surveys with the upgraded Jansky VLA and e-MERLIN interferometers.

## 2.7 Identifying radio counterparts to submm galaxies

As discussed in Section 2.1, due to the limited number of submm interferometers (and suitable weather) available for obtaining sub-arcsec astrometry, radio observations have often been used as a high-resolution proxy for submm measurements. Radio identification of submm sources is possible due to the correlation between far-IR and radio flux densities, discussed earlier; emission at both wavelengths traces recent star-formation activity.

Due to the large beam sizes of single-dish submm observatories, determining radio counterparts to submm sources is non-trivial: multiple radio sources may be present close to the position of the submm source. Better methods are beginning to emerge,

but a robust and reasonable way of identifying radio counterparts to submm sources within a given search radius, $r_{\rm s}$, is to use the corrected Poisson probability (the *P* statistic – Downes et al., 1986). Within a given search radius, the *P* statistic uses the surface density of objects brighter than some flux density (or magnitude) to calculate the probability of a chance association. For a surface density, *N*, of objects with flux densities greater than *S*, the expected number of events within a given counterpart separation, *r*, is:

$$\mu = \pi r^2 \, N. \tag{2.7}$$

The probability of finding at least one object within *r*, with a flux density of *S* or greater is then

$$p = 1 - \exp(-\mu). \tag{2.8}$$

As the search is done within a larger search radius, the expected number of events has to be corrected for a critical probability, $p_{\rm crit}$ – the probability of finding a source at $r_{\rm s}$ and at the flux density limit, $S_{\rm lim}$. The corrected expected number of events is then

$$\mu_{\rm corr} = p_* \, [1 + \ln(\frac{p_{\rm crit}}{p_*})] \quad \text{where} \quad p_{\rm crit} = \pi r_{\rm s}^2 \, N_{\rm lim}. \tag{2.9}$$

and $p_*$ is the probability of a chance association for each source found within $r_{\rm s}$. Substituting $\mu_{\rm corr}$ into Equation 2.8 will then give the corrected probability that each radio source is associated with the submm source by chance. The source least likely to be a chance association is taken to be the counterpart. Typically, sources with $p \leq 0.05$ are taken to be a counterpart (Ivison et al., 2007; Biggs et al., 2011; Michalowski et al., 2012).

The radius within which we search for counterparts has to be large enough that candidate counterparts are not missed; at the same time, the area cannot be too wide, otherwise bright, unrelated sources can be selected as counterparts. An alternative to using a fixed radius is to use a radius that is a function of the SNR ratio of the submm detection, which is linearly related to the positional accuracy. The counterpart-matching work done here was carried out using $r_{\rm s} = 3\sigma$ where $\sigma$ is the positional error of the submm source. As given in Ivison et al. (2007), $\sigma$=0.6 (SNR)$^{-1}$ FWHM is adopted as the positional uncertainty of the submm source. Following Biggs et al. (2011), Fig. 2.7 illustrates the justification for using a 3-$\sigma$ search radius. At 3$\sigma$, the

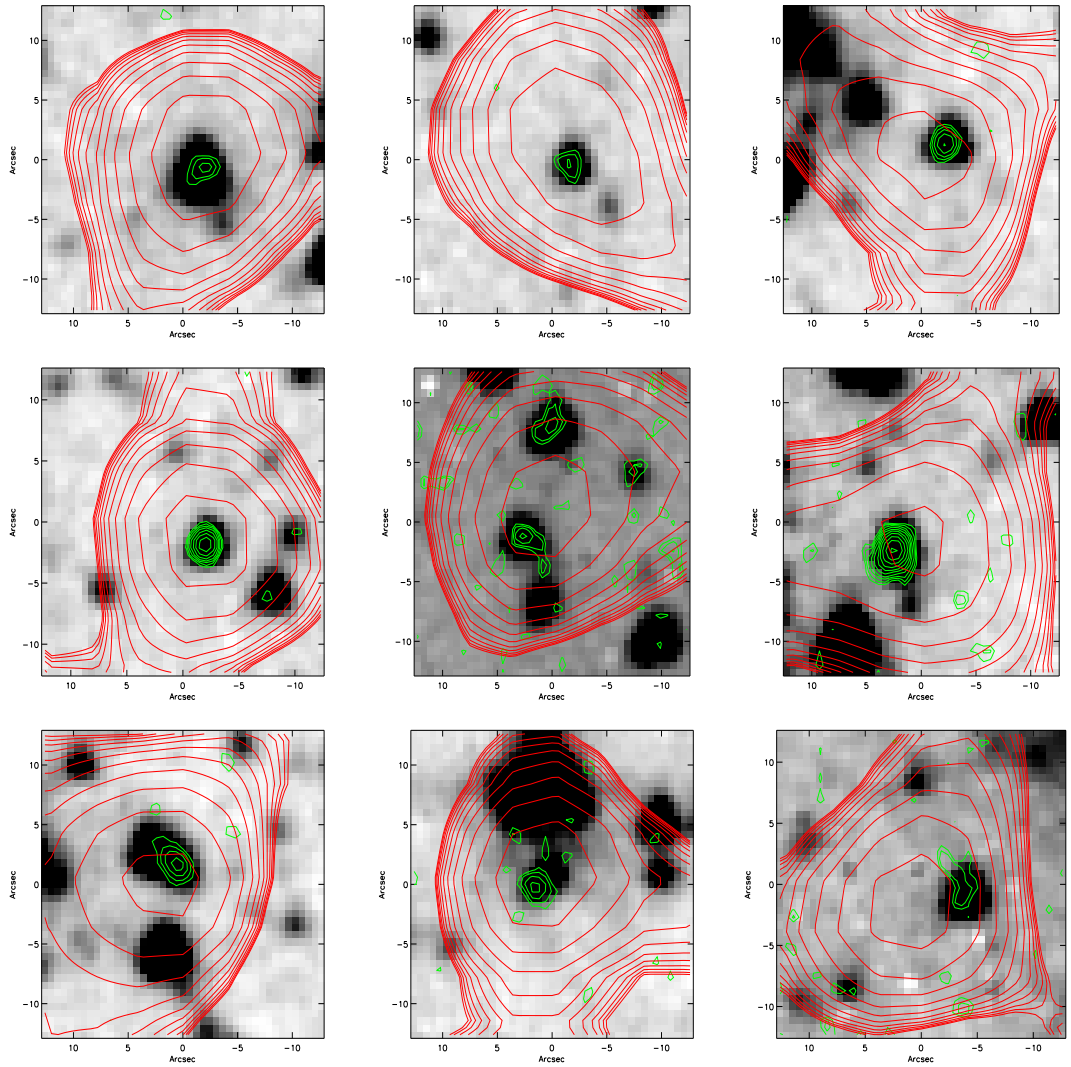


Figure 2.8: Postage stamps, 25 arcsec on a side, at the positions of some of the submm sources for which robust radio counterparts have been identified. The greyscale image is from a *Spitzer* IRAC 3.6-$\mu$m image; superimposed contours represent the radio (green) and submm (red) signal.

fraction of sources for which a counterpart is robustly identified, as shown by the dot-dashed line, ($p \leq 0.05$) is close to the maximum possible fraction. The solid line represents the number of real identifications that are missed, estimated using the cumulative distribution function of a Rayleigh distribution:

$$\mathrm{CDF} = 1 - e^{-\frac{r^2}{2\sigma}}. \tag{2.10}$$

and at $r_\mathrm{s} = 3\sigma$ only $\sim$1 per cent of sources have been missed.

Using *p* statistics, I have assigned radio counterparts from the catalogue presented here to the submm sources detected at 850 $\mu$m in the SCUBA-2 Cosmology Legacy Survey in the UDS ($\mathrm{FWHM} \sim 14$ arcsec; r.m.s. = 2.1 mJy) were identified, taking sources with $p \leq 0.05$ to be robust counterparts. Figure 2.8 displays a small subsample of postage stamps from a large 3.6-$\mu$m *Spitzer* IRAC image at the positions of the submm sources for which radio counterparts have been identified. Most are unambiguous IDs, though the large single-dish submm beam does lead to some blended sources (e.g. the central example in Figure 2.8) and hence some multiple IDs.

## 2.8 Conclusions

The UKIDSS UDS field has been observed with the VLA in its A, B and DnC configurations, producing a high-resolution, deep ($\sigma < 8\mu$Jy beam$^{-1}$ at the centre) radio image and a robust catalogue of more than 1,000 radio emitters. The acquisition and reduction of the data is discussed, as well as a series of sometimes novel steps and simulations undertaken thereafter to assess a safe threshold for the source catalogue and to correct the counts – which agree well with those from previous surveys – for the effects of bandwidth smearing and incompleteness.

In the first of several examples to be encountered in the coming chapters, I exploit these new radio data to find accurate positions for a new catalogue of submm sources from the SCUBA-2 Cosmology Legacy Survey, via the relatively simple $p$ statistic.

Table 2.4: A sample portion of the UDS radio catalogue at 1.4 GHz. Column 14 gives the reduction in peak flux due to BWS effects. Column 15 indicates if a source is detected in the final image and/or the convolved images; the numbering system is explained in Section 2.4.1. A '1' in Column 16 signifies that the flux density of a source was obtained using the TVSTAT task in $\mathcal{AIPS}$. A note is made for these sources – where discernible – in column 17 if the source was an extended, multi-element or an object with imaging artifacts using the abbreviations introduced in Section 2.4.1

| ID | RA | DEC | $S_{TOT}$ | $ERR_{tot}$ | $S_{PK}$ | $ERR_{pk}$ | CONVOLVED SIZES | | | $I/I_o$ | CATNO | TVSTAT | TYPE | NOTES | | | |
|---|---|---|---|---|---|---|---|---|---|---|---|---|---|---|---|---|---|
| | (h:m:s) | (d:m:s) | ($\mu$Jy) | ($\mu$Jy) | ($\mu$Jy/beam) | ($\mu$Jy/beam) | Major (") | Minor (") | PA (deg) | | | | | | | | |
| (1) | (2) | (3) | (4) | (5) | (6) | (7) | (8) | (9) | (10) | (11) | (12) | (13) | (14) | (15) | (16) | (17) | (18) |
| 1 | 02:15:39.79 (0.154) | -05:11:32.1 (0.198) | 299.6 | 65.7 | 133.6 | 22.5 | 2.929 | 2.272 | 5.1 | 2.3 | 1.58 | 7.0 | 0.76 | 9123 | 0 | | |
| 2 | 02:15:39.88 (0.117) | -04:50:14.5 (0.149) | 141.3 | 50.5 | 165.7 | 32.3 | 1.801 | 1.404 | 178.0 | 1.25 | | | 0.67 | 9100 | 0 | | |
| 3 | 02:15:39.91 (0.17 ) | -04:49:16.1 (0.177) | 183.9 | 70.2 | 192.4 | 41.4 | 2.373 | 1.195 | 43.1 | 1.64 | 0.0 | 47.5 | 0.65 | 9100 | 0 | | |
| 4 | 02:15:39.99 (0.165) | -04:52:45.0 (0.109) | 99.6 | 38.2 | 130.7 | 26.6 | 2.026 | 1.117 | 68.6 | 1.81 | | | 0.71 | 9100 | 0 | | |
| 5 | 02:15:40.19 (0.035) | -04:53:42.9 (0.034) | 1302.8 | 66.3 | 776.9 | 27.6 | 2.871 | 1.733 | 133.5 | 2.29 | 0.12 | 129.9 | 0.72 | 9123 | 0 | | |
| 6 | 02:15:40.30 (0.177) | -04:48:52.6 (0.123) | 202.7 | 66.8 | 200.7 | 38.3 | 2.322 | 1.29 | 114.1 | 1.62 | 0.0 | 110.5 | 0.65 | 9120 | 0 | | |
| 7 | 02:15:40.32 (0.184) | -05:18:44.9 (0.171) | 161.5 | 61.3 | 147.0 | 33.3 | 2.113 | 1.543 | 51.8 | 2.01 | | | 0.64 | 9123 | 0 | | |
| 8 | 02:15:40.34 (0.176) | -05:11:24.7 (0.235) | 129.3 | 47.6 | 105.1 | 24.1 | 2.731 | 1.336 | 31.4 | 2.09 | 0.0 | 34.6 | 0.76 | 9123 | 0 | | |
| 9 | 02:15:41.55 (0.216) | -04:53:31.1 (0.232) | 165.1 | 58.7 | 101.2 | 24.9 | 2.384 | 2.029 | 31.4 | 2.38 | | | 0.69 | 9120 | 0 | | |
| 10 | 02:15:41.56 (0.194) | -04:58:49.3 (0.146) | 105.6 | 40.5 | 103.9 | 23.1 | 2.149 | 1.404 | 66.9 | 2.06 | | | 0.79 | 9100 | 0 | | |
| 11 | 02:15:41.77 (0.282) | -04:51:16.2 (0.186) | 236.5 | 67.6 | 124.9 | 26.0 | 3.687 | 1.524 | 118.1 | 3.28 | 0.0 | 116.7 | 0.67 | 9123 | 0 | | |
| 12 | 02:15:42.33 (0.134) | -05:02:48.0 (0.145) | 79.9 | 30.9 | 98.1 | 20.4 | 1.758 | 1.375 | 36.0 | 1.35 | | | 0.81 | 9100 | 0 | | |
| 13 | 02:15:42.42 (0.158) | -05:08:48.2 (0.145) | 106.4 | 37.4 | 104.1 | 21.3 | 1.839 | 1.648 | 108.0 | 1.48 | | | 0.80 | 9120 | 0 | | |
| 14 | 02:15:42.74 (0.186) | -05:06:35.9 (0.145) | 104.2 | 36.9 | 93.21 | 19.7 | 2.071 | 1.602 | 86.7 | 1.91 | | | 0.81 | 9120 | 0 | | |
| 15 | 02:15:43.02 (0.098) | -05:15:39.3 (0.069) | 300.1 | 46.7 | 231.2 | 23.0 | 2.434 | 1.582 | 73.2 | 1.8 | 0.0 | 75.4 | 0.69 | 9123 | 0 | | |
| 16 | 02:15:43.70 (0.226) | -05:00:46.3 (0.133) | 113.1 | 41.4 | 100.9 | 22.2 | 2.464 | 1.349 | 102.4 | 1.84 | 0.0 | 100.4 | 0.81 | 9100 | 0 | | |
| 17 | 02:15:43.90 (0.149) | -05:07:16.2 (0.109) | 162.0 | 40.6 | 133.3 | 20.7 | 2.365 | 1.525 | 69.0 | 1.7 | 0.0 | 71.9 | 0.82 | 9123 | 0 | | |
| 18 | 02:15:43.91 (0.213) | -04:50:47.4 (0.264) | 251.2 | 68.7 | 118.9 | 24.6 | 3.713 | 1.688 | 144.5 | 3.27 | 0.0 | 142.9 | 0.67 | 9123 | 0 | | |
| 19 | 02:15:44.39 (0.105) | -04:57:52.7 (0.119) | 74.4 | 28.0 | 112.3 | 21.0 | 1.526 | 1.289 | 159.7 | 0.73 | | | 0.79 | 9100 | 0 | | |
| 20 | 02:15:44.77 (0.274) | -05:18:42.9 (0.265) | 245.7 | 76.5 | 102.0 | 25.0 | 3.184 | 2.244 | 48.0 | 2.69 | 1.4 | 51.5 | 0.66 | 9123 | 0 | | |
| 21 | 02:15:45.71 (0.115) | -05:06:10.9 (0.148) | 69.6 | 27.3 | 94.2 | 19.1 | 1.754 | 1.25 | 20.3 | 1.24 | | | 0.83 | 9100 | 0 | | |
| 22 | 02:15:45.88 (0.133) | -05:00:36.3 (0.125) | 71.7 | 26.0 | 102.9 | 18.8 | 2.115 | 0.977 | 132.4 | 1.85 | | | 0.82 | 9100 | 0 | | |
| 23 | 02:15:46.05 (0.185) | -04:56:18.5 (0.164) | 87.0 | 34.1 | 83.3 | 19.1 | 2.029 | 1.526 | 58.0 | 1.89 | | | 0.75 | 9120 | 0 | | |
| 24 | 02:15:46.64 (0.198) | -05:18:50.1 (0.204) | 160.6 | 54.9 | 107.0 | 24.7 | 2.166 | 2.056 | 29.7 | 2.03 | | | 0.67 | 9123 | 0 | | |
| 25 | 02:15:47.12 (0.123) | -04:58:06.4 (0.125) | 64.2 | 25.4 | 93.2 | 18.7 | 1.65 | 1.237 | 136.8 | 1.09 | | | 0.78 | 9100 | 0 | | |
| 26 | 02:15:48.30 (0.283) | -04:50:22.1 (0.264) | 205.3 | 67.9 | 100.2 | 24.9 | 3.45 | 1.762 | 131.6 | 2.99 | 0.32 | 129.4 | 0.68 | 9120 | 0 | | |
| 27 | 02:15:48.42 (0.307) | -04:50:19.0 (0.155) | 148.2 | 54.2 | 98.2 | 24.5 | 3.036 | 1.474 | 98.1 | 2.56 | 0.0 | 97.2 | 0.68 | 9100 | 0 | | |
| 28 | 02:15:48.74 (0.213) | -05:00:17.2 (0.16 ) | 90.0 | 34.3 | 87.0 | 19.3 | 2.543 | 1.207 | 122.2 | 1.9 | 0.0 | 118.8 | 0.81 | 9100 | 0 | | |
| 29 | 02:15:48.96 (0.083) | -04:43:15.3 (0.094) | 194.1 | 55.0 | 277.3 | 40.1 | 1.548 | 1.342 | 168.5 | 0.56 | | | 0.63 | 9120 | 0 | | |
| 30 | 02:15:49.18 (0.216) | -05:00:29.2 (0.269) | 123.5 | 44.4 | 76.1 | 18.8 | 2.946 | 1.634 | 147.2 | 2.35 | 0.0 | 144.3 | 0.81 | 9123 | 0 | | |
| 31 | 02:15:49.19 (0.182) | -05:19:20.8 (0.143) | 92.9 | 36.9 | 104.8 | 22.9 | 2.155 | 1.22 | 121.3 | 2.05 | | | 0.67 | 9100 | 0 | | |
| 32 | 02:15:49.52 (0.135) | -05:08:20.5 (0.269) | 151.0 | 46.8 | 97.7 | 20.7 | 3.139 | 1.46 | 11.3 | 2.57 | 0.0 | 12.6 | 0.81 | 9123 | 0 | | |
| 33 | 02:15:49.53 (0.131) | -04:54:22.8 (0.128) | 257.9 | 48.5 | 148.1 | 19.6 | 2.795 | 1.847 | 133.5 | 2.2 | 0.65 | 129.2 | 0.74 | 9123 | 0 | | |
| 34 | 02:15:50.05 (0.232) | -05:07:31.6 (0.178) | 88.8 | 34.6 | 78.1 | 18.4 | 2.646 | 1.275 | 57.4 | 2.05 | 0.0 | 60.2 | 0.85 | 9120 | 0 | | |
| 35 | 02:15:50.27 (0.118) | -05:10:27.5 (0.111) | 210.0 | 40.1 | 136.4 | 17.7 | 2.256 | 2.025 | 65.1 | 1.54 | 0.92 | 73.7 | 0.79 | 9123 | 0 | | |
| 36 | 02:15:50.82 (0.165) | -05:00:39.7 (0.166) | 112.4 | 36.2 | 88.6 | 18.0 | 2.008 | 1.875 | 139.2 | 1.77 | | | 0.82 | 9120 | 0 | | |
| 37 | 02:15:50.88 (0.193) | -04:44:34.5 (0.233) | 202.8 | 70.9 | 136.7 | 32.0 | 2.635 | 1.67 | 147.8 | 1.95 | 0.0 | 143.6 | 0.65 | 9123 | 0 | | |
| 38 | 02:15:51.44 (0.134) | -05:03:59.4 (0.118) | 71.4 | 25.7 | 90.2 | 17.3 | 1.704 | 1.379 | 117.3 | 1.21 | | | 0.87 | 9100 | 0 | | |
| 39 | 02:15:51.55 (0.227) | -05:11:17.3 (0.194) | 106.3 | 35.6 | 76.3 | 16.8 | 2.959 | 1.397 | 52.2 | 2.43 | 0.0 | 54.7 | 0.79 | 9123 | 0 | | |
| 392 | 02:16:37.16 | -05:27:05.7 | 2184.1 | 65.5 | 172.1 | 12.8 | 21.9 | | | | | | 0.82 | 9123 | 1 | ME | Core+lobes |

# Chapter 3

# Multi-wavelength properties of the faint radio population

## 3.1 Introduction

Early radio surveys were limited to detecting the brightest radio-loud galaxies ($L_{1.4\,\mathrm{GHz}} > 10^{25}\,\mathrm{W\,Hz^{-1}}$) and were used as cosmological probes to trace the evolution of AGN across cosmic time (Dunlop & Peacock, 1990). However, the past decade has seen numerous radio surveys with the ability to probe down to fainter flux limits ($\sim 100\mu$Jy) revealing a flattening in the Euclidean radio source counts at fluxes below 1 mJy (Hopkins et al., 2003; Biggs & Ivison, 2006; Simpson et al., 2006; Kellermann et al., 2008; Willner et al., 2012). This flattening indicates an evolution in radio sources and may signify the emergence of a different population in the sub-mJy radio regime.

Despite the plethora of surveys dedicated to understanding the faint, sub-mJy population, the mix of AGN and star-forming galaxies is still a topic of controversy. Initially thought to be dominated by star-forming galaxies (SFGs – e.g. Richards, 2000; Fomalont et al., 2006; Ibar et al., 2009), the sub-mJy population was more recently found to have a significant contribution from radio-quiet AGN (Smolčić et al., 2008; Padovani et al., 2009). Solving this puzzle is key to providing an insight into the interaction between – and possible co-evolution of – AGN and SFGs. Jets and winds produced as a result of accretion of material by the central black holes of galaxies can regulate star-formation activity, either by blowing away the gas that feeds that activity or by triggering star formation. Understanding the relationship between these two different activities is clearly important if we are to understand how galaxies evolve.

When approaching this problem, radio surveys are one of the most powerful tools available to us. Radio emission is unobscured by the dust that is known to be present in the tori of AGN and in star-forming regions. However, the classification of objects into AGN and SFGs is non-trivial and requires the appropriate use of multi-wavelength data.

A number of different approaches can be taken to distinguish sources dominated by nuclear activity from those dominated by fusion-driven activity: imposing a radio luminosity threshold, radio spectral indices, radio morphologies, the far-IR/radio correlation, IRAC colour-colour selection and X-ray counterparts with luminosities above a threshold. As the various diagnostics identify AGN by tracing different physical phenomena, we expect different results from different classification schemes. In this chapter I combine a number of diagnostics to infer the AGN fraction of the radio sample presented in Chapter 2.

The UDS is an ideal field for such a study as it has complementary data covering a wide range of the electro-magnetic spectrum, from X-rays to radio observations. In this chapter, the deep radio data will be cross-matched with optical/near-IR, IRAC, MIPS, and X-ray catalogues to probe the nature of the faint radio population. The multi-wavelength catalogues have a common, overlapping area of $\sim 0.7\,\mathrm{deg}^2$, large enough for cosmic variance effects to not be a major issue. As discussed in Chapter 2, the new radio data presented in this thesis is deep enough to probe the sub-mJy population, and my 6-$\sigma$ catalogue contains a large sample of secure detections.

## 3.2 Multi-wavelength observations of the UDS

### 3.2.1 Optical and near-IR observations

Ground-based near-IR observations of the UDS were obtained as part of UKIDSS (Lawrence et al., 2007) in the $J, H$ and $K$ bands with the Wide-Field Camera (WFCAM – Casali et al., 2007) on UKIRT[1]. These observations covered an area of $0.8\,\mathrm{deg}^2$. The near-IR data used in this Chapter were extracted from the UKIDSS DR1 release (Warren et al., 2007), which includes $J$ and $K$ images reaching 5-$\sigma$ depths of $K = 23.1$ and $J = 23.3$ within a 3-arcsec-diameter aperture. Deep optical images of the UDS comes from observations of the wider Subaru/*XMM-Newton* Deep Survey

[1]The United Kingdom IR Telescope is operated by the Joint Astronomy Centre on behalf of the Science and Technology Facilities Council of the U.K.

(SXDS – Furusawa et al., 2008) area in the $B, V, R, i$ and $z'$ filters with 5-$\sigma$ depths of $B = 27.5, V = 26.7, R = 27.0, i' = 26.8$ and $z' = 25.9$, again within a 3-arcsec-diameter aperture.

An initial catalogue was produced by running source extraction on the *K*- and *z'* band images using SExtractor (Bertin & Arnouts, 1996). Including the deeper *z'*-band image in the initial catalogue allowed for *K*- band sources near the flux limit to be identified. Optical and near-IR catalogues were then constructed by measuring photometry at the positions of the *K*- and *z'*-band sources. The FWHM range for the images are $0.75 < \mathrm{FWHM} < 0.8$ arcsec and so the differential aperture corrections between the images is small. In the final catalogue, only the area where the UDS and SXDS overlap was used, i.e. 0.7 deg$^2$. This catalogue is presented in Cirasuolo et al. (2010), along with a more detailed explanation of the cataloguing process.

### 3.2.2 *Spitzer* observations

Mid-IR observations were made with *Spitzer* using IRAC (at 3.6, 4.8, 5.8 and 8.0 $\mu$m) and MIPS (at 24 $\mu$m), as part of the *Spitzer* UDS program (SpUDS; P.I.: J. Dunlop). The IRAC source catalogue was extracted by initially running SExtractor on the 4.5-$\mu$m image to obtain the positions of sources. Then, photometry was obtained for the remaining images using a 4-arcsec-diameter aperture at the positions of the 4.5-$\mu$m sources. A detailed explanation of the catalogue production can be found in (Caputi et al., 2011). Photometry for the 24-$\mu$m catalogue was obtained using an aperture diameter of 6.225 arcsec, with the appropriate aperture correction from the MIPS documentation. The 24-$\mu$m image is estimated to be 80-per-cent complete at $S_{24} \sim 80\mu$m.

### 3.2.3 X-ray imaging

The wider SXDS field, within which the UDS region resides, was imaged in X-rays by the *XMM- Newton* space telescope. Observations consisted of 7 pointings, covering an area of 1.14 deg$^2$ (all of the area imaged in the optical) in the 0.3–5 keV (ultrasoft), 0.5–2 keV (soft), 2–4.5 keV (medium) and 4.5–10 keV (hard) bands. The image production and source detection are described in Ueda et al. (2008). The final catalogue was determined, through simulations, to have a low contamination rate (0.6–5 per cent from the softest to the hardest bands) of spurious sources.

Source detection is presented in counts ks$^{-1}$ and is converted to a flux using a conversion factor based on the response of the imaging instrument, as provided by Ueda et al.. In order to make a scientific comparison to previous studies, fluxes were combined to give the standard soft (as above) and hard (2–10 keV) bands. Rest-frame luminosities were then calculated using

$$L_{\rm X} = 4\pi D_{\rm L}^2 \, S_{\rm X} (1-z)^{\Gamma-2} \times 10^{-7} \, {\rm W}, \tag{3.1}$$

where $S_{\rm X}$ is the X-ray flux in ergs cm$^{-2}$ s$^{-1}$, $D_{\rm L}$ is the luminosity distance in cm and $\Gamma$ is the photon index, taken to be 1.8 (Barger et al., 2007).

## 3.3 Photometric and spectroscopic redshifts

Here, I use the Cirasuolo et al. (2010) optical/near-IR catalogue to obtain photometric redshifts for the faint radio population in the UDS. To ensure a good fit to galaxy SED models by the photometric redshift code, Cirasuolo et al. improve the wavelength coverage of their sources by including optical observations in the $u, g, r, i,$ and $z$ bands from the Canada-France-Hawaii Telescope, *Spitzer* IRAC mid-IR observations at 3.6 and 4.5 $\mu$m and far- and near-ultraviolet observations from the *Galaxy Evolution Explorer (GALEX)* satellite. Photometric redshifts were then derived with the 16 bands from the far-UV to 4.5 $\mu$m, using a $\chi^2$ minimisation technique based on the publicly available *Hyperz* code (Bolzonella et al., 2000).

Both empirical (Coleman et al., 1980; Kinney et al., 1996; Mignoli et al., 2005) and synthetic templates (Bruzual & Charlot, 2003) were used to model the galaxy SEDs, including a prescription for dust attenuation (Calzetti et al., 2000) and Lyman-series absorption due to the H I clouds in the intergalactic medium, according to Madau (1995).

For the $\simeq$ 1,200 galaxies in the UDS with reliable spectroscopic redshifts, the agreement of the photometric redshifts is good over the full redshift range, $0 < z < 6$. The distribution of the $|\Delta z|/(1+z) \equiv |(z_{\rm spect} - z_{\rm phot})|/(1+z_{\rm spect})$ has a mean consistent with zero (0.008), a standard deviation, $\sigma = 0.034$, and clear outliers make up less than 2 per cent of the total. This accuracy is comparable to the best available from other surveys such as GOODS and COSMOS (Caputi et al., 2006; Grazian et al., 2006; Mobasher et al., 2007). To ensure that only sources with robust photometric redshifts were selected, a $\chi^2 < 15$ cut was imposed.

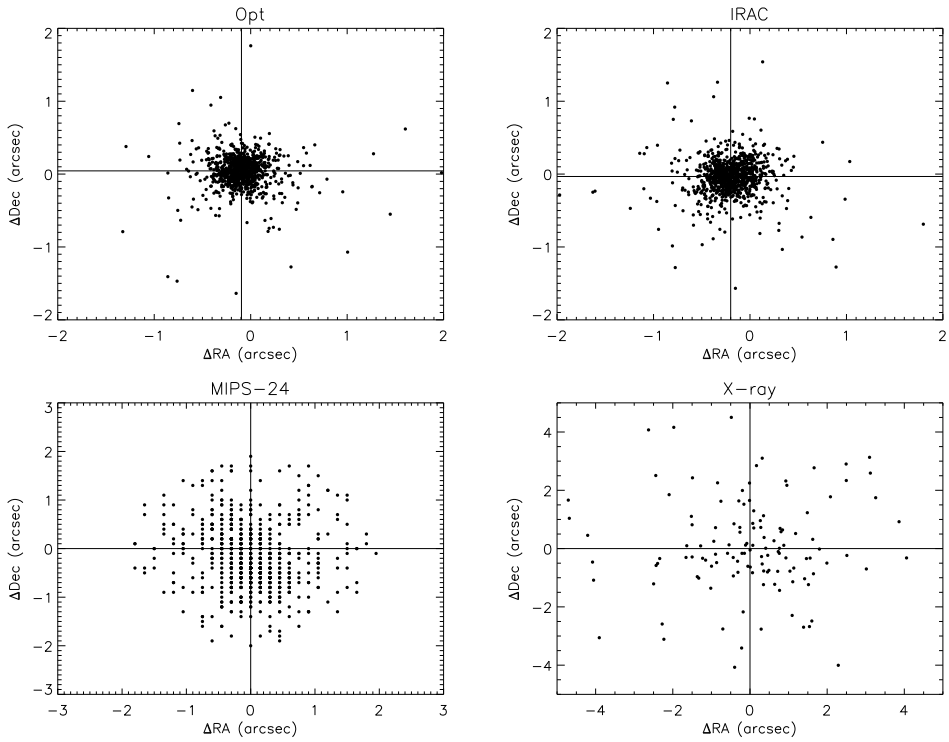


Figure 3.1: R.A. and Dec. offsets for the optical, IRAC, MIPS and X-ray cross-matching. The median offsets, indicated by the cross-hair, is small or zero in all cases and so no astrometric corrections were needed as part of the cross-matching process.

## 3.4 Radio sub-sample

The parent radio sample used for this study is the 6-$\sigma$ catalogue discussed in Chapter 2. A sub-sample of this catalogue was extracted, including only the area which overlaps with the multi-wavelength observations discussed above. This sub-sample, comprising 975 sources, was then cross-matched with the optical/near-IR, IRAC, 24-$\mu$m and X-ray catalogues. Table 3.1 summarises the number of counterpart matches ($N$) for the different catalogues and the search radii ($R$) used to cross-match. As the resulting median positional offsets between radio source and counterpart at all wavelengths were small (see Figure 3.1), no astrometric corrections were needed as part of the cross-matching process. Figure 3.2 shows the cumulative fraction of fluxes for the radio sub-sample. The bulk of the sources (90 per cent) have flux densities, $<$1 mJy, making this sample suitable for studying the nature of the faint, radio population.

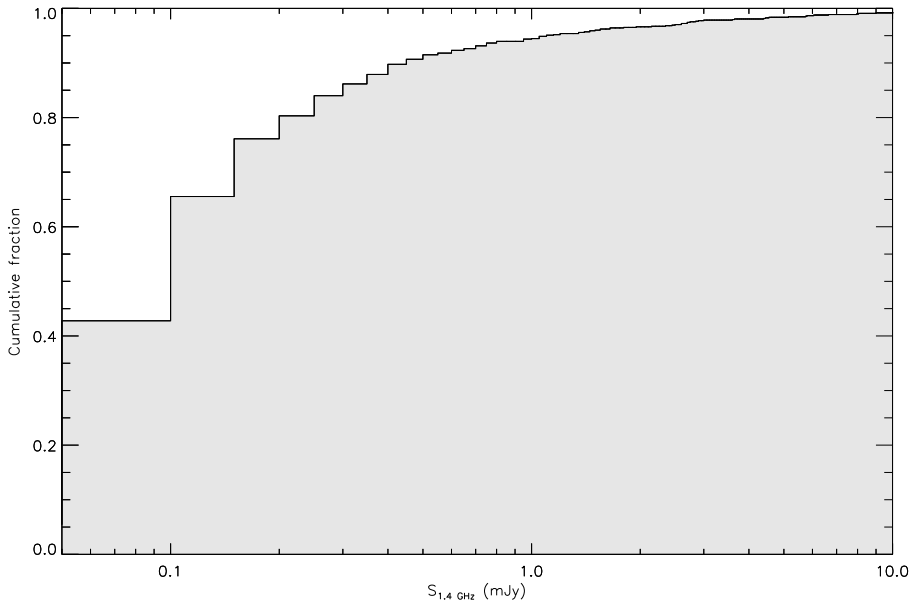


Figure 3.2: Cumulative fraction of $S_{1.4\,\mathrm{GHz}}$ fluxes for the radio sub-sample. The bulk of the sources ($\sim$90 per cent) have flux densities, $<$1 mJy, making the sample suitable for studying the faint, radio population.

Table 3.1: Cross-matching parameters and number of matches, along with the counterpart identification rate.

| Wavelength | $R$ (arcsec) | $N$ |
|---|---|---|
| Optical/near-IR | 2 | 795 (82 per cent) |
| IRAC | 2 | 933 (96 per cent) |
| 24 $\mu$m | 2 | 713 (73 per cent) |
| X-ray | 5 | 124 (13 per cent) |

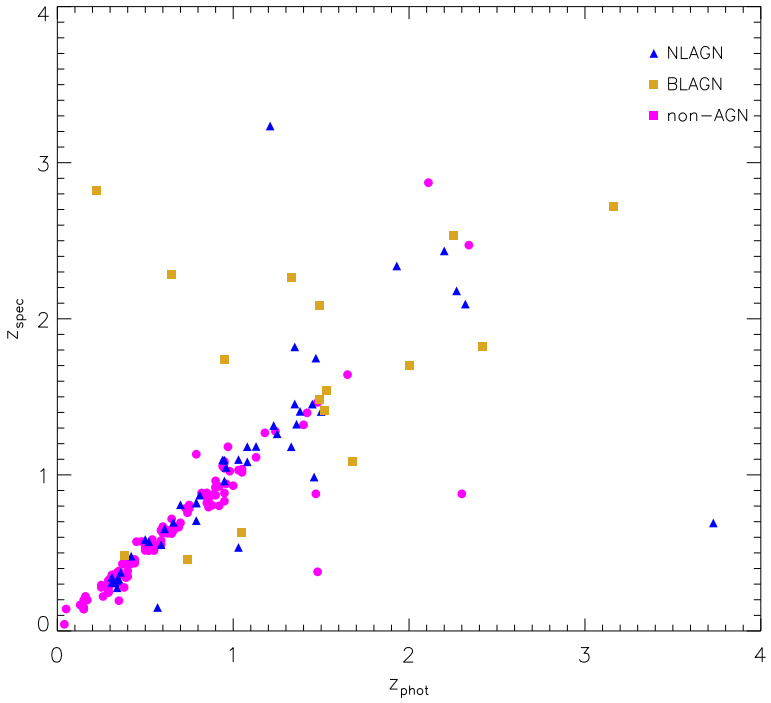


Figure 3.3: A comparison of photometric spectroscopic redshifts from Simpson et al. (2012) for the sample. Spectroscopically determined NLAGN, BLAGN and non-AGN are also indicated in the plot. There is a good agreement between redshifts determined using the two methods for the non-AGN. On the other hand, photometric redshifts for the NLAGN and BLAGN sources have a poor accuracy, especially for the BLAGN. This is due to intervening dust and strong emission lines when measuring broad-band photometry.

## 3.5 Spectroscopic Classification

Spectroscopic classification used for this work was obtained from Simpson et al. (2012). The sample presented in Simpson et al. is smaller (375 sources within the area matching the sub-sample in §3.4) than the one used in this work as it is derived from shallower observations (Simpson et al., 2006). Out of the 375 sources matched to the sub-sample, 198 had robust spectroscopic redshifts and classifications. Where available, photometric redshifts were replaced with spectroscopic redshifts.

Objects were classified as starburst (SB), narrow-line AGN (NLAGN), broad-line AGN (BLAGN), absorbers or strong and weak based on the strength of the O II emission line. Due to the uncertain nature of absorbers, strong and weak sources – these could either be AGN or starburst regions – only SB, NLAGN and BLAGN spectral types were used for classification. The fraction of sources with spectroscopic

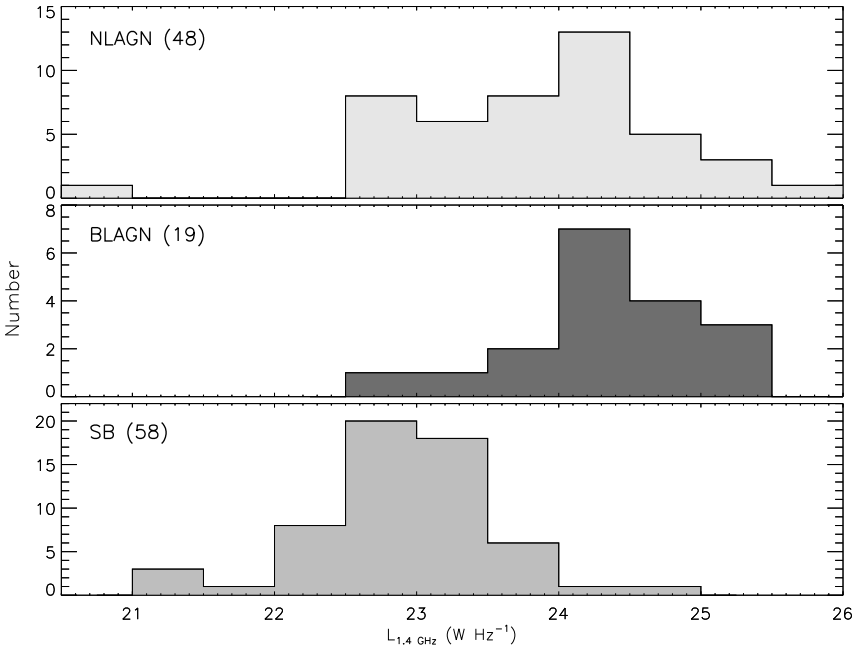


Figure 3.4: Luminosity distributions of the sources spectroscopically determined to be NLAGN (blue triangles), BLAGN (golden squares), and SB (magenta circles). Based on these distributions, $L_{1.4\,\mathrm{GHz}} > 10^{24}\,\mathrm{W\,Hz^{-1}}$ was chosen to be a radio luminosity-based selection criteria for AGN.

data identified to be AGN (NLAGN and BLAGN) is 33 per cent.

Figure 3.3 shows a comparison of the photometric and spectroscopic redshifts. With the exception of four outliers, photometric redshifts of non-AGN sources agree well with their spectroscopically-determined redshifts. While there is still a reasonable agreement between photometric and spectroscopic redshifts for NLAGN, the overall AGN sample shows poorly determined photometric redshifts. This is due to broad-band photometry being affected by dust emission and strong emission lines, highlighting the importance of spectroscopic follow-up. However, as discussed in Section 3.3, the photometric redshifts determined for this sample generally have small uncertainties.

Figure 3.4 shows the luminosity distribution for NLAGN, BLAGN and SB. Based on the distribution of NLAGN and BLAGN, a radio luminosity of $L_{1.4\mathrm{GHz}} > 10^{24}\,\mathrm{W\,Hz^{-1}}$ will be applied as a threshold above which sources are considered to be an AGN.

## 3.6 Near-IR properties of the radio sample

IRAC colour-colour diagnostics (Lacy et al., 2004; Stern et al., 2005) are popular ways of distinguishing AGN from SFGs. Mid-IR selection of AGN is effective due to the difference in SED shape between SFGs and AGN; the SED of AGN in the mid-IR region will continue to rise, following a power law, whereas the SED of an SFG will start to fall after a peak at $\sim 1.6\mu$m. Figure 3.5 displays the IRAC colour-colour diagnostic introduced by Stern et al. (2005) to select AGN. The following loci define the area within which sources are taken to be an AGN (hereafter referred to as the "Stern wedge"):

$$
\begin{aligned}
& m_{5.8} - m_{8.0} > 0.6, \\
& m_{3.6} - m_{4.5} > 0.2(m_{5.8} - m_{8.0}) + 0.18 \quad \text{and} \\
& m_{3.6} - m_{4.5} > 2.5(m_{5.8} - m_{8.0}) - 3.5,
\end{aligned}
$$

where *m* is the Vega magnitude for each IRAC filter.

Using the spectroscopic classification discussed above, NLAGN, BLAGN and starburst (SB) galaxies are identified on the plot. Only 3 per cent of the SB sources have been identified as AGN, indicating that there is a low contamination of SFGs in the Stern wedge, making this a robust method of identifying a clean sample of AGN. Only 44 per cent of the NLAGN are recovered in the Stern wedge, so a large fraction of NLAGN are missed using this method and IRAC colour-colour selection is clearly not a foolproof method of selecting obscured AGN.

Figure 3.6 displays contours of the fraction of radio-selected AGN in a given 'cell' – with cells defined by binning the IRAC colour-colour space. This shows where the radio-selected AGN lie in the colour-colour diagram. A non-negligible fraction of these radio-selected AGN (which are shown by the grey-shaded region in Figure 3.6) are missed by the Stern wedge. Brusa et al. (2010) indicate that sources located in this region of the IRAC colour-colour diagram are high-redshift obscured AGN; the redshifts of these objects are shown as the grey-shaded histogram, inset as part of Figure 3.6, compared to the redshift distribution of other sources on the colour-colour diagram. This confirms that the Stern wedge misses obscured AGN. At $z \geq 1$, the stellar SED starts to redden and so the grey-shaded region will be a mix of obscured AGN and normal high-redshift galaxies.

However, having recovered 84 per cent of the BLAGN, this method is ideal for

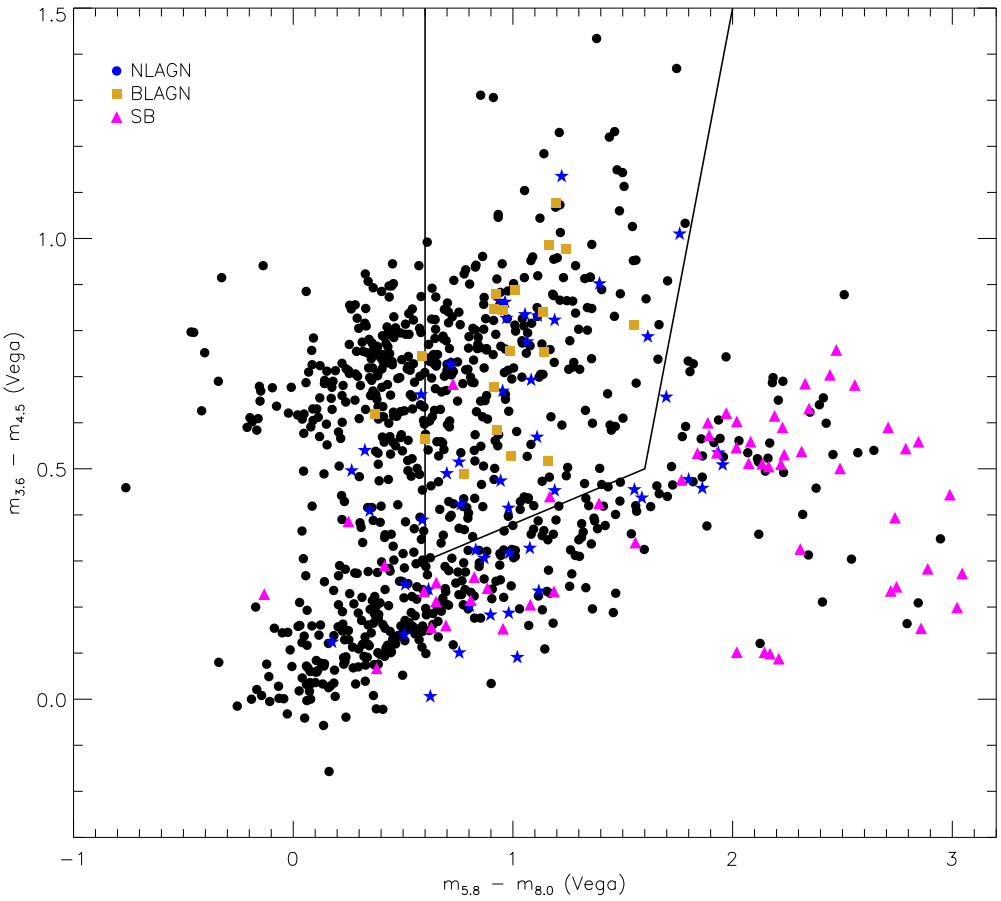


Figure 3.5: IRAC colour-colour plot for the radio subsample, with the solid lines indicating the region within which AGN are expected to lie due to their power-law IR SED. The positions of NLAGN (blue circles), BLAGN (golden squares) and SB (magenta triangle) indicate that this technique is ideal for identifying unobscured AGN (BLAGN), with a very low contamination rate of SFGs.

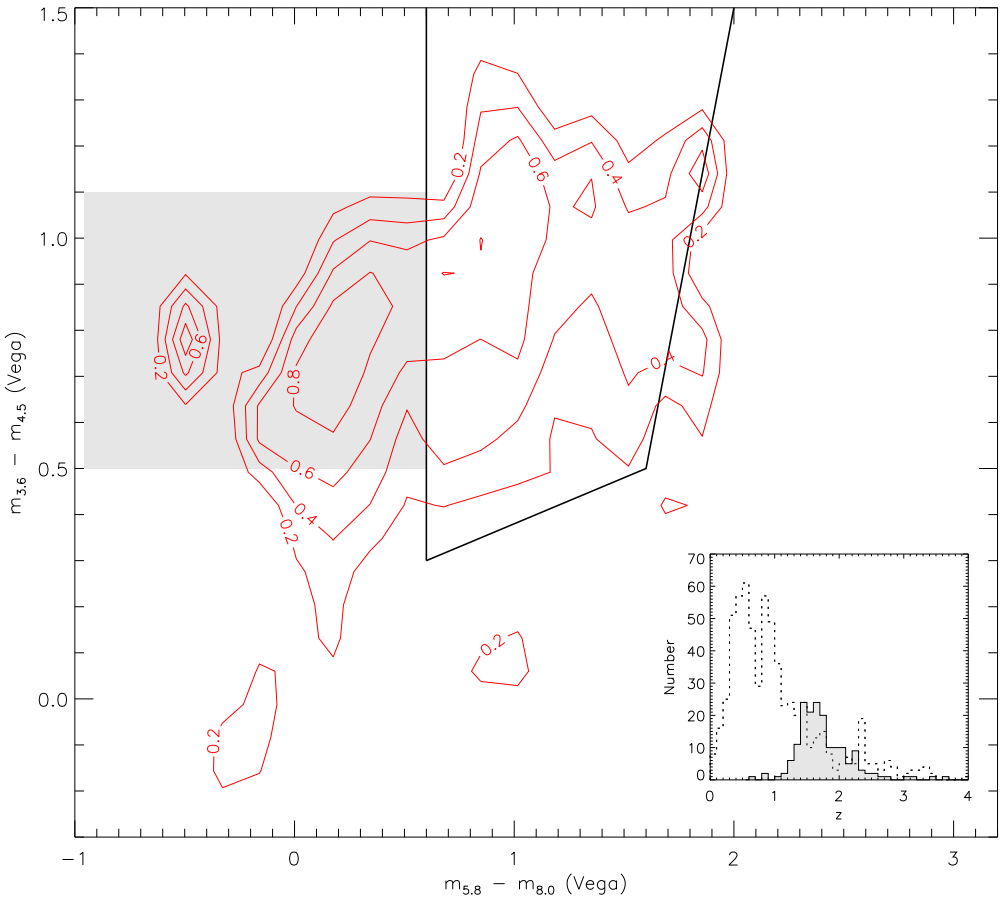


Figure 3.6: Contour plot of the fraction of radio-selected AGN out of all sources in a given 'cell'. A significant fraction lie in the grey-shaded region, missed by the Stern wedge. *Inset:* the redshift distribution of the whole sample, compared to the redshift distribution of the radio-selected AGN sample that lies in the grey-shaded area. It has been suggested that these sources are high-redshift obscured AGN, confirming that the IRAC AGN selection method is not ideal for obscured AGN.

identifying unobscured AGN and is still clearly a powerful selection technique for selecting AGN. The total AGN fraction of the radio sample identified using the Stern et al. (2005) mid-IR selection is 31 per cent.

## 3.7 Mid-IR (24-$\mu$m) properties of the radio sample

The far-IR/radio correlation is a well-known method of selecting radio-excess AGN. The sample was limited to sources with $S_{24\mu\mathrm{m}} > 80\mu Jy$ to reduce the risk of including spurious sources. This flux limit corresponds to a SNR of $\sim 3.5\sigma$ in the 24-$\mu m$ data.

The far-IR/radio correlation will be presented here in the form of the $q$-parameter, $q_{24} = \log(S_{24\mu\mathrm{m}}/S_{1.4\mathrm{GHz}})$, as a function of redshift. While this correlation is sometimes investigated using bolometric far-IR flux, this work is limited to 24-$\mu$m flux densities due to the lack of longer wavelength coverage at the time of writing.

To obtain rest-frame 24-$\mu$m and radio fluxes, the data has to be *K*-corrected. As the definition of redshift is given by $(1+z) = \nu_{\mathrm{rest}}/\nu_{\mathrm{obs}}$ and since the radio regime of the SED follows a power-law ($S_\nu \propto \nu^\alpha$, where $\alpha$ is the spectral index), the *K*-correction is given by $K = S_{\nu,\mathrm{rest}}/S_{\nu,\mathrm{obs}} = (1+z)^\alpha$. Then,

$$L_{\nu,\mathrm{rest}} = \frac{4\pi D_{\mathrm{L}}^2}{(1+z)} S_{\nu,\mathrm{obs}} (1+z)^{-\alpha} = 4\pi D_{\mathrm{L}}^2 \frac{S_{\nu,\mathrm{obs}}}{(1+z)^{-\alpha}}. \tag{3.2}$$

The spectral index is taken to be $-0.8$, appropriate for SFGs (e.g. Ibar et al., 2009). The *K*-correction in the 24-$\mu$m band was done following the method of Ivison et al. (2010a), i.e. a correction using an M82 SED template. Again, this correction is based on SFGs, of which M82 is an archetypal example. In addition to this, Ibar et al. (2008) find that in a comparison to other star-forming SED templates, the M82 template yields the least scatter in $q_{24}$.

The *K*-corrected $q_{24}$ is shown in Figure 3.7, along with the distribution of $q_{24}$ values. When calculating the mean, a robust statistical method needs to be used to ensure that the result is not skewed by the radio-excess sources. A biweight estimator (Beers et al., 1990) is used to locate the mean and scatter of the data; in the range $0 < z < 3.5$, $q_{24} = 0.93 \pm 0.36$. This is shown as the dashed line on the histogram in Figure 3.7 and agrees with results from previous studies of the far-IR/radio correlation using 24-$\mu$m monochromatic flux density (Appleton et al., 2004; Donley et al., 2005a; Del Moro et al., 2013). Based on the distribution of $q_{24}$ values (see histogram in Figure 3.7), a 2-$\sigma$ boundary was taken to be the limit below which sources are considered to have

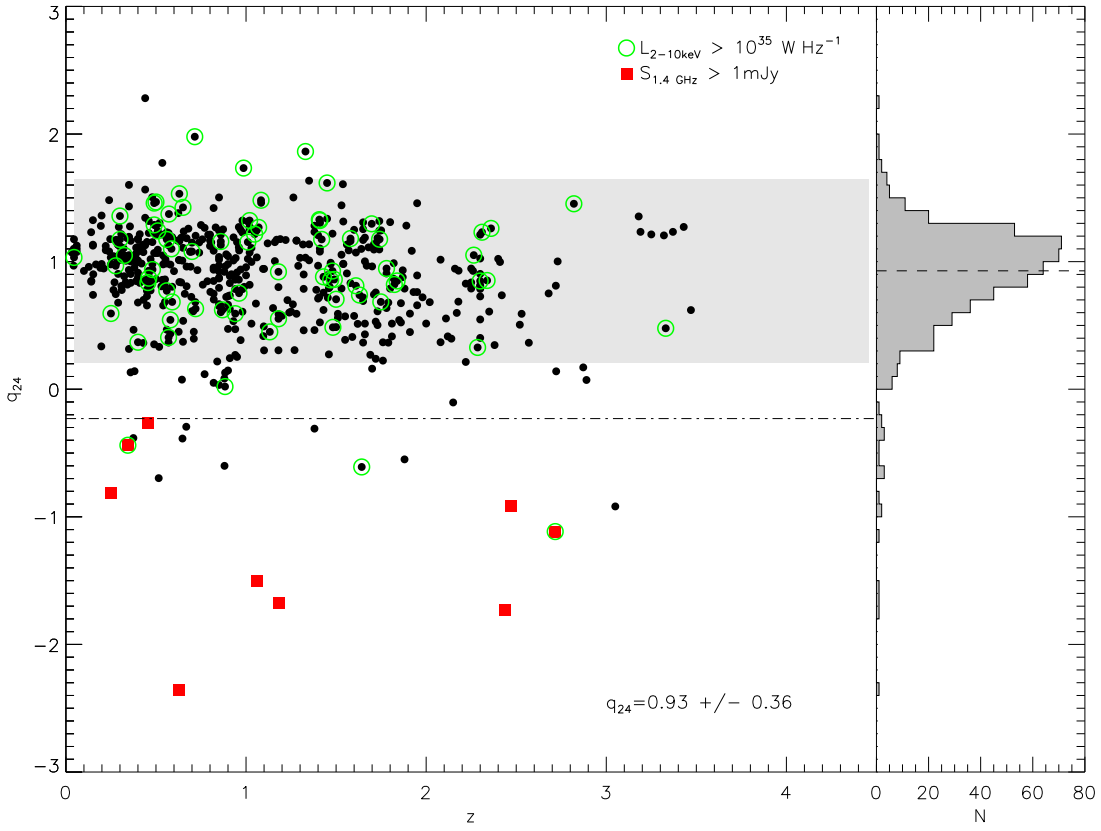


Figure 3.7: *K*-corrected $q_{24}$ values, where the ratio of 24-$\mu$m to radio fluxes is used as a proxy for the far-IR/radio correlation. The grey-shaded region represents the 2-$\sigma$ region of the $q_{24}$ value, $0.93 \pm 0.36$, within which sources are considered to be SFGs. This boundary was chosen using the distribution of $q_{24}$ values, as shown in the side plot; the dashed line here represents the calculated $q_{24}$ value. The dot-dashed line is the boundary below which Ibar et al. (2008) identify sources as being radio-loud AGN. Reassuringly, all sources with $S_{1.4\,\mathrm{GHz}} > 1$ mJy lie below this line. A large number of X-ray identified AGN (green circles) are seen to lie within the 2-$\sigma$ region, suggesting that these are possibly radio-quiet AGN as they are also expected to follow the far-IR/radio correlation.

radio-excess emission, i.e. at $q < 0.57$. A line at $q_{24} = -0.23$ is also included; this is taken as the boundary below which Ibar et al. (2008) classify sources as radio-loud AGN. Reassuringly, all sources with $S_{1.4\mathrm{GHz}} > 1$ mJy) lie below this limit.

Sources with X-ray counterparts having $L_{2-10\mathrm{keV}} > 10^{35}\,\mathrm{W\,Hz^{-1}}$ are also identified on the plot. The presence of these X-ray selected AGN in the region taken to follow the far-IR/radio correlation suggest that these are possibly radio-quiet AGN, as these are expected to follow the correlation too (Condon, 1992). Hence, the far-IR/radio correlation also acts as a means of distinguishing radio-quiet AGN from their radio-loud counterparts. By this assumption, $\sim$67 per cent of the AGN with a 24-$\mu$m detection are radio-quiet AGN. This result is similar to the findings of Padovani et al. (2011), who argued that radio-quiet AGN make up 60 per cent of all AGN in their sample. This would imply that radio-quiet AGN make up an important portion of the faint radio population. However, due to the uncertainties in this method (e.g. the large scatter seen in Figure 3.7 and the use of a monochromatic mid-IR flux density rather than a bolometric flux), this classification of radio-quiet AGN will not be applied to the sample. More robust methods such as those involving the radio/optical ratio and resolved jet morphologies are needed to confirm this.

## 3.8 X-ray properties of the radio sample

Hard X-ray observations are an efficient way of identifying the presence of AGN in Compton-thin sources (column densities $N_{\mathrm{H}} > 10^{24}\,\mathrm{cm^{-2}}$), where X-ray sources with $L_{2-10\mathrm{KeV}} > 10^{35}\,\mathrm{W\,Hz^{-1}}$ are considered to be AGN (e.g. Mushotzky, 2004; Barger et al., 2007). The use of hard X-rays ensures both obscured and unobscured Compton-thin sources are selected. A majority of sources with X-ray counterparts were identified as AGN, with 2–10-keV luminosities above the AGN threshold – the dashed lines on Figure 3.8(a) indicate the X-ray and radio luminosity thresholds for AGN identification. Also indicated are spectroscopically identified SFGs. In concordance with the imposed threshold, all but one source have $L_{2-10\mathrm{KeV}} < 10^{35}\,\mathrm{W\,Hz^{-1}}$. The one source lying above the threshold is likely to be an obscured AGN, which would explain why it did not display an AGN signature in its spectrum.

Figure 3.8(b) shows the fraction of X-ray-identified AGN out of all AGN identified sources – using all the diagnostic methods discussed above – for the sub-mJy population, while the inset shows the distribution of radio flux densities for the X-

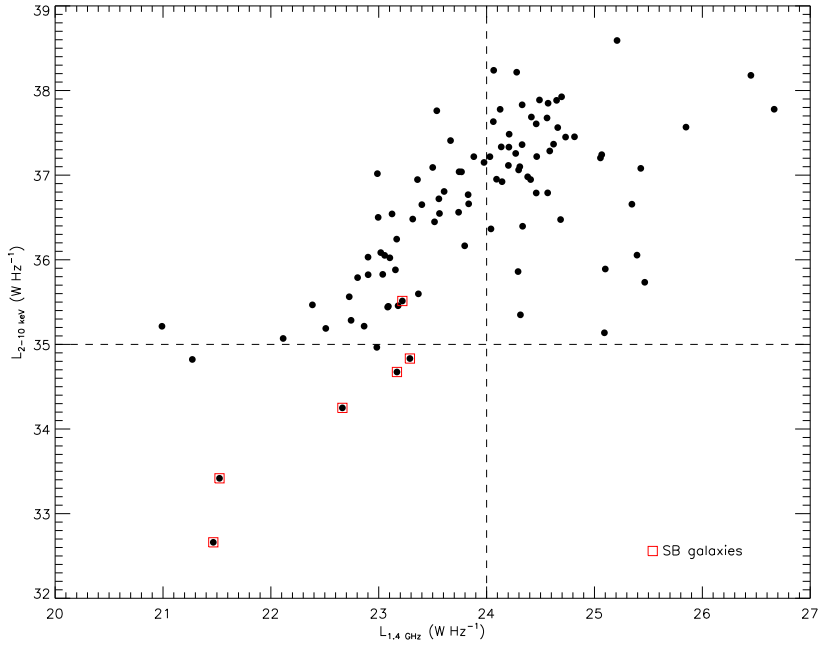


(a)

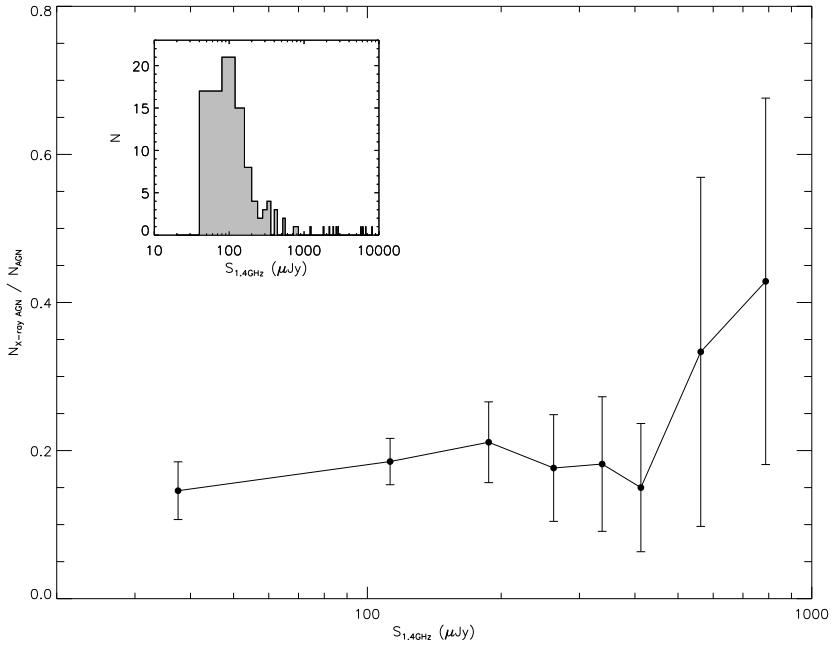


(b)

Figure 3.8: (a) Hard X-ray luminosity versus radio luminosity for the X-ray identified sources. The dashed lines show the radio- and X-ray AGN selection at $L_{1.4\,\mathrm{GHz}} > 10^{24}\,\mathrm{W\,Hz^{-1}}$ and $L_{2-10\,\mathrm{keV}} > 10^{35}\,\mathrm{W\,Hz^{-1}}$. Red squares indicate SB sources, of which all but one lie outside of the AGN regions. (b) Fraction of X-ray-identified AGN out of the whole AGN sample as a function of radio flux. *Inset:* Distribution of radio flux density for the X-ray-identified AGN sample.

Table 3.2: Summary of AGN/SFG diagnostics.

| Diagnostic | $N_{\rm det}$ | $N_{\rm AGN}$ |
|---|---|---|
| $L_{1.4\rm GHz}$ | 823 | 324 (39 per cent) |
| Spectra | 198 | 67 (13 per cent) |
| IRAC colours | 929 | 288 (31 per cent) |
| $q_{24}$ | 557 | 33 (6 per cent) |
| $L_{2-10\rm keV}$ | 99 | 92 (93 per cent) |

ray-identified AGN. The majority of the X-ray sources are found at faint radio flux densities, $< 300\mu$Jy, although X-ray AGN only make up a small portion of the overall AGN identified sources, i.e. 15–20 per cent up to $S_{1.4\,\rm GHz} \sim 500\,\mu$Jy. This suggests that the bulk of the radio-quiet sources are X-ray-obscured, and possibly Compton-thick AGN, detectable using other diagnostics as the source of the IR emission is an AGN-heated torus and radio emission does not suffer obscuration. This result can best be tested by measuring X-ray fluxes at higher energies. Newer telescopes like *NuSTAR* (Harrison et al., 2010), which are capable of observing harder X-rays – as well as the large effective collecting area needed to probe faint sources – will need to be employed for such a task.

## 3.9 Nature of the faint radio population

The results of the diagnostics exploited here to distinguish AGN from SFGs are summarised in Table 3.2. These classifications are then applied to the entire sample, where sources identified as AGN by at least one diagnostic method are considered to be AGN.

### 3.9.1 Luminosity and redshift distributions

Figure 3.9 is a plot of radio flux density versus radio luminosity for sources identified as SFGs and AGN. As can be seen from the plot, AGN are found even at the faintest fluxes, indicating that the sub-mJy population consists of a mix of AGN and SFGs, down to fluxes close to the flux limit of the catalogue (dashed line in Figure 3.9). At flux densities $\lesssim 200\mu$Jy, sources have a wide range of luminosities – a combination of low-luminosity sources at low redshift and luminous high-redshift sources, the latter being primarily AGN.

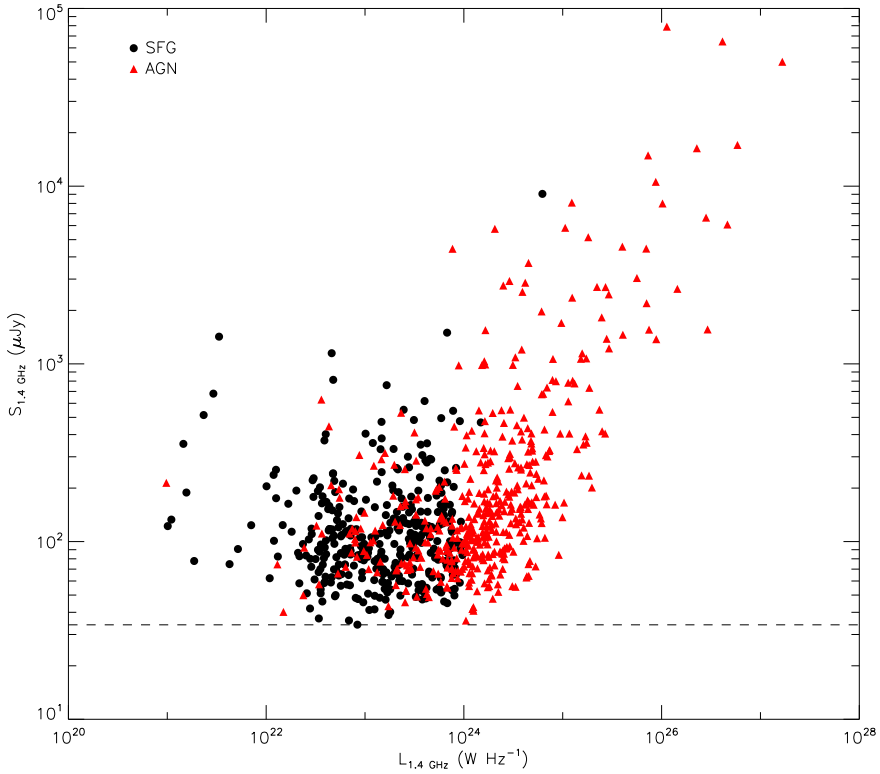


Figure 3.9: Radio flux density versus radio luminosity. SFGs and AGN are marked as black filled circles and red triangles, respectively. There is a significant contribution of AGN at lower fluxes, indicating that the sub-mJy population consists of a mix of AGN and SFGs.

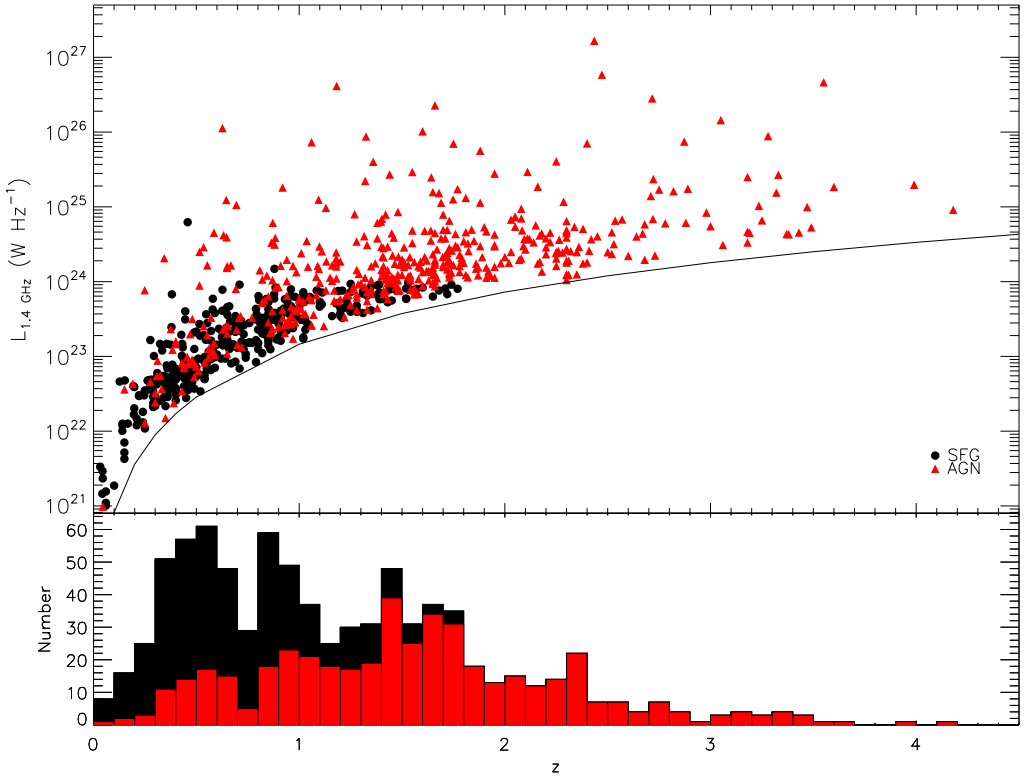


Figure 3.10: *Top:* 1.4-GHz luminosity as a function of redshift for the radio sub-sample, with AGN marked as red triangles and SFGs as black filled circles. The curved solid line indicates the flux limit of the sample, at $\sim 35\mu$Jy. *Bottom:* Redshift distribution of the radio sample, split into AGN and SFG contributions.

The 1.4-GHz luminosity and redshift distributions are shown in Figure 3.10. Low-radio-luminosity sources are dominated by the star-forming population and the dominance then shifts to AGN at higher luminosities. At low redshifts ($z < 1$), most sources have low luminosities and the converse is found at high redshifts. A small range of luminosities is observed at recent epochs and the range gets wider at higher redshifts. Condon (1989) suggest that a luminosity evolution can be inferred from these results.

The median redshifts for the star-forming and AGN population are 0.64 and 1.73, respectively. The redshift distributions show that more recent epochs are dominated by the presence of SFGs and earlier epochs tend to favour AGN. At $z > 2$, the observed radio population is completely dominated by AGN. This is likely affected by Malmquist bias, where only the most luminous sources from this epoch are detected in the observations.

### 3.9.2 Partitioning the radio population between AGN and SFGs

Applying the selection criteria discussed so far to the whole sample yields an AGN fraction of 53 per cent. The AGN population makes a significant contribution to the sub-mJy population. As discussed earlier, my findings agree with recent studies of the faint radio population (Smolčić et al., 2008; Padovani et al., 2011; Willner et al., 2012).

It is useful to investigate the evolution in the fractions of AGN and SFGs as a function of flux. Figure 3.11 shows the Euclidean source counts for the total sub-sample and the AGN and SFGs. In the lowest flux-density bin (30–100 $\mu$Jy), SFGs are the dominant population, making up 57 per cent of the sources. The AGN fraction then rises at a considerable rate, reaching $\sim 80$ per cent at around 1 mJy. Beyond this flux limit, radio-loud AGN dominate the source counts, up to a 100 per cent in some of the brighter bins. Exceptions to a completely AGN-dominated flux bin above this level are due to the presence of a few bright, local starburst galaxies.

The flattening seen in radio source counts below 1 mJy is then due to the emergence of a population of SFGs. While the sub-mJy regime down to $\sim$0.1 mJy is dominated by AGN, SFGs start to outnumber AGN below 0.1 mJy. However, Padovani et al. (2011) predict that the $\mu$Jy regime should also contain a significant radio-quiet AGN contribution. A robust technique is needed to separate out radio-quiet AGN – part of on-going work with e-MERLIN, amongst other SKA precursors and pathfinders.

Exploring the fainter counts ($S_{1.4\,\mathrm{GHz}} \approx 10\,\mu$Jy) requires the next generation of telescopes as improvements in both sensitivity and resolution are required. This is is not limited to the radio window. As I have demonstrated already, complementary data at shorter wavelengths is required to classify sources accurately. In the present day, deep imaging of the far-IR sky by *Herschel* is providing better constraints for techniques that exploit the far-IR/radio correlation. Looking further to the future, the European Extremely Large Telescope and the *James Webb Space Telescope* will be able to provide counterparts to $\mu$Jy sources, allowing their classification.

## 3.10 Conclusions

In this Chapter I have classified faint radio sources as either SFGs or AGN. To accomplish this, the robust 6-$\sigma$ radio catalogue introduced in Chapter 2 was cross-matched with complementary optical/near-IR, spectroscopic, mid-IR, 24-$\mu$m and X-ray catalogues. The bulk of the sources ($\sim 90$ per cent) lie in the sub-mJy regime,

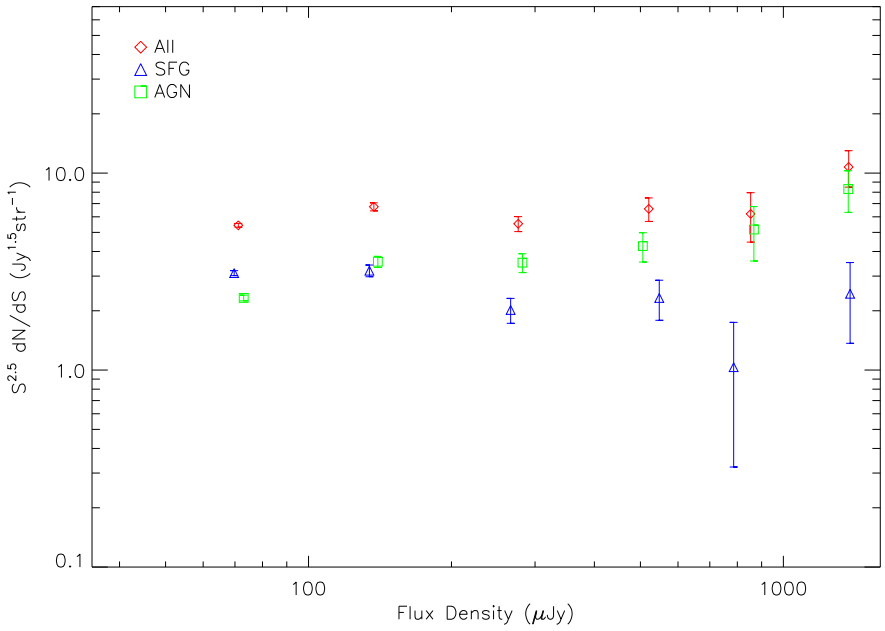


Figure 3.11: Euclidean-normalized source counts at 1.4 GHz for the whole sample (red diamonds) and for the sample decomposed into AGN (green squares) and SFGs (blue triangles). The counts and their respective error bars were derived as discussed in Chapter 2.

making this sample ideal for probing the nature of the faint, radio population.

Recently published spectroscopic information on a subset of the radio sources was included to identify NLAGN, BLAGN and star-forming sources, classifying 13 per cent of the detected sources as AGN. The radio luminosity distributions of these sources were used to decide upon a radio-luminosity-based AGN selection threshold, $L_{1.4\,\mathrm{GHz}} > 10^{24}\,\mathrm{W\,Hz^{-1}}$. IRAC colour-colour diagnostics were then employed. While this method was effective at selecting a clean sample of AGN, it was shown to be biased towards selecting unobscured AGN: a significant number of radio-selected AGN at high redshift were missed by this selection technique. Hard X-ray detection of $L_{2-10\,\mathrm{keV}} > 10^{35}\,\mathrm{W\,Hz^{-1}}$ was taken to be an AGN. Hard X-rays were used, instead of soft X-rays, to ensure that both obscured and unobscured sources are selected.

*K-corrected* 24-$\mu$m and radio data were used to quantify the far-IR/radio correlation, via $q_{24}$. Ideally, bolometric far-IR luminosities should be used to quantify $q$, but far-IR observations at longer wavelengths and with sufficient depth was not available at the time of this investigation. Sources outwith a 2-$\sigma$ region of $q_{24}$ $(0.93 \pm 0.36)$ were classified as AGN. The $q_{24}$ classification yielded an AGN identification rate

of only 6 per cent. A number of X-ray identified sources were found to lie within the 2-$\sigma$ region. As radio-quiet AGN are also expected to follow the far-IR/radio correlation, this suggests the potential to separate out radio-quiet from radio-loud AGN using the $q$ parameter. Taking any X-ray-identified source found in the 2-$\sigma$ region to be a radio-quiet AGN, they make up 67 per cent of the entire AGN population – a significant fraction. As was discussed in Section 3.9.2, this AGN population is expected to contribute to the $\mu$Jy population and so it is important to understand their role. However, due to the large scatter when using $q_{24}$, an evaluation of the radio-quiet AGN population was not included in this work.

If we classify a source as an AGN if at least one of the diagnostics identifies the source as such, then 53 per cent of the overall sample was found to comprise AGN. This agrees with recent studies suggesting that AGN make a significant contribution to the sub-mJy population. Above 1 mJy, radio-loud AGN are shown to dominate the source counts. Below this flux limit, a flattening is seen due to the emergence of a star-forming population. However, AGN continue to dominate the 0.1–1 mJy flux-density region. Below 0.1 mJy, SFGs dominate, though there is a significant contribution from radio-quiet AGN.

More robust methods of separating out radio-quiet AGN are needed. One additional diagnostic which could be used to classify sources is their optical/near-IR morphologies, e.g. from CANDELS observations. While Chapter 4 does address the morphologies of my faint radio sample, the work done there concentrates on tracing merger activity.

The median redshifts for the star-forming population and the AGN are 0.64 and 1.73, respectively; at $z > 2$, the population consists entirely of AGN though this could be due to Malmquist bias.

Draper et al. (2011) find that the faint, radio population presented in the literature make up only 60 per cent of the cosmic radio background. Deeper surveys are needed to probe the $\mu$Jy population, to classify these sources and to better understand the faint, radio population. Upcoming surveys with the SKA, down to nanoJy fluxes, will provide fresh insight.

# Chapter 4

# Morphologies of the faint radio population

## 4.1 Introduction

Inferring properties such as mass, age and star-formation rates require a number of assumptions to be made, e.g. the adoption of a universal initial mass function. On the other hand, galaxy morphology is a direct observable, making it one of the most accessible methods of studying galaxy evolution and formation. Being correlated to other properties such as star-formation activity, galaxy morphology plays an important role in constraining theories of galaxy formation and evolution.

Early morphological studies by Edwin Hubble, resulted in the broad classification of galaxies into ellipticals, spirals and lenticulars – the Hubble Sequence (Figure 4.1; Hubble, 1936). Although Hubble did not intend the position on the diagram to reflect a sequence, an early and erroneous interpretation of the Hubble diagram was that it was an evolutionary sequence, where galaxies start of as ellipticals, become lenticulars then eventually become spirals. This misinterpretation led to elliptical galaxies being referred to as 'early-type galaxies' and spirals as 'late-type galaxies'. The Hubble scheme of galaxy classification is still commonly used, as the classifications are broad enough to accommodate most galaxies.

In the local Universe, galaxy morphology is seen to reflect the star-formation activity of a galaxy: elliptical galaxies have low or quenched star-forming activity (quiescent galaxies); SFGs have disk-dominated morphologies. Hierarchical galaxy-formation models suggest that ellipticals are formed from the mergers of spiral

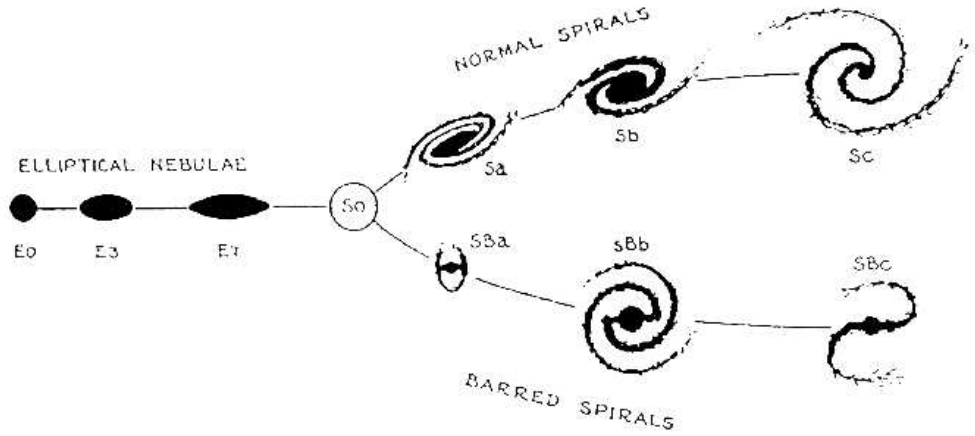


Figure 4.1: Hubble's classification scheme (Hubble, 1936).

galaxies, meaning that there is a possibility of morphological transformations halting star-formation activity. However, at high redshift a different picture is seen: quiescent galaxies have a more significant disk component (e.g. van der Wel et al., 2011). Given the link between star formation activity and galaxy morphology, tracing the evolution of morphologies will contribute towards a better understanding of how galaxies assemble their mass.

Morphological analysis is also a useful tool for identifying the end products of galaxy mergers and interactions. The cold dark matter model, for which there is strong observational evidence (e.g. Spergel et al., 2007), suggests that cosmological structures grow hierarchically, i.e. through mergers. While some observations suggest that galaxy interactions and mergers are responsible for the bulk of star formation in the early Universe (e.g. Bridge et al., 2007; Conselice et al., 2008; Engel et al., 2010), the role of mergers and interactions in galaxy evolution is not fully understood. It is therefore important to track merger fractions and morphologies to better understand the processes responsible for star formation and galaxy assembly, particularly during the epoch when the Universe was undergoing increased star-formation activity ($z \sim 1-3$).

## 4.2 Quantifying galaxy morphology

Galaxy morphologies are characterised on the basis of their observed two-dimensional projection on the plane of the sky, e.g. radial light profile, size, sub-structures such as arms, and so on. Morphological classifications were traditionally done through

visual inspection but automated methods had to be developed to deal with increasingly large volumes of data from extragalactic imaging surveys. Automated morphological characterisation has the added benefits of consistency – eliminating biases caused by different individual interpretations – and being able to better quantify the presence of faint sub-structures in distant galaxies. Measurements of galaxy morphology are done either through model based or model-independent (non-parametric) automated fitting. Some common methods used to quantify galaxy morphology are discussed below.

Model-based techniques fit a pre-defined model to the surface brightness profile. The advantage of this method is the ability to decompose the light into a bulge and a disk component, allowing for the structure of the galaxy to be quantified. However, an issue with this method is that the fitting depends heavily on the assumption of the light profile and on the galaxy having well-defined sub-structures. This creates a problem when trying to quantify the morphologies of galaxies at high redshift, since sub-structures are not be as nicely defined as in the local Universe. This will also be an issue for peculiar galaxies and for galaxies with structural disruptions caused by clumps of star-formation activity and mergers.

The strength of 'non-parametric' methods is that no analytic solution for the light profile of the galaxy is assumed, allowing for irregulars and galaxies with disrupted structures to be distinguished from Hubble-sequence galaxies. This also makes classifications of high-redshift galaxies possible. Decomposing bulge from disc luminosity is, however, not possible through non-parametric methods.

### 4.2.1 Sersic index

A galaxy profile shape can be obtained by fitting a Sersic profile (Sersic, 1968; Simard et al., 2002), which is a radial profile of surface brightness of the form:

$$\Sigma(r) = \Sigma_e \left\{ -k \left[ \left( \frac{r}{r_{\rm e}} \right)^{\frac{1}{n}} - 1 \right] \right\}, \tag{4.1}$$

where $\Sigma(r)$ is the surface brightness at some radius, *r*, $\Sigma_e$ is the surface brightness over the area of radius, $r_e$, within which half of the galaxy's light is contained, *k* is a parameter set to $1.9992n - 0.3271$ so that $r_{\rm e}$ is always the projected half-light radius and *n* is the Sersic index. Bulge-dominated and early-type galaxies which follow the classical de Vaucouleurs profile will have a $n = 4$ profile, whereas late-type galaxies will have a $n = 1$ profile. Multi-component models, using a bulge and a disk model,

can be used to measure how disk-dominated or bulge dominated a galaxy is (Mendez et al., 2011; Bruce et al., 2012).

### 4.2.2 *CAS* parameters

A widely used, model-independent method of quantifying galaxy morphology is the *CAS* system (Bershady et al., 2000; Conselice, 2003), based on concentration of stellar light (*C*), asymmetric distribution (*A*), and clumpiness (*S*).

The concentration index is defined by

$$C = 5 \log \left( \frac{r_{80}}{r_{20}} \right) \tag{4.2}$$

where $r_{20}$ and $r_{80}$ are the radii of the aperture within which 20 and 80-per-cent of the total light is contained, respectively. *C* is higher for elliptical galaxies as their light is more concentrated; $C$ decreases for disc galaxies.

The asymmetry index is given by a summation of the absolute values of the difference between the pixel intensities of an image of the galaxy ($I$ (*i, j*)) and an image of the galaxy rotated by 180° about it's centre ($I_{180}$ (*i, j*)), then normalised to the original total flux of the galaxy:

$$A = \frac{\sum_{i,j} |I(i,j) - I_{180}(i,j)|}{\sum_{i,j} |I(i,j)|}. \tag{4.3}$$

Ellipticals have a low asymmetry index due to their smooth light profiles; a higher *A* could be due to structures such as spiral arms, mergers, star-forming regions and 'irregular' features.

Finally, the measure of clumpiness (*S*) is given as the summation of the absolute value of the difference between the pixel intensities of an image of a galaxy ($I$ (*i, j*)) and the pixel intensities of a smoothed image of the galaxy ($I_S$ (*i, j*)), normalised to the original total flux of the galaxy:

$$S = \frac{\sum_{i,j} |I(i,j) - I_S(i,j)|}{\sum_{i,j} |I(i,j)|}. \tag{4.4}$$

Clumpiness is a measure of the amount of high-spatial frequency structure in the galaxy. Smoothing the image lowers the image resolution, generally speaking, removing any high spatial frequencies and structure. Hence, subtracting the smoothed image from the original gives a residual image containing only high-frequency

components. A low number of residuals will then indicate a galaxy with a low degree of clumpiness, and hence a low *S*. The presence of clumps at high spatial frequencies is usually indicative of a star-forming galaxy as these are usually patchy and contain more structure at high spatial frequencies.

### 4.2.3 Gini and $M_{20}$

Like the *CAS* classification, Gini and $M_{20}$ (Lotz et al., 2004) are another form of model-independent classification scheme; the two are complementary to each other. The Gini coefficient describes the distribution of pixel fluxes. As given in Lotz et al. (2004), Gini is given by

$$G = \frac{\sum_i^n (2i - n - 1)|X_i|}{|\bar{X}|n(n-1)}, \tag{4.5}$$

where *n* is the total number of pixels and $X_i ... X_n$ are the pixel flux values in ascending order. The Gini coefficient has the benefit that it does not require a well-define centroid of the galaxy.

$M_{20}$ is the second-order moment of the brightest 20 per cent of a the flux of a galaxy. The total second-order moment is given by

$$M_{\rm tot} = \sum_i^n M_i = \sum_i^n I_i[(x_i - x_c)^2 + (y_i - y_c)^2], \tag{4.6}$$

where $I_i$ is the intensity in each pixel, $(x_i, y_i)$ is the position of the pixel, and $(x_c, y_c)$ is the position of the centre of the galaxy. $M_{20}$ is then given by

$$M_{20} = \log\left(\frac{\sum_i^n M_i}{M_{\rm tot}}\right), \tag{4.7}$$

where the summation $\sum_i^n M_i$ is over the pixels in descending order, and stops when 20 per cent of the total flux is reached, i.e. $\sum_i I_i < 0.2 I_{\rm tot}$. $M_{20}$ is a useful morphological tool to use as it is sensitive to the presence of two close-by nuclei, i.e. a merger/interaction.

This combination allows for the distinction between 'normal' SFGs and ULIRGs. However, there is no clear boundary for the delineation of these populations resulting in various values being used in the literature (Lotz et al., 2008b). The $G - M_{20}$ combination is used in our morphological analysis.

## 4.3 Data and sample selection

### 4.3.1 Deep *HST* observations of the UDS

The morphological analysis presented in this chapter focuses on the region of the UDS complemented by deep *Hubble Space Telescope* imaging as part of the CANDELS multi-cycle treasury program (Grogin et al., 2011; Koekemoer et al., 2011). The CANDELS imaging data was obtained using by the WFC3/IR instrument with both the F125W and F160W filters, covering a total area of 210 arcmin$^2$. The pixel scale of the images is 0.06″ and the PSF has a FWHM of 0.12″ and 0.18″, for the respective filters. The 5-$\sigma$ point-source sensitivity of the images are 27.0 and 27.1 (AB magnitudes), respectively.

Morphological studies require high-resolution images, making these observations ideal for this work and space-based observations are the best way to achieve this as ground-based imaging, even with the use of adaptive optics, is affected by seeing effects. Another reason as to why the images are ideal for morphological studies is the depth of these images allows for the morphologies of distant galaxies (up to $z \sim 3$) to be measured. The F125W and F160W filters have observed bandpasses of 1.1–1.4 and 1.4–1.7 $\mu$m, respectively, allowing for rest-frame optical morphologies to be measured from $z \sim 3$ up the current epoch.

### 4.3.2 Sample selection from the faint radio population

The sample used here, for which counterparts from the images above were identified, is the 6-$\sigma$ radio catalogue described in Chapter 2. Using this catalogue, the images described above were visually examined for sources with optical counterparts. Any counterparts towards the edge of the images were excluded to avoid morphological misclassification due to edge effects. 68 sources were identified in the CANDELS images, for which secure morphologies could be obtained; the redshift distribution of this sample is given in Figure 4.2. Figure 4.3 displays $12'' \times 12''$ stamps of some of optical counterparts, overlayed with radio contours.

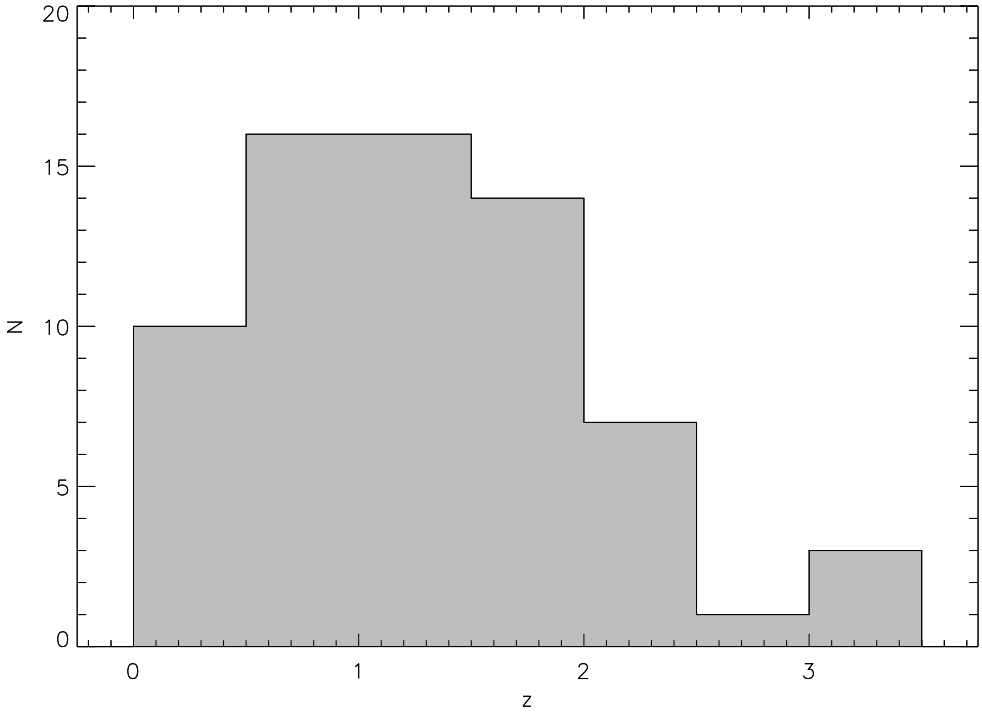


Figure 4.2: Redshift distribution of the sample with optical counterparts in the CANDELS UDS region, for which morphologies were measured.

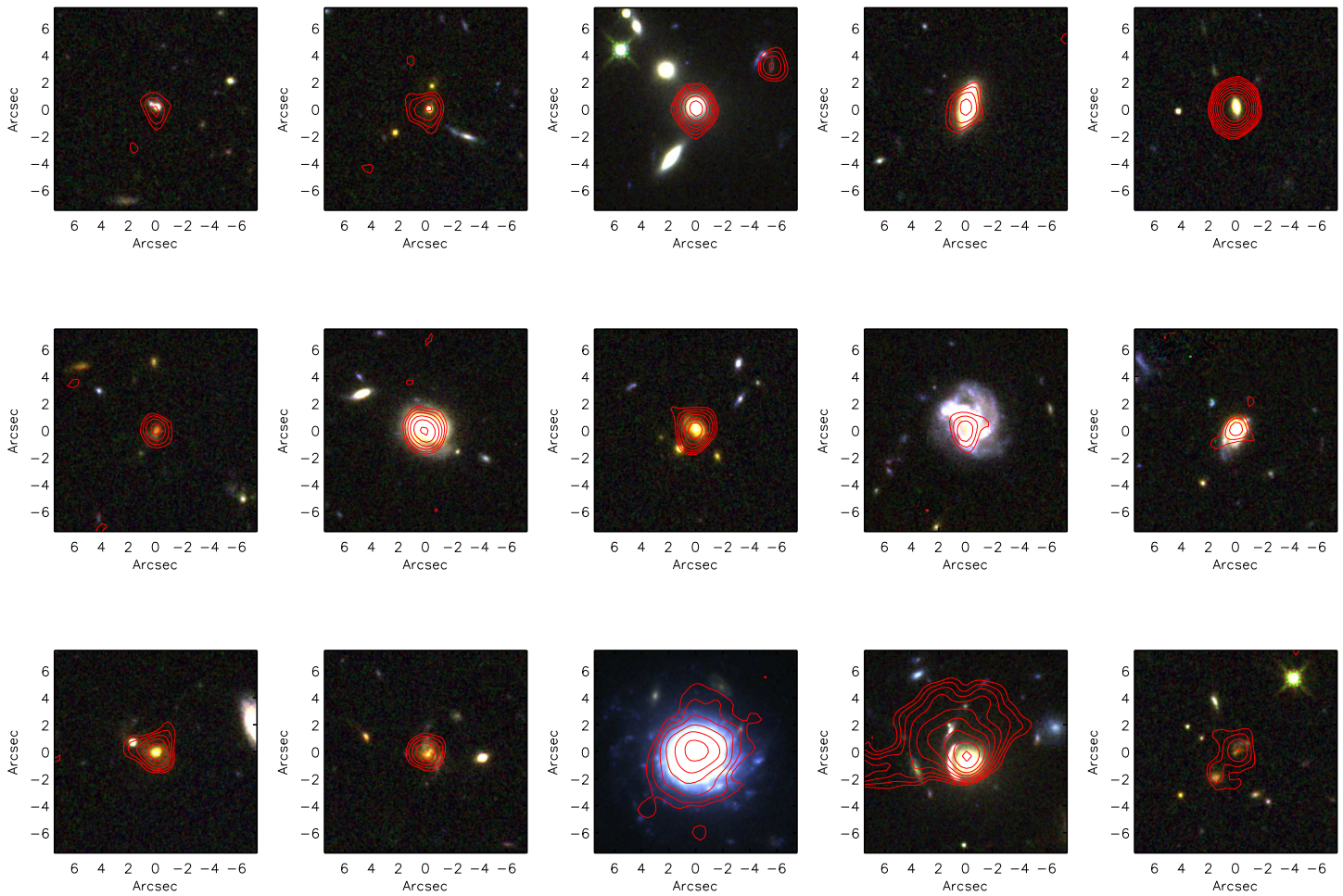


Figure 4.3: $12'' \times 12''$ cut-outs centred on optical counterparts from the CANDELS UDS image. Colour images are constructed using images from *HST* ACS and WFC3 instruments. Radio contours are overlayed in red at $-3\sigma$, $3\sigma$ and increments of $\sqrt{2}$.

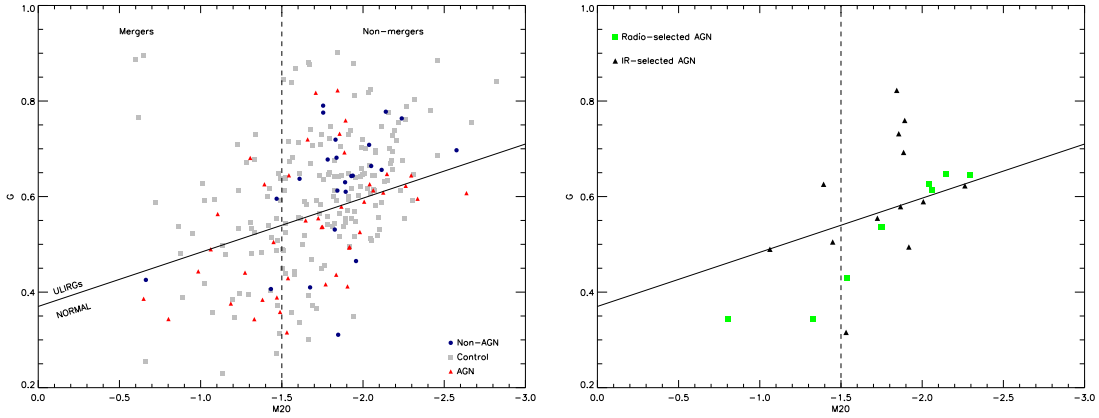


(a) (b)

Figure 4.4: (a) $G - M_{20}$ classification of the faint radio population in comparison to a control sample (grey squares). The dashed line at $M_{20} = -1.5$ divides mergers from non-mergers, as defined by visual classification, and the solid locus separates ULIRGs from 'normal' Hubble-type galaxies. AGN (red triangles) and non-AGN (blue filled circles) are identified using the multi-wavelength classification done in Chapter 3; (b) $G - M_{20}$ classification for IR- and radio-selected AGN (black triangles and green filled squares, respectively).

A control sample, for comparison, was also included in this work. The control sample was extracted from the photometric catalogue described in Cirasuolo et al. (2010), by selecting the three non-radio emitters closest to the position of the radio sources on an $H$-magnitude vs. redshift plot.

A detailed explanation of the measurement and calibration of the *Gini* and $M_{20}$ coefficients used here can be found in Stott et al. (2012). In brief , the morphologies are quantified using the Gini and $M_{20}$ components of the galVSM software (Huertas-Company et al., 2008). The software uses $10''$ cutouts centred on each galaxy, along with a corresponding segmentation map – used to describe pixels associated with the galaxy – to calculate the Gini and $M_{20}$ values.

## 4.4 Morphological analysis

Figure 4.4(a) shows the Gini and $M_{20}$ measurements made for the sample discussed above. The Gini-$M_{20}$ combination can be used as a means of differentiating ULIRGs from normal Hubble-types and mergers from non-mergers (Lotz et al., 2008a). The boundaries used in this work for the regions populated by these populations are

different to those suggested by Lotz et al. as they have been calibrated to match the way in which Gini and $M_{20}$ were measured here.

The locus for separating mergers from non-mergers is chosen based on visual identification, where possible, of mergers (defined as sources with a nearby neighbour or a disturbed morphology). It was found that the delineation between mergers and non-mergers occurs at $M_{20} = -1.5$. This was found to hold across the full redshift range of the sample. Stott et al. (2012) found that this method of delineation may result in some contamination by clumpy, star-forming regions, since it is not possible to visually distinguish between star-forming clumps and merger-driven morphologies. The solid locus in Figure 4.4(a) separates ULIRGs from early- and late-Hubble types; Hubble-type galaxies have been referred to as 'normal' in the figure.

The merger fraction of the overall sample is $25 \pm 6$ per cent, with the control sample having a similar merger fraction, $25 \pm 4$ per cent. Based on the multi-wavelength properties determined in Chapter 3, AGN and SFGs have been identified in Figure 4.4(a). AGN and SFGs display merger fractions of $33 \pm 9$ and $13 \pm 7$ per cent, respectively. The presence of these sources in the 'merger' region suggests that galaxy interactions do have a role in triggering star-formation and AGN activity, though the low fraction of mergers hints that it is not the dominant triggering mechanism for either.

A possible reason that more AGN and SFGs galaxies are not picked out as mergers could be due to the Gini-$M_{20}$ method tracing only a very short morphological timescale ($\sim$0.2–0.6 Gyr) in comparison to other morphological analyses, e.g. the concentration/asymmetry parameters are thought to trace merger timescales of up to $\sim$1.2 Gyr (Lotz et al., 2008b).

The Gini-$M_{20}$ classification was also used to investigate if AGN selection at different wavelengths favour a particular host morphology. Figure 4.4(b) shows the host-galaxy morphologies for near-IR- and radio-selected AGN. A similar investigation was not done with X-ray-selected AGN as the X-ray data was not deep enough to yield a sufficient sample size. Near-IR-selected AGN are classified using the IRAC colour-colour technique and the radio selection was done using a luminosity cut. Recall that both are detailed in Chapter 3. Near-IR-selected AGN tend to show no preference for host morphology. However, the radio-selected AGN lie either close to or in the Hubble-type galaxy region. Considering, the uncertainties in morphological classifications, this could possibly mean that a radio-selected AGN sample is sensitive

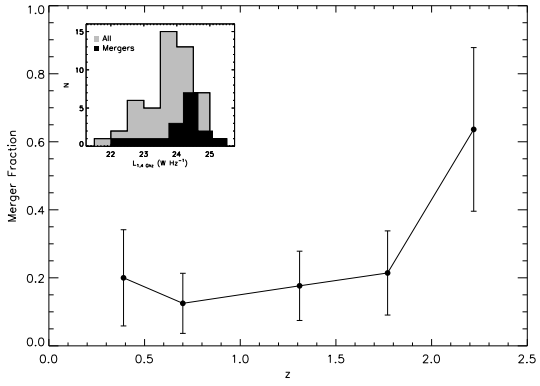


(a)

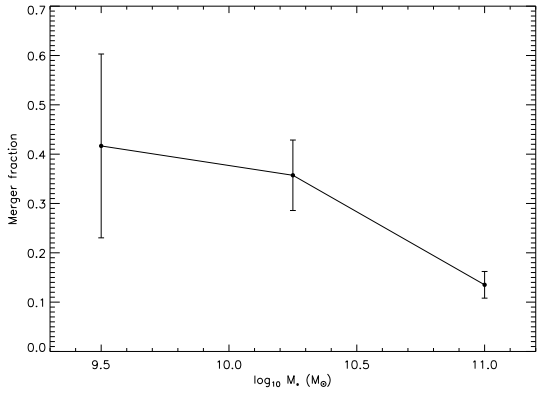


(b)

Figure 4.5: (a) Merger fraction as a function of redshift. *Inset:* Distribution of radio luminosity for the whole sample and for mergers, illustrating that the bulk of mergers are seen at higher luminosities; (b) merger fraction as a function of stellar mass.

to early- and late-type galaxies. The difference in morphological preference suggests that the different emissions are selecting AGN at either varying stages or through varied column densities of gas, or due to contamination of SFGs (Pierce et al., 2007).

The redshift evolution of the merger fraction is displayed in Figure 4.5(a). Up to $z \sim 2$, the merger fraction shows no evolution, then it rises sharply for the final redshift bin. This rise in the merger fraction could be due to observational biases (Malmquist bias), where only the brightest sources are seen; since mergers are seen as the more luminous radio sources (inset, Figure 4.5(a)), they are most likely the dominant observed sources. Hence, excluding the final bin, it can be concluded that there is no evolution in the merger fraction over cosmic time up to $z \sim 2.5$. As most galaxies are expected to have assembled their mass by $z \simeq 2$ (peak of star-formation activity – Hopkins & Beacom, 2006), a peak in merger activity would be expected

around this epoch if galaxy mergers played an important role in driving the cosmic star-formation activity. Recently, using visual classification to identify mergers, Kaviraj et al. (2012) have found a similar result. Figure 4.5(b) is a plot of merger fraction against mass. With a higher merger fraction at a lower mass, low-mass galaxies are more likely to undergo a galaxy merger than their high-mass counterparts.

## 4.5 Conclusions

Here, I presented a morphological analysis of optical counterparts to the sample of faint radio sources discussed in previous chapters, in the area covered by deep CANDELS *HST* imaging. The morphologies of 68 securely identified counterparts were measured using the *Gini*-$M_{20}$ classification scheme, separating mergers from non-mergers. The delineation between these two morphologies, found to be at $M_{20} = -1.5$, was deduced by visually classifying galaxies with either close neighbours or disturbed morphologies as mergers. With less significance to this particular work, a locus to distinguish between ULIRGs and Hubble-type galaxies was also included in the *Gini*-$M_{20}$ classification.

Using near-IR- and radio-selected AGN samples, as previously defined, the morphological classification was used to investigate if the different wavelength selection was sensitive to a particular AGN-host-galaxy morphology. While the near-IR-selected sample seemed not to have a preference to any particular type of host morphology, the radio-selected AGN sample was found to favour Gini and $M_{20}$ values resembling or close to 'normal' Hubble-type host galaxies. A similar investigation of X-ray-selected AGN could not be performed as the available X-ray data was not deep enough to produce a statistically sufficient sample.

The merger fraction for both AGN and non-AGN was found to be low, at $33 \pm 9$ and $13 \pm 7$ per cent, respectively. The low fraction for both types suggest that mergers and interactions do not play an important role in triggering black-hole growth or star-formation activity. The merger fraction of the overall sample was found to show no significant evolution since $z \sim 2$. This again suggests that mergers could not have played an important role in galaxy mass assembly as galaxies are expected to have assembled much of their stellar mass by $z \sim 2$, the epoch at which the peak of cosmic star-formation activity has been observed. Finally, the merger fraction was observed to be higher for low-mass galaxies.

No morphological classification scheme is perfect; most become less useful at high redshift as it is harder to define the edge of a galaxy and to identify sub-structures such as arms and star-forming clumps. Morphological classifications are therefore subject to contamination from neighbouring classes. Improvements will come in time with deeper observations, e.g. with the James Webb Space Telescope, and as more robust automated morphological classifications are developed.

# Chapter 5

# Panchromatic stacking

## 5.1 Introduction

Providing an accurate history of cosmic star formation – how and when the available fuel is turned into stars – is one of the key goals of modern astrophysics. This can be approached in (at least) two ways: we can delineate how the star-formation-rate density changes with cosmic time, or we can track the build-up of stellar mass.

A strong correlation exists between the star-formation rate (SFR) and the stellar mass of a galaxy, and this is true from as early as $z \sim 7$ (González et al., 2010) through to the present epoch. This star-formation 'main sequence' – so-called as it is populated by SFGs, while passive galaxies (those considered to be 'red and dead') and extreme starbursts (e.g. submm-selected galaxies) lie off the relation – maintains a low scatter over cosmic time. This suggests that stellar mass plays an important role in regulating the star-formation activity of a galaxy. The high fraction of SFGs that populate the main sequence suggests that they undergo a continuous star-formation phase over a long timescale – a 'secular' mode of star formation, through a continuous stream of gas to the galaxy, as opposed to the merger-induced gas fuelling that leads to an extreme starburst event (Wuyts et al., 2011; Papovich et al., 2011).

The strong correlation between SFR and stellar mass makes it difficult to compare the star-formation activity between galaxies of different masses. Normalising the SFR by stellar mass allows for a comparison of the physical properties of different galaxies and this quantity is known as the specific star-formation rate (SSFR). The SSFR is a probe of the efficiency at which a galaxy converts a proportion of its mass into stars. The overall SSFR is seen to be fairly constant between $z \sim 7$ and $z \sim 2$ (González

et al., 2010; Stark et al., 2012), followed by a steep decline at lower redshifts. The turnover in the SSFR could indicate a change in the dominant mode of star formation at more recent epochs, or merely the decreasing availability of gas with which to form stars. The SSFR is found to be lower for more massive galaxies compared to their less massive counterparts at all redshifts. This implies that massive galaxies assemble early and that the bulk of star-forming activity at recent epochs occurs in low-mass galaxies. This phenomenon is often referred to as 'cosmic downsizing'.

The SFR – and in turn the SSFR – is an important probe of the history of star formation. Accurate measurements over cosmic time are required to fully understand the cosmic star-formation history. Several obstacles make this job difficult, e.g. their dusty environments make it difficult to assess the star-formation activity in SFGs, and many of these objects are missed by rest-frame ultraviolet or even optical imaging surveys. However, the dust-absorbed starlight is re-emitted in the rest-frame far-IR and hence the integrated IR luminosity, $L_{\rm IR}$, covering rest-frame 8–1000 $\mu$m, is a good tracer of dust-enshrouded star formation activity, providing a reliable dust-enshrouded SFRs (to which must be added the unobscured component, unless this has been factored in to the conversion factor). Constraining the IR portion of a galaxy SED is thus crucial, and this has been known since *COBE* discovered that cosmic IR radiation accounts for approximately half of the total energy output in the Universe (Puget et al., 1996; Lagache et al., 2005).

SED fitting techniques provide a means of deducing the physical properties of galaxies, such as $L_{\rm IR}$, dust properties (temperature and mass). $L_{\rm IR}$ is intimately related to SFR, and $M_{\rm dust}$ is related to the mass of gas, though this is likely to be strongly metallicity-dependent. SED fitting can be done either by comparison of templates defined by dust models representing far-IR/submm observations of local galaxies (e.g. Chary & Elbaz, 2001; Draine & Li, 2007) or by characterising the radiation of a galaxy with that of a modified blackbody (a greybody – Kovács et al. 2010; Magdis et al. 2011). The latter technique is used in this work to deduce dust properties and will be discussed in more detail in later. The IR SED is defined by the Rayleigh-Jeans tail (usually the rest-frame far-IR and submm bands), the position of the SED peak (usually at rest-frame $\sim$ 60–200 $\mu$m) and the Wien tail (in the rest-frame mid-IR).

Observations from space observatories such as *Spitzer* and *AKARI* have been used to probe the Wien portion of galaxy SEDs; the Rayleigh-Jeans portion has been constructed using observations from ground-based instruments such as SCUBA and

AzTEC. However, probing the peak of the SED of galaxies has been a challenge due to the very limited sensitivity of observations in this region of the spectrum. Estimation of the total IR luminosity was typically accomplished via extrapolation of limited coverage in the mid-IR or submm wavebands, introducing large uncertainties. Recent observations by *Herschel* (Pilbratt et al., 2010)) have improved the measurement of SEDs of galaxies at all redshifts, allowing more complete SEDs to be constructed with the peak of the emission accurately sampled.

As well as deducing the star-formation activity via far-IR measurements, the work presented here also utilises my deep radio imaging of the UDS to investigate the star-formation properties of galaxies. As we have seen, radio emission is a very good tracer of star formation because the observed synchrotron radiation is due to the acceleration of relativistic particles in supernovae remnants – the remains of short-lived massive stars (Condon, 1992). Estimating SFRs from radio observations has the advantage that the emission is dust-unbiased. Radio interferometric imaging also benefits from high-angular resolution, greatly reducing the chances of blending; this is a significant source of uncertainty in single-dish far-IR/submm observations due to the large beam sizes. However, an important consideration when using radio observations to investigate star formation is the possibility of contamination by radio-loud AGN. The way in which I handle AGN contamination will be discussed in more detailed later in this chapter.

As we have seen several times already, radio emission from SFGs is tightly correlated with their far-IR emission (e.g. Helou et al., 1985). This correlation exist because young, massive stars are ultimately responsible for both the radio and the far-IR emission. There is still much debate as to whether the far-IR/radio correlation holds up to high redshifts (e.g. Ivison et al., 2010b; Bourne et al., 2011). By stacking in the far-IR and radio bands, we can explore the validity of the far-IR/radio correlation out $z \sim 4$. Using radio observations as an additional probe of star-formation activity allows for a comparison between entirely independent star-formation-rate indicators.

In this chapter I discuss the stacking of panchromatic data to obtain detailed high-SNR SEDs in order to probe the star-formation history of galaxies from $z \sim 4$ to the present epoch. Stacking is also performed in the radio bands to explore the far-IR/radio correlation out to high redshift and to provide an independent star-formation-rate indicator.

## 5.2 Observations

### 5.2.1 Parent sample, photometric redshifts and stellar masses

The catalogue used in this paper was again selected from the UDS, which is the deepest of the five surveys that comprise UKIDSS (Lawrence et al., 2007), exploiting the Wide-Field IR Camera (WFCAM – Casali et al., 2007) on UKIRT. In this chapter I exploit DR8. Stacking, mosaicing and quality control for the UDS was performed using a different recipe to the standard UKIDSS pipeline, and is described fully in Almaini et al. (in preparation). The near-IR images have median seeing of 0.86 and 0.76 arcsec (FWHM) in $J$ and $K$, respectively, with astrometry (calibrated against 2MASS stars) accurate to $\sigma < 0.05$ arcsec. Photometry is uniformly accurate to $<$2 per cent r.m.s. in both bands. Source extraction was accomplished using SExtractor (Bertin & Arnouts, 1996), using simulations to characterise source completeness (details are described in Foucaud et al. 2007). Objects which were saturated, in noisy regions or defined as compact ($K < 19.9$ and with a 50 per cent light radius around the PSF) were not included in the catalogue.

We matched the UDS $K$-selected catalogue to deep optical data in this field from the Subaru *XMM-Newton* Deep Field survey (Furusawa et al., 2008) in five broad-band filters to 3-$\sigma$ depths of $B = 28.4, V = 27.8, R = 27.7, i' = 27.7$ and $z' = 26.6$ (in AB magnitudes; again, 2-arcsec diameter apertures).

This deep multi-wavelength coverage of the UDS allowed us to model the galaxy SEDs in detail, as described in Cirasuolo et al. (in prep). The SED fitting procedure, to derive photometric redshifts, was performed with a code based largely on the public package *Hyperz* (Bolzonella et al., 2000) and exploits reliable photometry in 16 broad bands from far-UV to the mid-IR. Both empirical (Coleman et al., 1980; Kinney et al., 1996; Mignoli et al., 2005) and synthetic templates (Bruzual & Charlot, 2003) were used to model the galaxy SEDs, including a prescription for dust attenuation (Calzetti et al., 2000) and Lyman-series absorption due to the H I clouds in the intergalactic medium, according to Madau (1995). The masses used in this work were derived using SED fitting and will be discussed in Cirasuolo et al. (in preparation).

### 5.2.2 *Herschel* observations

A $30' \times 30'$ region of the UKIDSS UDS was observed at 100 and 160 $\mu$m for a total of 14 hours with the PACS instrument (Poglitsch et al., 2010) aboard *Herschel* during 2011, as part of the *Herschel* Multi-tiered Extragalactic Survey (HerMES) guaranteed time key programme (see HerMES Collaboration et al., 2012, for details). These data were reduced using a refined version of the pipeline described by Ibar et al. (2010b). Briefly, they are projected onto a grid of pixels at 100 and 160 $\mu$m, where the cores of the observed point spread function (PSF) measure 7.4 and 11.3 arcsec FWHM, and the resultant 1-$\sigma$ noise levels are 2.24 and 4.28 mJy, respectively.

The area observed by PACS lies within a $\sim$0.7 deg$^2$ region that has been imaged to well below the confusion limit using SPIRE. Data were obtained simultaneously at 250, 350 and 500 $\mu$m for a total of 10.5 hr, comprising 7 repetitions of two near-orthogonal scans, with the telescope tracking at 30 arcsec s$^{-1}$. These data comprise part of the HerMES guaranteed time key programme (HerMES Collaboration et al., 2012).

Our SPIRE maps have 6-, 8- and 12-arcsec pixels ($\sim$FWHM$/3$) and are produced using the iterative map-maker SHIM, described in Levenson et al. (2010). Briefly, SHIM iteratively removes a low-order polynomial from the detector time-streams for each pass across the field, thus removing detector baseline drifts while preserving large-scale structure in the map.

### 5.2.3 Radio observations

The radio data used here are described in Chapter 2. We also employed the GMRT image described by Ivison et al. (2007), which covers the entire UDS to $\sigma \sim 40\,\mu$Jy beam$^{-1}$ with a spatial resolution of around 6 arcsec.

### 5.2.4 Archival observations in the mid-IR and submm wavebands

Substantial fractions of the UDS have been mapped close to the confusion limit with *Spitzer* using its IRAC and MIPS cameras as part of the SpUDS legacy survey[1]. The region has also been imaged from the ground in the submm and mm wavebands, using the SCUBA and AzTEC cameras mounted on the 15-m James Clerk Maxwell

[1] `irsa.ipac.caltech.edu/data/SPITZER/docs/spitzermission/observingprograms/legacy/`

Telescope, as described by Coppin et al. (2006) and Austermann et al. (2010). Wider images were also obtained using AzTEC on the smaller Atacama Submillimetre Telescope Experiment (ASTE) telescope (Hatsukade et al., in prep).

## 5.3 Stacking $K$-selected galaxies

Stacking methodology – as employed by Dole et al. (2006) and many other studies since – is a very effective tool for exploring the multi-frequency mean or median of a sample of galaxies in the absence of clustering, even when the spatial resolution is poor and/or the source density is high. We cannot always investigate the panchromatic properties of individual galaxies, but by choosing appropriate redshift and mass bins for a sufficiently large sample of galaxies we can determine their general properties and their evolution with mass and/or redshift. Stacking small cut-outs from an image, each centred on the position of a galaxy as determined accurately in some other waveband, makes it possible the determine the typical properties of that galaxy sample, sometimes to levels well below the confusion limits of the image.

In this case, our parent $K$-selected sample – the catalogue that provides accurate positions at which we stack cut-outs from our panchromatic images – was described in §5.2.1. The panchromatic imaging, spanning observed-frame wavelengths from 8 $\mu$m to 50 cm, with excellent sampling in the regions where galaxy spectra are most changeable, were described in §5.2.

## 5.4 Stacking of far-IR observations

As discussed above, the standard stacking method is ideal for the case where clustering is not an issue. If the input catalogue is clustered, however, then care needs to be taken to ensure that an appropriate correction is made, particularly when the spatial resolution is poor and/or the source density is high. This can be done in a number of ways, e.g. following the technique outlined by Bourne et al. (2011). Alternatively, the stacking methodology can be adapted to account for the clustered input catalogue, as outlined by Viero et al. (in prep). In what follows, we use both of these techniques.

### 5.4.1 Simultaneous stacking

Briefly, the Viero et al. method accounts for double-counting of flux density due to clustering of the input catalogue by using the positions of *all* the galaxies in the parent sample *simultaneously*. determining the flux density contribution from each bin to the observed flux density at a given position.

We start with a blank image for each mass bin and each given redshift slice, then add a delta function at the position (to the nearest pixel) of each galaxy, then convolve this image to the resolution of the image to which it is to be matched. At high source densities and/or with strong clustering, some of these galaxies will now be overlapping, even within a single mass bin and redshift slice.

As stacking yields an average flux density, all sources contributing towards a particular stack can be assumed to have flux densities identical to the stacked flux density. Then, for a given sky position, $j$, in the presence of clustered galaxies from different mass bins, the observed flux density, $S_{\rm obs}$, can be described by

$$S^{j}_{\rm obs} = N^{j}_{1} S_1 + N^{j}_{2} S_2 + ... + N^{j}_{\alpha} S_{\alpha}, \tag{5.1}$$

where $\alpha$ refers to the mass and redshift bin, $N^{j}_{\alpha}$ is the number of sources that fall on pixel $j$ and $S_{\alpha}$ is the average flux density of a particular bin. As $N^{j}_{\alpha}$ is known, fitting a function to Equation 5.1 for all pixels with values of unity or more in the map above will give solutions to $S_{\alpha}$, the clustering-corrected stacked flux densities for the respective bins.

### 5.4.2 Traditional stacking

The method presented by Bourne et al. (2011) takes a more traditional approach to stacking, creating small postage stamps for each mass and redshift bin (Fig. 5.2), and correcting for the effects of clustering by calculating the autocorrelation function of galaxies in the parent catalogue for each bin.

To address the issue of clustering, the Landy & Szalay (1993) estimator,

$$W(\theta) = \frac{DD - 2DR - RR}{RR}, \tag{5.2}$$

was used, where $DD$ is the number of target-target source pairs as a function of radius, $\theta$; $DR$ is the number of target-random source position pairs and $RR$ is the number of random-random source position pairs.

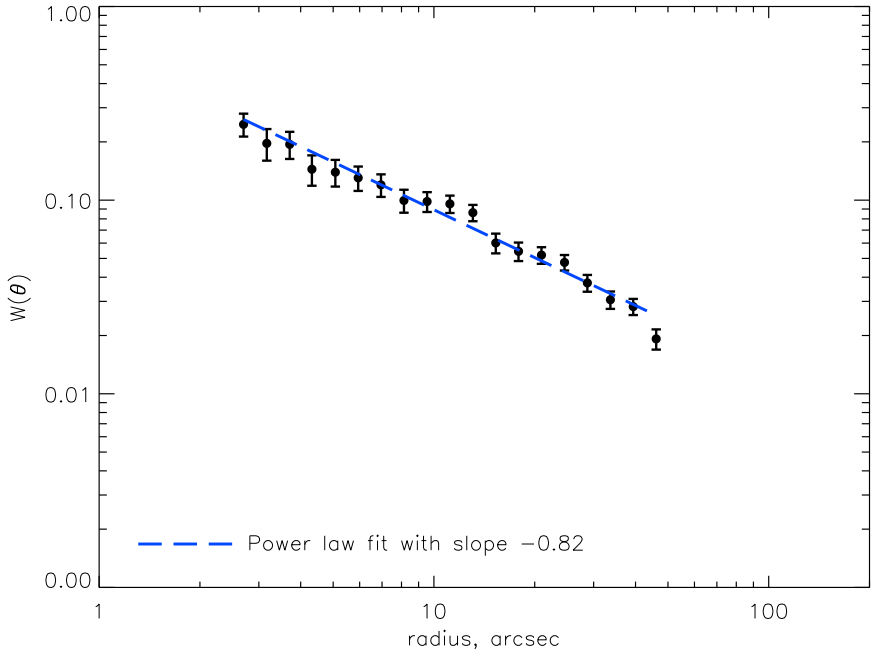


Figure 5.1: Autocorrelation function for the *K*-band parent catalogue used here.

Using positions from our parent *K*-band catalogue, the autocorrelation function $W(\theta)$ is calculated; this provides an estimate of the probability of a source being found at a radius $\theta$ from the target source. The autocorrelation function for our parent catalogue is shown in Fig. 5.1. The autocorrelation function can be fit by the function, $W(\theta) = A\,\theta^{\delta}$, where $\log A = -3.15 \pm 0.08$ and $\delta = -0.82 \pm 0.03$. Uncertainties were obtained by dividing the sample into four quadrants and accessing the scatter in $W(\theta)$ across these regions.

The flux density contribution due to clustering, $F$, is then obtained in the form of a fraction of the average source flux density by convolving $W(\theta)$ with the point spread functions (PSFs) – assumed to be Gaussians – of the observed bands. The correction factor to be applied to the stacked flux densities is then given by $1/(1+F)$. As the level of clustering is expected to vary from bin to bin, we must calculate a correction factor for each bin. To obtain these, the slope was fixed to $\delta = -0.8$ and the cross-correlation of each bin with the full catalogue was calculated.

### 5.4.3 Comparison of the two stacking methods

For both stacking techniques, the units of the images were in Jy beam$^{-1}$; as explained earlier this means that the pixel with the peak flux represents the integrated flux of

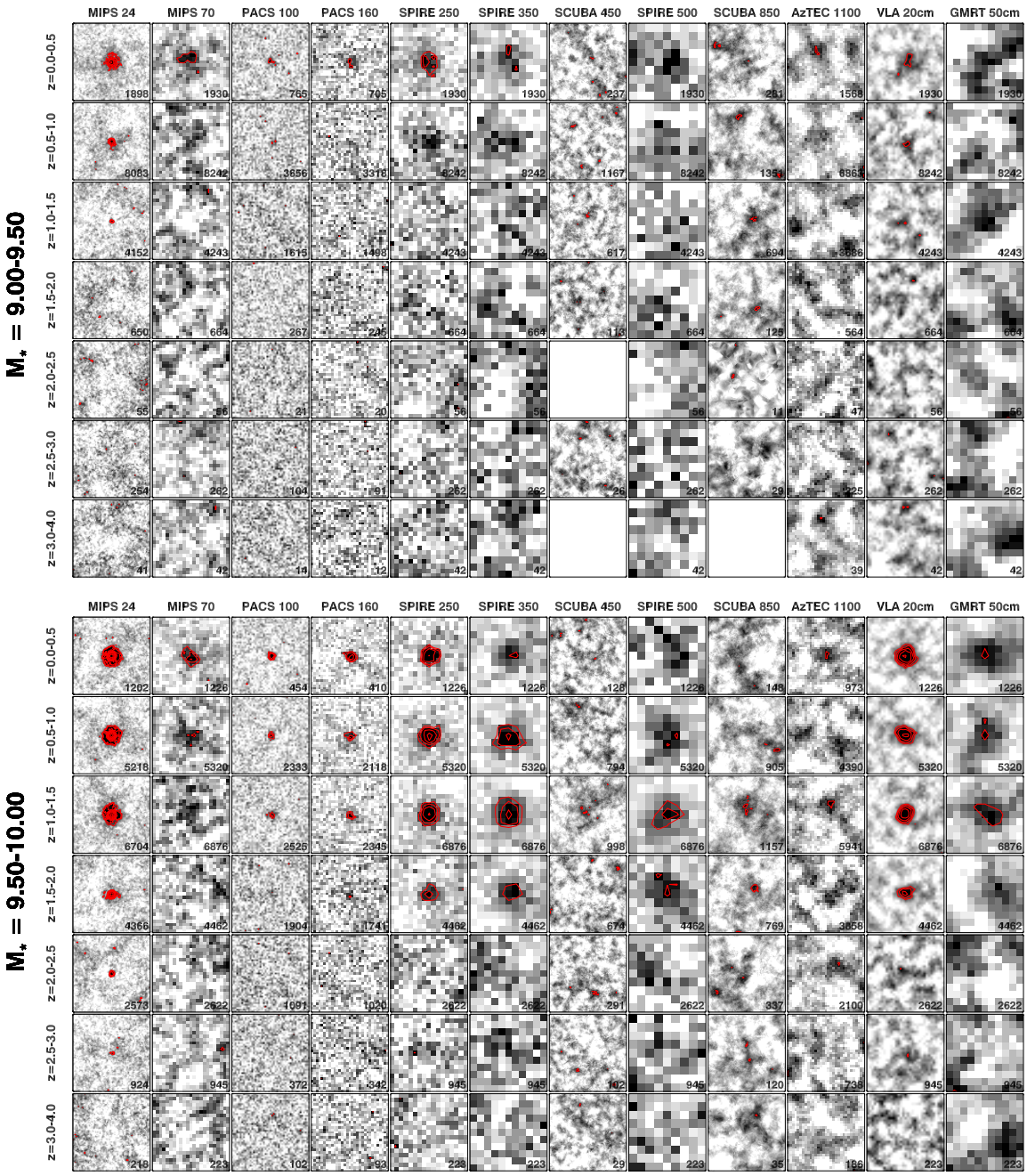


Figure 5.2: $45'' \times 45''$ postage-stamp images of the multi-wavelength stacks. North is up; East is left. The number of sources contributing to each stack is displayed in each image. Contours start at $3\sigma$ and increase in steps of $\sqrt{2}$.

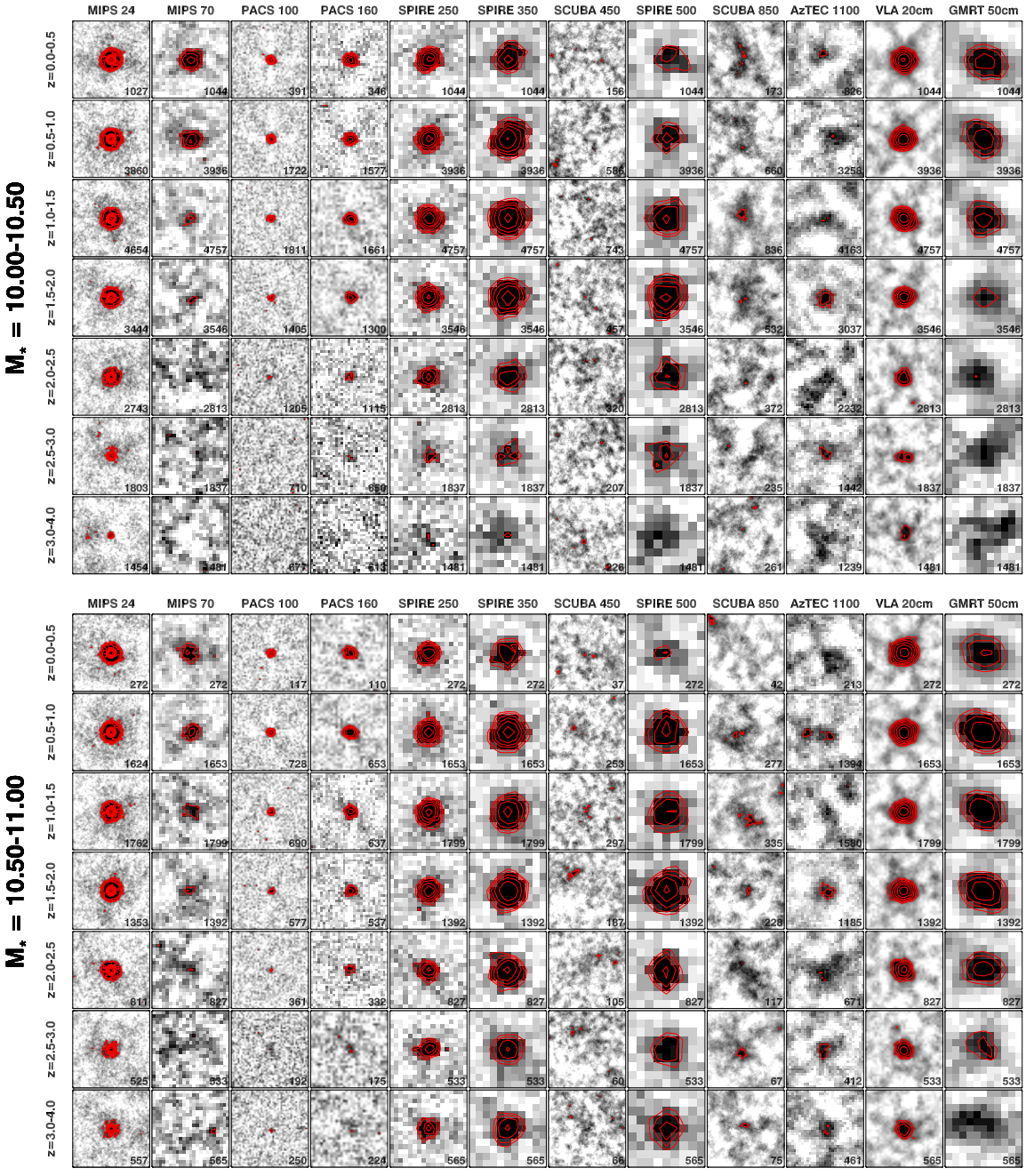


Figure 5.2: Cont...

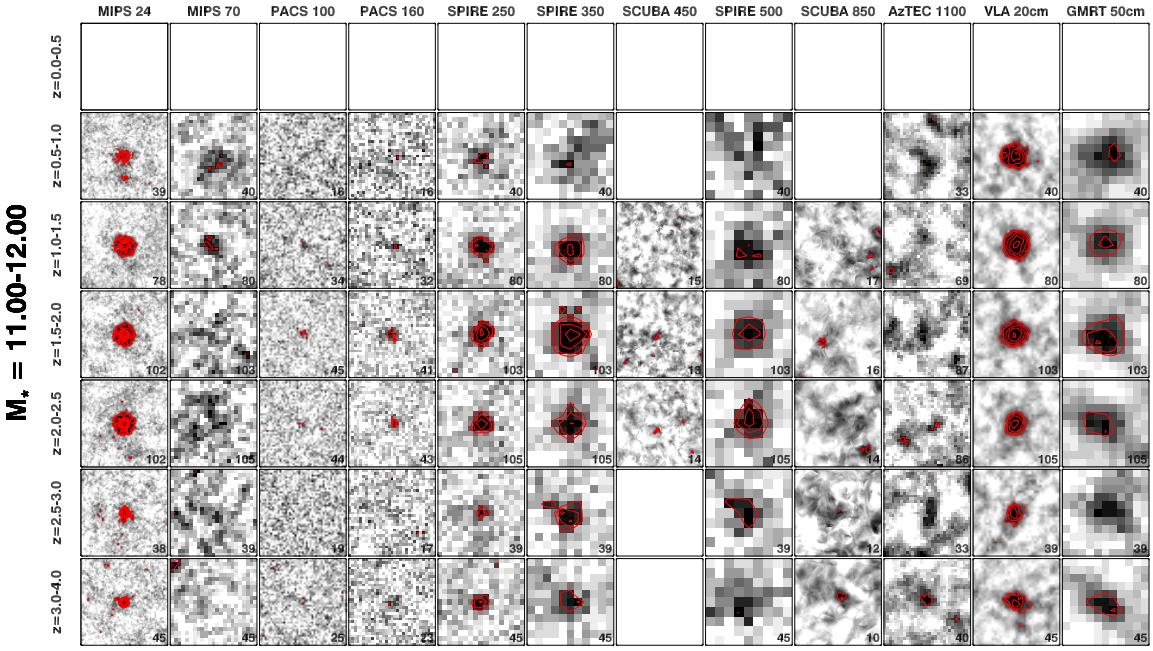


Figure 5.2: Cont...

the stacked source. In the case of simultaneous stacking, pixel values were used as the total flux, whereas Gaussian-fitting was used to extract fluxes form traditionally stacked images.

Figure 5.3 displays the SEDs for all mass and redshift bins for the two different stacking methods; red points represent traditionally stacked fluxes and black points represent fluxes obtained from the simultaneous stacking routine. Overall, fluxes from the two methods agree with one another reasonable well, though there is a good agreement between the two methods at higher masses.

## 5.5 Stacking in the radio waveband

The radio image was stacked at the positions of the *K*-band sources, producing a $91 \times 91$-pixel postage stamp, corresponding to $\sim 31''$ on each side of the stamp. The radio map has units of Jy beam$^{-1}$, which means that in a perfect world the peak value of the stacked point source is the total flux of the stacked sample. The final stacked image could either represent a median or mean image of the selected parent sample. Radio observations are sensitive to emission from AGN activity which can skew the flux distribution and yield biased SFRs. Hence, it is important to take this

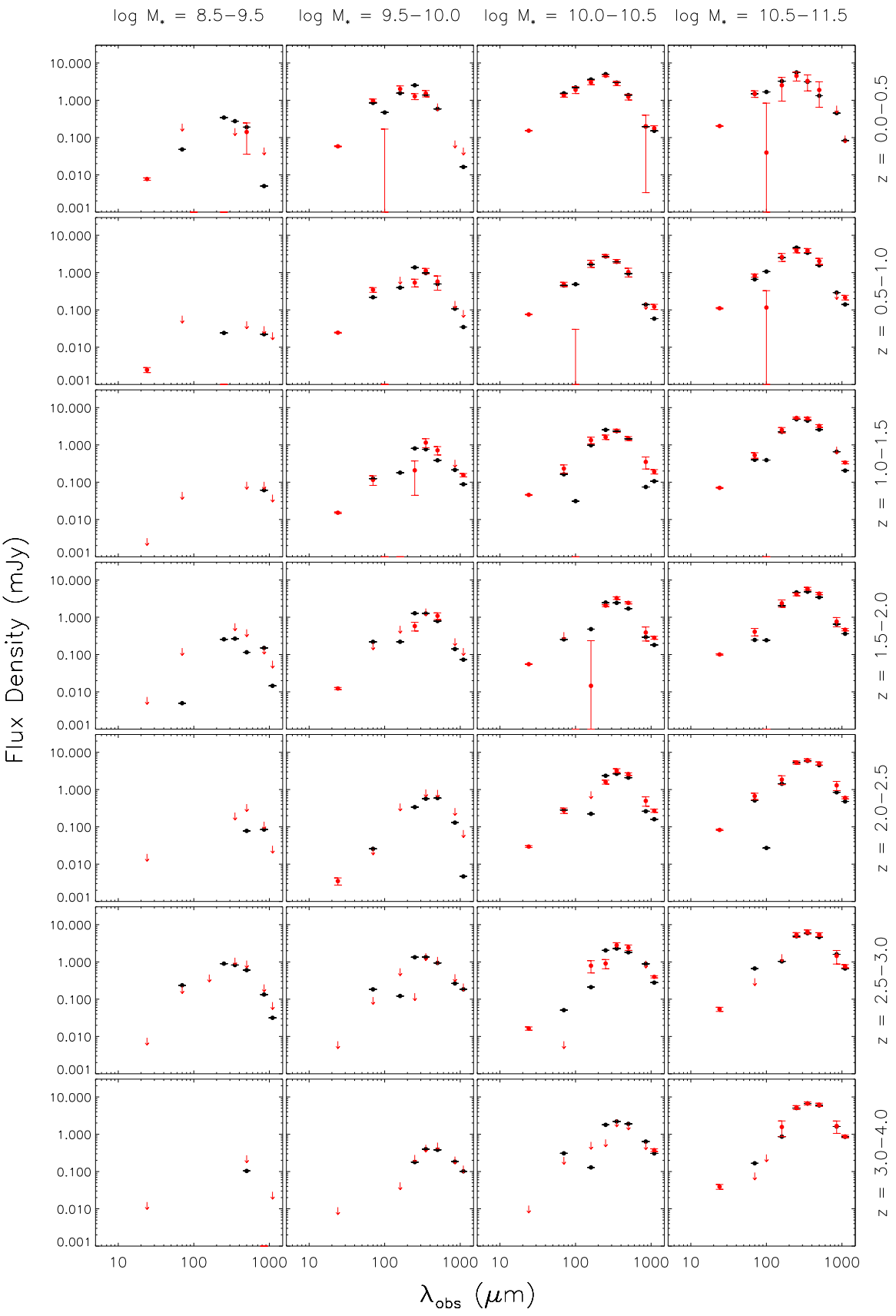


Figure 5.3: A comparison of SEDs constructed using simultaneous (black points) and traditional (red points) stacking.

source of contamination into consideration. As reported by Karim et al. (2011), simply excluding detections or introducing a threshold can artificially alter a sample. In order to overcome this issue, the median stack is used instead. It is robust against outliers while still allowing for the entire sample to be used (Gott et al., 2001).

Another important consideration when stacking radio images, particularly high-resolution images, is bandwidth smearing (BWS – Dunne et al., 2009; Karim et al., 2011), which we have already encountered. The effect of BWS on the source is to attenuate the peak, as the source is smeared radially from the pointing centre. As discussed in Chapter 2, BWS smearing is an important consideration for the radio data presented in this thesis due to the finite bandwidth of the VLA correlator and the small synthesised beam. A correction needs to be applied if peak pixel values are used as the total flux. Due to the mosaiced nature of the radio map, the final BWS effect is combination of contributions from multiple pointings. This could introduce several uncertainties in determining the extent of BWS. However, we can exploit the fact that the total flux density of a source affected by BWS is conserved. As postage stamps were generated in the stacking process, rather than a single pixel centred on the source, fluxes were extracted using all the information available. The $\mathcal{AIPS}$ task, JMFIT, was used to extract fluxes by fitting a Gaussian to the stacked source.

To check for any positional offset, i.e. whether or not the peak of the Gaussian is aligned to the central pixel, a stack of the entire sample (all mass and redshift bins) was generated (see Figure 5.4); no astrometric correction was needed as the peak of the Gaussian was aligned with the central pixel. As the stacking procedure probes the map at very faint levels, the dirty beam is visible in Figure 5.4. This is because the CLEANing process for the radio map was accomplished using only those sources visible to the eye. The ultra-faint sources that comprise the stacked emission are well below the CLEAN threshold employed, so they appear in their 'dirty' guise. Based on correction factors presented in Dunne et al. (2009), any corrections are expected to be very small and do not have a significant effect on the results presented here.

### 5.5.1 Radio-derived star-formation rates

The rest-frame 1.4-GHz luminosity was calculated using

$$L_{1.4\,\mathrm{GHz}}\,(\mathrm{W\,Hz^{-1}}) = 9.52 \times 10^{18}\, S_{1.4\,\mathrm{GHz}}\, D_{\mathrm{L}}^{2}\, 4\pi(1+z)^{-0.2}$$

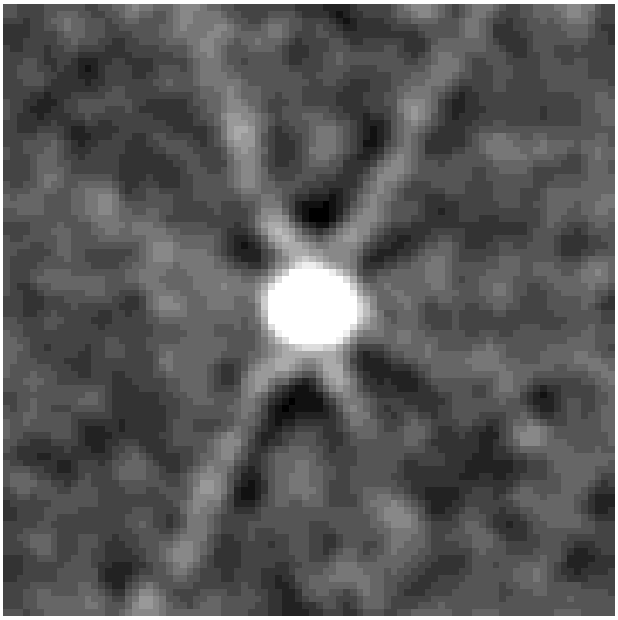

Figure 5.4: $31'' \times 31''$ radio postage stamp, made using all the sources from mass and redshift bins with a strong signal in Fig. 5.2. The dirty beam can be seen clearly, since cleaning of the radio image cannot take place at these faint levels.

where $D_{\rm L}$ is the luminosity distance (Mpc) and $S_{1.4{\rm GHz}}$ is the 1.4-GHz flux density (Jy). This assumes a radio spectral index, $\alpha = -0.8$, where $S_\nu \propto \nu^\alpha$. The luminosity is calculated using the median redshift. While the peak of the radio luminosity might not coincide with the median redshift, it is the best approximation that can be used here since the possibility of stacking a source with extended nature prohibits peak pixel values to be used in order for a median luminosity to be calculated instead.

The calculated luminosities can then be converted into a star-formation rate based on the far-IR/radio correlation, as inferred by Bell (2003), and is given by

$$\begin{aligned} {\rm SFR}\,({\rm M}_\odot\,{\rm yr}^{-1}) &= 5.52\times10^{-22}\,L, \quad L > L_{\rm c} \\ &= \frac{5.52\times10^{-22}\,L}{0.1+0.9(L/L_{\rm c})^{0.3}}, \quad L \leq L_{\rm c} \end{aligned}$$

where $L_{\rm c} = 6.4\times10^{21}\,{\rm W\,Hz^{-1}}$.

The conversion suggested by Bell (2003) assumes a Salpeter initial mass function (IMF), i.e. the IMF is proportional to $M^{-2.35}$, within a mass range of 0.1–100 $M_\odot$. A

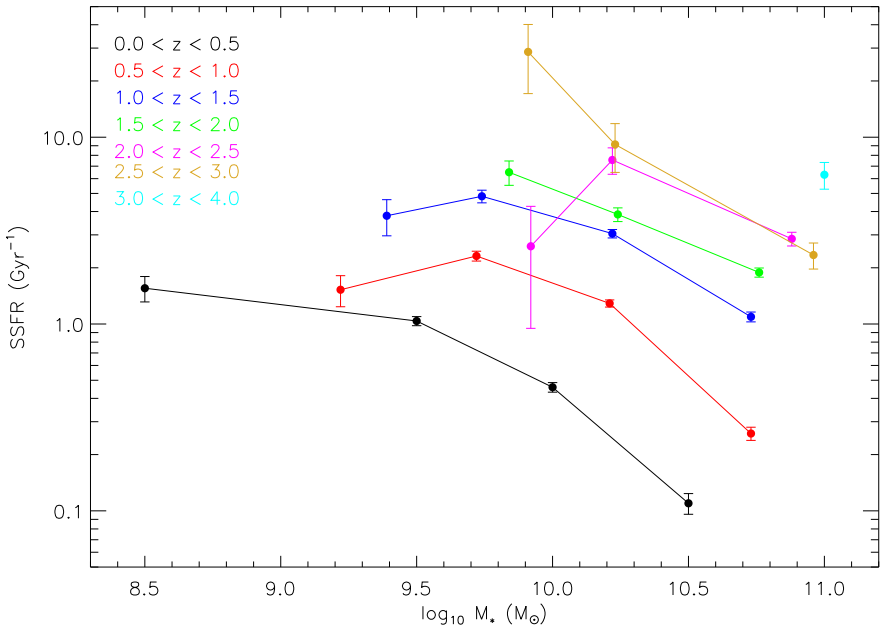


Figure 5.5: Specific star-formation rates as a function of mass for the different redshift bins, derived from 1.4-GHz luminosity.

different conversion is used for low-luminosity sources as Bell suggest that the non-thermal radio emission is suppressed at low luminosities, and hence needs a 'boost'.

## 5.6 Specific star-formation rates

The specific star-formation rates (SSFR = SFR/$M_*$) as a function of mass is displayed in Figure 5.6, for all redshift bins. The SSFR is a useful tool as it describes the fraction of a galaxy's mass that can be converted to stars in a given time. This can be taken as a measure of the galaxies star-formation efficiency. At all redshifts, a decreasing trend as a function of mass is seen, i.e. less massive galaxies are seen to have higher SSFR. However, the dependence of SSFR on stellar mass is not a strong one.

There is a strong increase in SSFR with redshift, seen for all masses. As well as this, the SSFR for a given mass is seen to increase with increasing redshift. These results indicate that galaxies in the early Universe were not only forming stars at a higher rate, but were also forming stars more efficiently. The SSFR–mass relation was not found to be a strong correlation, which agrees with previous work in the literature (e.g. Dunne et al., 2009; Pannella et al., 2009).

A number of previous studies have found that the drop in SSFR with redshift is

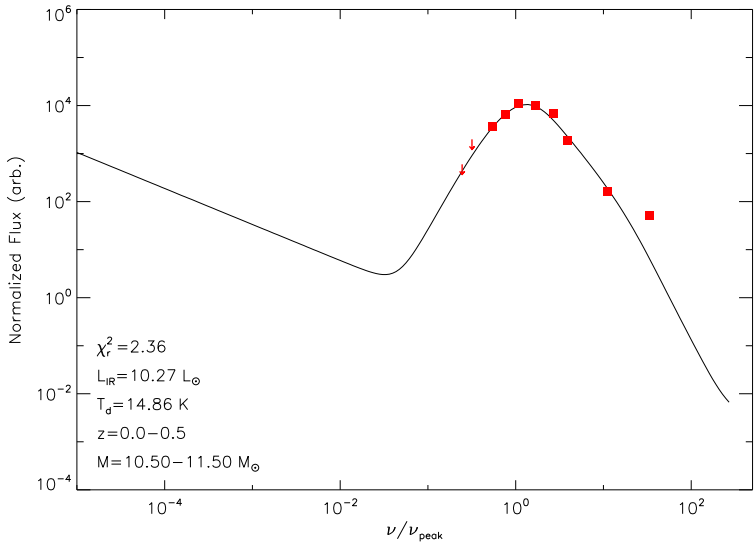


Figure 5.6: Sample SED fit using single temperature model

more rapid at higher masses (Cowie et al., 1996; Pérez-González et al., 2008). This is usually interpreted as 'cosmic downsizing', where the star-formation efficiency is being shifted to lower mass galaxies. This rapid decrease is not observed in the data presented here. This finding is supported by other, recent studies on SSFR (Dunne et al., 2009; Karim et al., 2011)

## 5.7 Future work

The next phase of this work, to be undertaken during the next 9 months at UK ATC, will be to use the two independent stacking methods discussed above to study the history of cosmic star formation as a function of stellar mass. This has proved impossible until very recently, due to the lack of availability of the necessary UDS catalogue, but this problem has now been largely overcome.

$L_{\rm IR}$ will be derived through greybody fits to the panchromatic SEDs assembled here. Obscured SFRs determined via $L_{\rm IR}$ will be compared with those determined from the radio stacking, and added to unobscured SFRs determined using population synthesis model fits to the rest-frame ultraviolet–through–IR SEDs of the parent $K$-selected galaxies (Cirasuolo et al., in preparation).

Figure 5.6 shows a sample fit to the stacked data, using a single temperature model (following Kovács et al. 2010), and some of the properties that can be so derived.

The proposed SED fitting will also allow me to explore the evolution of dust temperatures and masses in the parent (roughly mass-selected) sample, as a function of stellar mass and redshift.

# Chapter 6

# Conclusions

This thesis utilises deep, new, high-resolution radio observations of the UKIDSS Ultra Deep Survey field. These data have yielded a large new sample of faint radio emitters, whose properties I explore. I also use the radio image to determine the star-formation activity in a very large sample of $K$-selected galaxies, as a function of redshift and stellar mass.

Chapter 1 introduces the field of radio astronomy and the objects typically detected at radio wavelengths. The latter half of the chapter discusses the fundamental principles of radio interferometry and aperture synthesis.

Chapter 2 describes new pseudo-continuum observations of the UDS, obtained with the VLA at 1.4 GHz – the centrepiece of the thesis. These observations yielded a deep, high-resolution map – with noise levels below $10\,\mu$Jy beam$^{-1}$ within the central $0.7\,\mathrm{deg}^2$. From this, a robust 6-$\sigma$ catalogue was created, using a novel technique to ensure a high level of catalogue reliability. As $\sim$ 90 per cent of the sources in the catalogue are in the sub-mJy flux density regime, and lie in one of the best panchromatic deep fields on the sky, the new sample is ideal for detailed studies the faint radio population.

In Chapter 3, the 6-$\sigma$ radio catalogue was cross-matched with multi-wavelength data to determine the fraction of AGN and SFGs amongst the sub-mJy radio population. The techniques used here for AGN selecting AGN involved thresholds in radio and X-ray luminosity, IRAC colour-colour diagnostics, the 24 $\mu$m-to-radio luminosity ratio ($q_{24}$) and spectral classification. Classifying a source as an AGN if it is identified by at least one of the selection techniques, 53 per cent of the overall sample was found to comprise AGN. As expected, the radio source counts above 1 mJy are dominated by

AGN. A star-forming population emerges below this flux limit, causing a flattening in the source counts, though AGN continue to dominate down to fluxes of $\sim 0.1$ mJy. SFGs dominate below 0.1mJy, though a significant contribution from radio-quiet AGN is plausible. More robust identification methods are needed to understand the prevalence and influence of radio-quiet AGN at the very faint flux densities that e-MERLIN, JVLA and SKA will reach routinely within the next few decades.

Chapter 4 presents a morphological analysis of optical counterparts to a sub-sample of the new UDS radio catalogue that lie within the CANDELS region, using very deep *HST* imaging. The analysis uses the *Gini*-$M_{20}$ classification and concentrates on tracing the merger activity within the sample. The delineation between mergers and non-mergers was determined to be at $M_{20} = -1.5$ by visually classifying sources with a merger signature. The $G - M_{20}$ classification was applied to the AGN and SFGs in the sample. The merger fraction for both AGN and non-AGN was found to be low, suggesting that merger activity plays a relatively minor role in triggering black hole growth and star-formation activity. Tracing the merger fraction over the redshift range covered by the sample shows no evolution since $z \sim 2$, the epoch at which cosmic star formation has been observed to peak. This, again, suggests that merger activity has not played an important role in the mass assembly of galaxies or super-massive black holes.

Finally, Chapter 5 addresses the star-forming activity of the Universe via panchromatic stacking. New *Herschel* images were stacked, alongside the new UDS radio image, at the positions of a deep *K*-band selected sample. Dust-unbiased specific star-formation rates (SSFRs) were derived from the median radio luminosities. SSFRs were found to decrease with increasing mass at all redshifts, i.e. less massive galaxies have a higher SSFR. Also, for a given mass the SSFR is seen to be higher at earlier epochs: galaxies in the early Universe were forming stars at a higher rate as well as more efficiently. Two independent stacking methods are tested and are being used to delineate the complete history of cosmic star formation.

# Bibliography


Antonucci R., 1993, ARA&A, 31, 473

Appleton P. N. et al., 2004, ApJS, 154, 147

Austermann J. E. et al., 2010, MNRAS, 401, 160

Bardelli S. et al., 2009, Astronomy and Astrophysics, 495, 431

Barger A. J., Cowie L. L., Wang W., 2007, The Astrophysical Journal, 654, 764

Barlow M. J. et al., 2010, A&A, 518, L138

Beers T. C., Flynn K., Gebhardt K., 1990, AJ, 100, 32

Bell E. F., 2003, ApJ, 586, 794

Bershady M. A., Jangren A., Conselice C. J., 2000, The Astronomical Journal, 119, 2645

Bertin E., Arnouts S., 1996, A&AS, 117, 393

Biggs A. D., Ivison R. J., 2006, MNRAS, 371, 963

Biggs A. D., Ivison R. J., 2008, MNRAS, 385, 893

Biggs A. D. et al., 2011, MNRAS, 413, 2314

Blain A. W., Longair M. S., 1993, MNRAS, 264, 509

Bolzonella M., Miralles J.-M., Pelló R., 2000, A&A, 363, 476

Bondi M. et al., 2003, A&A, 403, 857

Bourne N., Dunne L., Ivison R. J., Maddox S. J., Dickinson M., Frayer D. T., 2011, MNRAS, 410, 1155

Boyle B. J., Cornwell T. J., Middelberg E., Norris R. P., Appleton P. N., Smail I., 2007, MNRAS, 376, 1182

Bridge C. R. et al., 2007, The Astrophysical Journal, 659, 931

Bruce V. A. et al., 2012, Monthly Notices of the Royal Astronomical Society, 427, 1666

Brusa M. et al., 2010, ApJ, 716, 348

Bruzual G., Charlot S., 2003, MNRAS, 344, 1000

Burke ., Graham-Smith ., 2002, An Introduction to Radio Astronomy

Calzetti D., Armus L., Bohlin R. C., Kinney A. L., Koornneef J., Storchi-Bergmann T., 2000, ApJ, 533, 682

Caputi K. I., Cirasuolo M., Dunlop J. S., McLure R. J., Farrah D., Almaini O., 2011, MNRAS, 413, 162

Caputi K. I. et al., 2006, ApJ, 637, 727

Carilli C. L., Yun M. S., 1999, ApJ, 513, L13

Casali M. et al., 2007, A&A, 467, 777

Chapman S. C., Blain A. W., Smail I., Ivison R. J., 2005, ApJ, 622, 772

Chary R., Elbaz D., 2001, ApJ, 556, 562

Cirasuolo M., McLure R. J., Dunlop J. S., Almaini O., Foucaud S., Simpson C., 2010, MNRAS, 401, 1166

Coleman G. D., Wu C.-C., Weedman D. W., 1980, ApJS, 43, 393

Condon J. J., 1989, ApJ, 338, 13

Condon J. J., 1991, in Astronomical Society of the Pacific Conference Series, Vol. 18, Duric N., Crane P. C., eds, The Interpretation of Modern Synthesis Observations of Spiral Galaxies, p. 113

Condon J. J., 1992, ARA&A, 30, 575

Condon J. J., 1997, PASP, 109, 166

Condon J. J., 2007, in Astronomical Society of the Pacific Conference Series, Vol. 380, Afonso J., Ferguson H. C., Mobasher B., Norris R., eds, Deepest Astronomical Surveys, p. 189

Condon J. J., Cotton W. D., Greisen E. W., Yin Q. F., Perley R. A., Taylor G. B., Broderick J. J., 1998, AJ, 115, 1693

Conselice C. J., 2003, The Astrophysical Journal Supplement Series, 147, 1

Conselice C. J., Rajgor S., Myers R., 2008, Monthly Notices of the Royal Astronomical Society, 386, 909

Coppin K. et al., 2006, MNRAS, 372, 1621

Cowie L. L., Songaila A., Hu E. M., Cohen J. G., 1996, AJ, 112, 839

Del Moro A. et al., 2013, A&A, 549, A59

Dole H. et al., 2006, Astronomy and Astrophysics, 451, 417

Donley J. L., Rieke G. H., Rigby J. R., Pérez-González P. G., 2005a, ApJ, 634, 169

Donley J. L., Rieke G. H., Rigby J. R., PerezGonzalez P. G., 2005b, The Astrophysical Journal, 634, 169

Downes ., Peacock ., Savage ., Carrie ., 1986, Monthly Notices of the Royal Astronomical Society (ISSN 0035-8711), 218, 31

Draine B. T., Li A., 2007, ApJ, 657, 810

Draper A. R., Northcott S., Ballantyne D. R., 2011, ApJ, 741, L39

Dunlop J. S. et al., 2004, MNRAS, 350, 769

Dunlop J. S., Peacock J. A., 1990, MNRAS, 247, 19

Dunne L., Eales S., Ivison R., Morgan H., Edmunds M., 2003, Nat, 424, 285

Dunne L. et al., 2009, MNRAS, 394, 3

Eales S., Lilly S., Gear W., Dunne L., Bond J. R., Hammer F., Le Fèvre O., Crampton D., 1999, ApJ, 515, 518

Eales S., Lilly S., Webb T., Dunne L., Gear W., Clements D., Yun M., 2000, AJ, 120, 2244

Engel H. et al., 2010, ApJ, 724, 233

Fanaroff B. L., Riley J. M., 1974, MNRAS, 167, 31P

Fixsen D. J., Dwek E., Mather J. C., Bennett C. L., Shafer R. A., 1998, ApJ, 508, 123

Fomalont E. B., Kellermann K. I., Cowie L. L., Capak P., Barger A. J., Partridge R. B., Windhorst R. A., Richards E. A., 2006, ApJS, 167, 103

Foucaud S. et al., 2007, MNRAS, 376, L20

Frayer D. T. et al., 1999, ApJL, 514, L13

Frayer D. T., Ivison R. J., Scoville N. Z., Yun M., Evans A. S., Smail I., Blain A. W., Kneib J.-P., 1998, ApJL, 506, L7

Furusawa H. et al., 2008, ApJS, 176, 1

Ginzburg V. L., Syrovatskii S. I., 1965, Annual Review of Astronomy and Astrophysics, 3, 297

González V., Labbé I., Bouwens R. J., Illingworth G., Franx M., Kriek M., Brammer G. B., 2010, ApJ, 713, 115

Gott J. R., III, Vogeley M. S., Podariu S., Ratra B., 2001, ApJ, 549, 1

Grazian A. et al., 2006, A&A, 449, 951

Greve T. R. et al., 2005, MNRAS, 359, 1165

Grogin N. A. et al., 2011, The Astrophysical Journal Supplement Series, 197, 35

Harrison F. A. et al., 2010, in Society of Photo-Optical Instrumentation Engineers (SPIE) Conference Series, Vol. 7732, Society of Photo-Optical Instrumentation Engineers (SPIE) Conference Series

Helou G., Soifer B. T., Rowan-Robinson M., 1985, ApJ, 298, L7

HerMES Collaboration et al., 2012, ArXiv e-prints

Holland W. S. et al., 1999, MNRAS, 303, 659

Hopkins A. M., Afonso J., Chan B., Cram L. E., Georgakakis A., Mobasher B., 2003, AJ, 125, 465

Hopkins A. M., Beacom J. F., 2006, The Astrophysical Journal, 651, 142

Hubble ., 1936, Realm of the Nebulae

Huertas-Company M., Rouan D., Tasca L., Soucail G., Le Fèvre O., 2008, Astronomy and Astrophysics, 478, 971

Hughes D. H. et al., 1998, Nat, 394, 241

Ibar E. et al., 2008, MNRAS, 386, 953

Ibar E., Ivison R. J., Best P. N., Coppin K., Pope A., Smail I., Dunlop J. S., 2010a, MNRAS, 401, L53

Ibar E., Ivison R. J., Biggs A. D., Lal D. V., Best P. N., Green D. A., 2009, MNRAS, 397, 281

Ibar E. et al., 2010b, MNRAS, 409, 38

Ikarashi S. et al., 2011, MNRAS, 415, 3081

Ivison R. J. et al., 2010a, MNRAS, 402, 245

Ivison R. J. et al., 2007, MNRAS, 380, 199

Ivison R. J. et al., 2002, MNRAS, 337, 1

Ivison R. J. et al., 2010b, A&A, 518, L31

Ivison R. J., Smail I., Le Borgne J.-F., Blain A. W., Kneib J.-P., Bezecourt J., Kerr T. H., Davies J. K., 1998, MNRAS, 298, 583

Ivison R. J., Smail I., Papadopoulos P. P., Wold I., Richard J., Swinbank A. M., Kneib J.-P., Owen F. N., 2010, MNRAS, 404, 198

Jarvis ., 2012, African Skies, 16

Karim A. et al., 2011, ApJ, 730, 61

Kaviraj S. et al., 2012, Monthly Notices of the Royal Astronomical Society: Letters, 429, L40

Kawakatu N., Kino M., Nagai H., 2009, ApJL, 697, L173

Kellermann K. I., Fomalont E. B., Mainieri V., Padovani P., Rosati P., Shaver P., Tozzi P., Miller N., 2008, ApJS, 179, 71

Kellermann K. I., Wall J. V., 1987, in IAU Symposium, Vol. 124, Hewitt A., Burbidge G., Fang L. Z., eds, Observational Cosmology, p. 545

Kinney A. L., Calzetti D., Bohlin R. C., McQuade K., Storchi-Bergmann T., Schmitt H. R., 1996, ApJ, 467, 38

Koekemoer A. M. et al., 2011, The Astrophysical Journal Supplement Series, 197, 36

Kovács A. et al., 2010, ApJ, 717, 29

Lacy M. et al., 2004, ApJS, 154, 166

Lagache G., Puget J.-L., Dole H., 2005, ARA&A, 43, 727

Landy S. D., Szalay A. S., 1993, ApJ, 412, 64

Lawrence A. et al., 2007, MNRAS, 379, 1599

Levenson L. et al., 2010, MNRAS, 409, 83

Longair ., 2010, High Energy Astrophysics by Malcolm S. Longair. Cambridge University Press

Lotz J. M. et al., 2008a, The Astrophysical Journal, 672, 177

Lotz J. M., Jonsson P., Cox T. J., Primack J. R., 2008b, Monthly Notices of the Royal Astronomical Society, 391, 1137

Lotz J. M., Primack J., Madau P., 2004, The Astronomical Journal, 128, 163

Madau P., 1995, ApJ, 441, 18

Magdis G. E. et al., 2011, ApJ, 740, L15

Mendez A. J., Coil A. L., Lotz J., Salim S., Moustakas J., Simard L., 2011, The Astrophysical Journal, 736, 110

Michalowski M. J. et al., 2012, Monthly Notices of the Royal Astronomical Society, 426, 1845

Mignoli M. et al., 2005, A&A, 437, 883

Mobasher B. et al., 2007, ApJS, 172, 117

Morrison G. E., Owen F. N., Dickinson M., Ivison R. J., Ibar E., 2010, ApJS, 188, 178

Mushotzky R., 2004, in Astrophysics and Space Science Library, Vol. 308, Barger A. J., ed, Supermassive Black Holes in the Distant Universe, p. 53

Norris R. P. et al., 2011, PASA, 28, 215

Owen F. N., Keel W. C., Ledlow M. J., Morrison G. E., Windhorst R. A., 2005, AJ, 129, 26

Owen F. N., Morrison G. E., Klimek M. D., Greisen E. W., 2009, AJ, 137, 4846

Padovani P., Mainieri V., Tozzi P., Kellermann K. I., Fomalont E. B., Miller N., Rosati P., Shaver P., 2009, ApJ, 694, 235

Padovani P., Miller N., Kellermann K. I., Mainieri V., Rosati P., Tozzi P., 2011, ApJ, 740, 20

Pannella M. et al., 2009, ApJ, 698, L116

Papovich C., Finkelstein S. L., Ferguson H. C., Lotz J. M., Giavalisco M., 2011, MNRAS, 412, 1123

Pérez-González P. G. et al., 2008, ApJ, 675, 234

Pierce C. M. et al., 2007, The Astrophysical Journal, 660, L19

Pilbratt G. L. et al., 2010, A&A, 518, L1

Poglitsch A. et al., 2010, A&A, 518, L2

Puget J.-L., Abergel A., Bernard J.-P., Boulanger F., Burton W. B., Desert F.-X., Hartmann D., 1996, A&A, 308, L5

Richards E. A., 2000, ApJ, 533, 611

Sersic ., 1968, Cordoba

Simard L. et al., 2002, The Astrophysical Journal Supplement Series, 142, 1

Simpson C. et al., 2006, MNRAS, 372, 741

Simpson C. et al., 2012, MNRAS, 421, 3060

Singal J., Stawarz L., Lawrence A., Petrosian V., 2010, MNRAS, 409, 1172

Smail I., Ivison R. J., Blain A. W., 1997, ApJL, 490, L5

Smail I., Ivison R. J., Blain A. W., Kneib J.-P., 2002, MNRAS, 331, 495

Smail I., Ivison R. J., Owen F. N., Blain A. W., Kneib J.-P., 2000, ApJ, 528, 612

Smolčić V. et al., 2008, ApJS, 177, 14

Spergel D. N. et al., 2007, The Astrophysical Journal Supplement Series, 170, 377

Stark D. P., Schenker M. A., Ellis R. S., Robertson B., McLure R., Dunlop J., 2012, ArXiv e-prints

Stern D. et al., 2005, ApJ, 631, 163

Stott ., Sobral ., Smail ., Bower ., Best ., Geach ., 2012, eprint arXiv:1212.4834

Strazzullo V., Pannella M., Owen F. N., Bender R., Morrison G. E., Wang W.-H., Shupe D. L., 2010, ApJ, 714, 1305

Tacconi L. J. et al., 2008, ApJ, 680, 246

Tacconi L. J. et al., 2006, ApJ, 640, 228

Ueda Y. et al., 2008, ApJS, 179, 124

van der Kruit P. C., 1971, AAP, 15, 110

van der Wel A. et al., 2011, The Astrophysical Journal, 730, 38

Warren S. J. et al., 2007, MNRAS, 375, 213

Willner S. P. et al., 2012, ApJ, 756, 72

Windhorst R., Mathis D., Neuschaefer L., 1990, in Astronomical Society of the Pacific Conference Series, Vol. 10, Kron R. G., ed, Evolution of the Universe of Galaxies, p. 389

Windhorst R. A., Miley G. K., Owen F. N., Kron R. G., Koo D. C., 1985, The Astrophysical Journal, 289, 494

Wuyts S. et al., 2011, ApJ, 742, 96

Younger J. D. et al., 2007, ApJ, 671, 1531

Yun M. S., Reddy N. A., Condon J. J., 2001, ApJ, 554, 803

# Publications

**Refereed:**

1. *The Herschel PEP/HerMES Luminosity Function. I: Probing the Evolution of PACS selected Galaxies to $z \sim 4$*, Gruppioni, C.; Pozzi, F.; Rodighiero, G.; Delvecchio, I.; Berta, S.; Pozzetti, L.; Zamorani, G.; Andreani, P.; Cimatti, A.; Ilbert, O.; Le Floch, E.; Lutz, D.; Magnelli, B.; Marchetti, L.; Monaco, P.; Nordon, R.; Oliver, S.; Popesso, P.; Riguccini, L.; Roseboom, I.; Rosario, D. J.; Sargent, M.; Vaccari, M.; Altieri, B.; Aussel, H.; Bongiovanni, A.; Cepa, J.; Daddi, E.; Dominguez-Sanchez, H.; Elbaz, D.; Forster-Schreiber, N.; Genzel, R.; Iribarrem, A.; Magliocchetti, M.; Maiolino, R.; Poglitsch, A.; Perez Garcia, A.; Sanchez-Portal, M.; Sturm, E.; Tacconi, L.; Valtchanov, I.; Amblard, A.; Arumugam, V.; Bethermin, M.; Bock, J.; Boselli, A.; Buat, V.; Burgarella, D.; Castro-Rodriguez, N.; Cava, A.; Chanial, P.; Clements, D. L.; Conley, A.; Cooray, A.; Dowell, C. D.; Dwek, E.; Eales, S.; Franceschini, A.; Glenn, J.; Griffin, M.; Halpern, M.; Hatziminaoglou, E.; Ibar, E.; Isaak, K.; Ivison, R. J.; Lagache, G.; Levenson, L.; Lu, N.; Madden, S.; Maffei, B.; Mainetti, G.; Nguyen, H. T.; Halloran, B. O; Page, M. J.; Panuzzo, P.; Papageorgiou, A.; Pearson, C. P.; Perez-Fournon, I.; Pohlen, M.; Rigopoulou, D.; Rowan-Robinson, M.; Schulz, B.; Scott, D.; Seymour, N.; Shupe, D. L.; Smith, A. J.; Stevens, J. A.; Symeonidis, M.; Trichas, M.; Tugwell, K. E.; Vigroux, L.; Wang, L.; Wright, G.; Xu, C. K.; Zemcov, M.; Bardelli, S.; Carollo, M.; Contini, T.; Le Fevre, O.; Lilly, S.; Mainieri, V.; Renzini, A.; Scodeggio, M.; Zucca, E., 2013, MNRAS, in press (arXiv:1302.5209).

2. *The Herschel census of infrared SEDs through cosmic time*, Symeonidis, Myrto; Vaccari, M.; Berta, S.; Page, M. J.; Lutz, D.; Arumugam, V.; Aussel, H.; Bock, J.; Boselli, A.; Buat, V.; Capak, P. L.; Clements, D. L.; Conley, A.; Conversi, L.; Cooray, A.; Dowell, C. D.; Farrah, D.; Franceschini, A.; Giovannoli, E.; Glenn, J.; Griffin, M.; Hatziminaoglou, E.; Hwang, H.-S.; Ibar, E.; Ilbert, O.; Ivison, R. J.; Le Floc'h, E.; Lilly, S.; Kartaltepe, J. S.; Magnelli, B.; Magdis, G.; Marchetti, L.; Nguyen, H. T.; Nordon, R.; O'Halloran, B.; Oliver, S. J.; Omont, A.; Papageorgiou, A.; Patel, H.; Pearson, C. P.; Perez-Fournon, I.; Pohlen, M.; Popesso, P.; Pozzi, F.; Rigopoulou, D.; Riguccini, L.; Rosario, D.; Roseboom, I. G.; Rowan-Robinson, M.; Salvato, M.; Schulz, B.; Scott, Douglas; Seymour, N.; Shupe, D. L.; Smith, A. J.; Valtchanov, I.; Wang, L.; Xu, C. K.; Zemcov, M.; Wuyts, S., 2013, MNRAS, in press (arXiv:1302.4895).

3. *HerMES: Candidate Gravitationally Lensed Galaxies and Lensing Statistics at Submillimeter Wavelengths*, J. L. Wardlow, A. Cooray, F. De Bernardis, A. Amblard, **V. Arumugam** et al., 2013, ApJ, 762:59.

4. *AzTEC half square degree survey of the SHADES fields - II. Identifications, redshifts and evidence for large-scale structure*. M. J. Michalowski, J. S. Dunlop, R. J. Ivison, M. Cirasuolo, K. I.Caputi, I. Aretxaga, **V. Arumugam**, J. E. Austermann, E. L. Chapin, S. C. Chapman, K. E. K. Coppin, E. Egami, D. H. Hughes, E. Ibar, A. M. J. Mortier, A. M. Schael, K. S. Scott, I. Smail, T. A.Targett, J. Wagg, G. W. Wilson, L. Xu, and M. Yun, 2012, MNRAS, 426:1845–1866.

5. *The SCUBA-2 Cosmology Legacy Survey: blank-field number counts of 450 μm-selected galaxies and their contribution to the cosmic infrared background*, J. E. Geach, E. L. Chapin, K. E. K. Coppin, J. S. Dunlop, M. Halpern, Ian Smail, P. van der Werf, S. Serjeant, D. Farrah, I. Roseboom, T. Targett, **V. Arumugam** et al., 2012, MNRAS, in press (arXiv:1211.6668).

6. *Gas-rich mergers and feedback are ubiquitous amongst starbursting radio galaxies, as revealed by the VLA, IRAM PdBI and Herschel*. R. J. Ivison, I. Smail, A. Amblard, **V. Arumugam**, C. De Breuck, B. H. C. Emonts, I. Feain, T. R. Greve, M. Haas, E. Ibar, M. J. Jarvis, A. Kovacs, M. D. Lehnert, N. P. H. Nesvadba, H. J. A. Rottgering, N. Seymour, and D. Wylezalek, 2012, MNRAS, 425:1320–1331.

7. *The Herschel Multi-tiered Extragalactic Survey: HerMES*. S. J. Oliver, J. Bock, B. Altieri, A. Amblard, **V. Arumugam** et al., 2012, MNRAS, 424:1614–1635.

8. *HerMES: deep number counts at 250 μm, 350 μm and 500 μm in the COSMOS and GOODS-N fields and the build-up of the cosmic infrared background*. M. Béthermin, E. Le Floch, O. Ilbert, A. Conley, G. La-gache, A. Amblard, **V. Arumugam** et al., 2012, A&A, 542:A58.

9. *The suppression of star formation by powerful active galactic nuclei*. M. J. Page, M. Symeonidis, J. D. Vieira, B. Altieri, A. Amblard, **V. Arumugam** et al., 2012, Nature, 485:213-216.

10. *The Herschel Multi-tiered Extragalactic Survey: SPIRE-mm photometric redshifts*. I. G. Roseboom, R. J. Ivison, T. R. Greve, A. Amblard, **V. Arumugam** et al., 2012, MNRAS, 419:2758-2773.

11. *Detection of an ultrabright submillimetre galaxy in the Subaru/XMM-Newton Deep Field using AzTEC/ASTE*. S. Ikarashi, K. Kohno, J. E. Aguirre, I. Aretxaga, **V. Arumugam**, J. E. Austermann, J. J. Bock, C. M. Bradford, M. Cirasuolo, L. Earle, H. Ezawa, H. Furusawa, J. Furusawa, J. Glenn, B. Hatsukade, D. H. Hughes, D. Iono, R. J. Ivison, S. Johnson, J. Kamenetzky, R. Kawabe, R. Lupu, P. Maloney, H. Matsuhara, P. D. Mauskopf, K. Motohara, E. J. Murphy, K. Nakajima, K. Nakanishi, B. J. Naylor, H. T. Nguyen, T. A. Perera, K. S. Scott, K. Shimasaku, T. Takagi, T. Takata, Y. Tamura, K. Tanaka, T. Tsukagoshi, D. J. Wilner, G. W. Wilson, M. S. Yun, and J. Zmuidzinas, 2011, MNRAS, 415:3081-3096.

12. *HerMES: SPIRE emission from radio-selected active galactic nuclei*. N. Seymour, M. Symeonidis, M. J. Page, A. Amblard, **V. Arumugam** et al., 2011, MNRAS, 413:1777-1786.

13. *Submillimetre galaxies reside in dark matter haloes with masses greater than 3x10*$^{11}$ $M_{\odot}$. A. Amblard, A. Cooray, P. Serra, B. Altieri, **V. Arumugam** et al., 2011 Nature, 470:510–512.

14. *HerMES: Herschel-SPIRE observations of Lyman break galaxies*. D. Rigopoulou, G. Magdis, R. J. Ivison, A. Amblard, **V. Arumugam** et al., 2010, MNRAS, 409:L7-L12.

15. *Measures of star formation rates from infrared (Herschel) and UV (GALEX) emissions of galaxies in the HerMES fields*. V. Buat, E. Giovannoli, D. Burgarella, B. Altieri, A. Amblard, **V. Arumugam** et al., 2010, MNRAS, 409:L1-L6.

16. *HerMES: deep galaxy number counts from a P(D) fluctuation analysis of SPIRE Science Demonstration Phase observations*. J. Glenn, A. Conley, M. Bethermin, B. Altieri, A. Amblard, **V. Arumugam** et al., 2010, MNRAS, 409:109-121.

17. *Evolution of dust temperature of galaxies through cosmic time as seen by Herschel*. H. S. Hwang, D. Elbaz, G. Magdis, E. Daddi, M. Symeonidis, B. Altieri, A. Amblard, P. Andreani, **V. Arumugam** et al., 2010, MNRAS, 409:75-82.

18. *The Deep SPIRE HerMES Survey: spectral energy distributions and their astrophysical indications at high redshift*. D. Brisbin, M. Harwit, B. Altieri, A. Amblard, **V. Arumugam** et al., 2010, MNRAS, 409:66-74.

19. *The Herschel Multi-Tiered Extragalactic Survey: source extraction and cross-identifications in confusion-dominated SPIRE images*. I. G. Roseboom, S. J. Oliver, M. Kunz, B. Altieri, A. Amblard, **V. Arumugam** et al., 2010, MNRAS, 409:48-65.

20. *Herschel reveals a $T_{dust}$-unbiased selection of z$\sim$2 ultraluminous infrared galaxies*. G. E. Magdis, D. Elbaz, H. S. Hwang, A. Amblard, **V. Arumugam** et al., 2010, MNRAS, 409:22-28.

21. *Cold dust and young starbursts: spectral energy distributions of Herschel SPIRE sources from the HerMES survey*. M. Rowan-Robinson, I. G. Roseboom, M. Vaccari, A. Amblard, **V. Arumugam** et al., 2010, MNRAS, 409:2-11.

22. *HerMES: Far infrared properties of known AGN in the HerMES fields*. E. Hatziminaoglou, A. Omont, J. A. Stevens, A. Amblard, **V. Arumugam** et al., 2010, A&A, 518:L33.

23. *HerMES: The submillimeter spectral energy distributions of Herschel/SPIRE-detected galaxies*. B. Schulz, C. P. Pearson, D. L. Clements, B. Altieri, A. Amblard, **V. Arumugam** et al., 2010, A&A, 518:L32.

24. *The far-infrared/radio correlation as probed by Herschel*. R. J. Ivison, B. Magnelli, E. Ibar, P. Andreani, D. Elbaz, B. Altieri, A. Amblard, **V. Arumugam** et al., 2010, A&A, 518:L31.

25. *Herschel unveils a puzzling uniformity of distant dusty galaxies*. D. Elbaz, H. S. Hwang, B. Magnelli, E. Daddi, H. Aussel,B. Altieri, A. Amblard, P. Andreani, **V. Arumugam** et al., 2010, A&A, 518:L29.

26. *First results from HerMES on the evolution of the submillimetre luminosity function*. S. A. Eales, G. Raymond, I. G. Roseboom, B. Altieri, A. Amblard, **V. Arumugam** et al., 2010, A&A, 518:L23.

27. *HerMES: Halo occupation number and bias properties of dusty galaxies from angular clustering measurements*. A. Cooray, A. Amblard, L.Wang, **V. Arumugam** et al., 2010, A&A, 518:L22.

28. *HerMES: SPIRE galaxy number counts at 250, 350, and 500 $\mu$m*. S. J. Oliver, L.Wang, A. J. Smith, B. Altieri, A. Amblard, **V. Arumugam** et al., 2010,A&A, 518:L21.

29. *The HerMES SPIRE submillimeter local luminosity function*. M. Vaccari, L. Marchetti, A. Franceschini, B. Altieri, A. Amblard, **V. Arumugam** et al., 2010, A&A, 518:L20.

30. *HerMES: The SPIRE confusion limit*. H. T. Nguyen, B. Schulz, L. Levenson, A. Amblard, **V. Arumugam** et al., 2010, A&A, 518:L5.

**Submitted:**

1. *HerMES: Cosmic Infrared Background Anisotropies and the Clustering of Dusty Star-Forming Galaxies*. M. P. Viero, L. Wang, M. Zemcov, G. Addison, A. Amblard, **V. Arumugam** et al., 2013, ApJ, submitted (arXiv: 1208.5049)

2. *The prevelance of AGN feedback in massive galaxies at $z\approx1$*. C. Simpson, P. Wostoby, **V. Arumugam**, R. Ivison, W. Hartley, O. Almaini, 2013, MNRAS, submitted.

**In preparation:**

1. *UDS20: deep, high-resolution radio imaging of the UKIDSS Ultra-Deep Survey field*, **V. Arumugam**, R. J. Ivison, Edo Ibar, C. S. Simpson, M. Cirasuolo, 2013, MNRAS, in preparation

2. *HerMES: Probing the star-formation history of mass-selected galaxies through panchromatic stacking*, **V. Arumugam** + *Her*MES consortium, 2013, MNRAS, in preparation

3. *H-ATLAS: SCUBA2 observations of the reddest Herschel galaxies*, **V. Arumugam** + *H*-ATLAS consortium, 2013, MNRAS, in preparation